2010

Non-axisymmetric instabilities in self-gravitating tori around black holes, and solving Einstein constraints with superconvergent finite element methods

Oleg Korobkin
Louisiana State University and Agricultural and Mechanical College

NON-AXISYMMETRIC INSTABILITIES IN SELF-GRAVITATING TORI AROUND BLACK HOLES, AND SOLVING EINSTEIN CONSTRAINTS WITH SUPERCONVERGENT FINITE ELEMENT METHODS

A Dissertation

Submitted to the Graduate Faculty of the
Louisiana State University and
Agricultural and Mechanical College
in partial fulfillment of the
requirements for the degree of
Doctor of Philosophy

in

The Department of Physics and Astronomy

by

Oleg Korobkin
B.S., Moscow Institute of Physics and Technology, 1998
M.S., Moscow Institute of Physics and Technology, 2003
December 2010

To my family

Acknowledgements

This thesis would have never been written without support of my dear wife Mitsuko, my friends, my family and my teachers.

I want to devote my special thanks to my advisor Erik Schnetter, who gave me so much freedom and provided me with numerous exciting research opportunities. I am thankful to him for always finding time to respond to the most difficult problems that I encountered and giving me great practical advices. I would also like to stress the tremendous help from Ernazar Abdikamalov, for being my friend and, in view of that, for critically examining my thesis. Numerous insightful discussions with Ernazar helped me to refine my ideas and to significantly improve my scientific style. Without his help this thesis would have been embarassingly obscure.

I am very grateful to Burkhard Zink for introducing me to the numerical general relativistic hydrodynamics. I appreciate stimulating conversations which I had with Burkhard over the few years that he was a Distinguished Postdoc at the CCT in LSU. I am also thankful to my first advisor Manuel Tiglio who introduced me in the field of numerical relativity and provided support for my travels to various exciting conferences and collaborations.

I want to thank my teachers at LSU, Lai-Him Chan, Juhan Frank, Gabriela González, Luis Lehner, Jorge Pullin and Joel Tohline for their hard work and for the deep physical and philosophical insights that they gave me. I need to mention the two-week intensive program in gravitational wave astronomy at the University of Texas at Brownsville, which made an indelible impression and determined the direction of my research during the Summer break in 2005. I want to thank organizers of this program, in particular Martha Casquette. I am also grateful to my collaborators Michael Holst and Nikolaos Stergioulas, without whom this work would have been impossible. I would like to thank Bruce Allen, Michael Holst, Luciano Rezzolla and Saul Teukolsky for their hospitality during my visits.

My thesis would have never happened if not for the absolutely unique friendly and creative environment that I enjoyed at LSU thanks to my friends Steven Brandt, Eloisa Bentivegna, Peter Diener, Nils Dorband, Tyler Landis, Frank Löffler, and Enrique Pazos.

This research was supported in part by NSF grants PHY 0505761, 0721915 (Alpaca), 0904015 (CIGR), and 0905046/0941653 (PetaCactus) to Louisiana State University and the Teragrid allocation TG-MCA02N014. The simulations were performed using the supercomputing resources Ranger and Lonestar at TACC via the NSF TeraGrid, and Queenbee at LONI. We also made an extensive use of the PetaShare infrastructure to store the large volumes of data from our simulations.

Table of Contents

Abstract

This thesis contains results on two related projects.

In the first project, we explore non-axisymmetric instabilities in general relativistic accretion disks around black holes. Such disks are created as transient structures in several astrophysical scenarios, including mergers of compact objects and core collapse of massive stars. These disks are suggested for the role of cenral engines of gamma-ray bursts. We address the stability of these objects against the runaway and non-axisymmetric instabilities in the three-dimensional hydrodynamical fully general relativistic treatment. We explore three slender and moderately slender disk models with varying disk-to-black hole mass ratio.

None of the models that we consider develop the runaway instability during the time span of the simulations, despite large radial axisymmetric oscillations, induced in the disks by the initial data construction procedure. All models develop unstable non-axisymmetric modes on a dynamical timescale. In simulations with dynamical general relativistic treatment, we observe two distinct types of instabilities: the Papaloizou-Pringle instability and the so-called Intermediate instability. The development of the nonaxisymmetric mode with azimuthal number $m = 1$ is enhanced by the outspiraling motion of the black hole. The overall picture of the unstable modes in our disk models is similar to the Newtonian case.

In the second project, we experiment with solving the Einstein constraint equations using finite elements on semistructured triangulations of multiblock grids. We illustrate our approach with a simple example of Brill wave initial data, with the constraints reducing to a single linear elliptic equation for the conformal factor ψ. We use quadratic Lagrange elements on semistructured simplicial meshes, obtained by triangulation of multi-block grids. In the case of uniform refinement the scheme is superconvergent at most mesh vertices, due to local symmetry of the finite element basis with respect to local spatial inversions. We show that in the superconver-

gent case subsequent unstructured mesh refinements do not improve the quality of our initial data. As proof of concept that this approach is feasible for generating multi-block initial data in three dimensions, we evolve the constructed initial data using a high order finite-differencing multi-block approach and extract gravitational waves from the numerical solution.

Introduction

Almost a hundred years have passed since the General theory of Relativity (GR) was discovered by Albert Einstein [1, 2]. Throughout this time, no experimental evidence has been found that would have contradicted the predictions of this theory. New experiments and observations remain in a perfect agreement with the conclusions, derived from the basic principles of General Relativity, despite the increasing accuracy of measurements that has become available with advancement of new technologies. These basic principles represent the most remarkable insights into the geometric nature of space, time and gravity. Their discovery opened the door to cosmology as a field of science and allowed to pose as well as answer questions which had previously belonged solely to the realm of philosophy.

One of the predictions of GR is the existence of gravitational waves. So far, only indirect experimental evidence of this natural phenomenon has been found. According to GR, an orbit of a binary should shrink over time because of the loss of energy to gravitational radiation. This effect can be measurable only when the binary consists of two compact objects that are sufficiently close to each other. One example of such system is the famous pulsar PSR B1913+16 in a binary system, discovered by Hulse and Taylor in 1974 [3]. The orbit of this binary is shrinking in precise agreement (up to the accuracy of measurements) with the predictions of GR. This outstanding discovery was one of the motivations to initiate efforts for a direct experimental detection of gravitational waves. As of today, several gravitational wave detectors have been constructed and achieved design sensitivities around the world: LIGO [4], VIRGO [5], GEO-600 [6], TAMA [7]. Despite all the effort, no detection has yet been made, partly because the expected distortion of the metric is incredibly small (relative change in length for a "strong" gravitational wave is $\delta l/l \sim 10^{-20}$), and partly due to the low event rate of the kind of events which produce detectable signals. Such events include mergers of two compact objects, i.e. black

holes or neutron stars, supernova explosions, rotating non-axisymmetric neutron stars and some others [8].

The next two generations of gravitational wave detectors are planned to have increased sensitivity, allowing for a much higher detection probability. These include the detectors under construction (Advanced LIGO [9], Advanced VIRGO [10]) and those in the design phase (LISA [11], Einstein Telescope [12,13]). Chances are high that the next decade will witness the long-awaited direct observation of gravitational waves, opening a new window on the Universe and putting our existing theories and models to the test.

Arguably one of the most important and influential concepts of GR is that of a black hole (BH). In recent decades astronomers have accumulated convincing observational evidence that BHs exist [14–17]. Curiously enough, these objects were originally brought forward as an argument against GR, because they harbor a singularity – a point where most of the currently established physical laws must break down. Although further investigation of the properties of BHs revealed that the singularity is "hidden" from external observers by the event horizon and could never be seen from or affect the outside world, the problem posed by the BH singularity requires a deeper and more general theory, which includes GR as a special case. This is one of the main reasons why we are interested in BHs.

Another reason is that BHs create extreme physical conditions impossible to achieve in a laboratory. The power for some of the most luminous and dramatic cosmic phenomena, such as quasars and active galactic nuclei, is generated by accretion onto a BH. The same mechanism is also believed to power gamma-ray bursts (GRBs) in some models.

GRBs are intense flashes of γ-rays, produced at cosmological distances with an estimated power $\sim 10^{51}$ erg/s ($\sim 10^{18}$ solar luminosities, which is equivalent to $\sim 0.01\ \mathcal{M}_{\odot}$ being annihilated per second) [18–20]. They can be roughly divided into two classes: short gamma-ray bursts (SGRBs) last $\lesssim 2$ s and have a harder spectrum, while long ones (LGRBs) last longer than 2 s and have a softer spectrum. LGRBs constitute the majority of all currently observed GRBs.

Several alternative scenarios exist to explain GRBs. In the standard scenario, short GRBs are believed to be produced by binary neutron stars (NS) or a NS-BH merger events [21], while long GRBs are associated with core collapse supernovae (CCSNe) events [22]. In both cases, the role

of the central engine which powers the burst is played by a solar mass BH surrounded by a thick massive accretion disk (note: alternative scenarios exist, such as the magnetar model [23])

The work reported in this thesis explores the stability of self-gravitating disks around BHs in a fully dynamical GR treatment. For the models of GRBs mentioned above to be plausible, a sufficiently massive disk needs to be present in order to supply matter for a quasi-stationary accretion process lasting for a time span of a few seconds [18]. However, previous studies of thick disks in Newtonian and Cowling approximation have shown that such disks develop non-axisymmetric instabilities of several different types [24–31], and sometimes such instabilities lead to disk fragmentation [32]. When GR effects are taken into consideration, massive self-gravitating disks around BHs could additionally develop the so-called runaway instability [33–43], in which case the disk could be completely consumed by the BH on the timescale of milliseconds. Models of the GRB central engine which rely on the existence of thick massive disk around BH must account for such instabilities, because they could interrupt the accretion powering the burst or make it too irregular.

There are several motivations to study disk instabilities using full GR treatment. First of all, the conclusions about the development of runaway instability in previous works vary depending on which approximation was used. Second, it is not clear if and how the inclusion of GR will modify the growth rates and types of non-axisymmetric unstable modes. Finally, disk oscillations and non-axisymmetric motions could produce potentially detectable gravitational waves. That is why in this work we evolve the spacetime metric along with the disk fluid in a coupled manner, using the complete system of Einstein equations.

In the second part of the thesis we report the results of our work on a somewhat unrelated project, in which we experimented with solving Einstein constraint equations on semistructured multiblock triangulations using finite element (FE) methods. Semistructured triangulations of the finite differencing (FD) grids provide a direct approach to transform the solution between the FD and FE representations, which is exact and does not require interpolation. Additionally, such triangulations provide superconvergent solutions at the points collocated with FD grid. We demonstrate that the FE solution to an elliptic equation, generated for the given FD grid, is sufficiently accurate and convergent for 3D relativistic simulations with independent FD hyperbolic

solver (QUILT).

The thesis is organized as follows. The first Chapter 1 describes the formulations and numerical methods used in both parts of the thesis, including multiblock grids (Section 1.1), high-order finite differencing operators (Section 1.2), and the formulations used to evolve the hydrodynamic (Section 1.3) and general relativistic (Section 1.4) equations. Chapter 2 presents validation tests of the coupling between the GR and hydrodynamic subsystems of the evolution code. Chapter 3 introduces the subject of self-gravitating disks and their instabilities. Chapter 4 describes the grid setup, initial data construction procedure and the data analysis for the non-axisymmetric instabilities. In particular, Section 4.3 describes the curvilinear grid, adapted to the disk evolution problem and designed to maximize the efficiency and save computational costs. Chapters 5 and 6 present the results of the time evolution of self-gravitating disks and the analysis of non-axisymmetric instabilities.

Chapter 7 opens the second part of the thesis by describing motivations for using finite element methods on semistructured triangulations of FD multiblock grids. Chapter 8 gives an overview and a weak formulation example for the Finite Element Toolkit (FETK) [44], which is used for solving the Einstein constraint equations using finite elements. Chapter 9 discusses our approach to multi-block triangulations and, in particular, why we expect our solutions to be superconvergent. In Chapter 10 we evaluate the accuracy of our approach by solving for several three-dimensional elliptic test problems on multi-block domains with known exact solutions. Finally, in Chapter 11 we solve the Brill wave equation, which is a particular case of the Einstein constraints, and in Chapter 12 we use the FD multi-block evolution solver to evolve the Einstein equations and accurately extract a pulse of gravitational waves from the numerical solution. The last Chapter 12 lists two separate conclusions for the two project reported in this thesis.

Throughout the thesis, we use a geometrized system of units where $G = c = 1$. Unless noted otherwise, the BH in our models has mass 2.5 $\mathcal{M}_{\odot}$. In tensor notations below, Latin indices from the beginning of the alphabet (a,b,...) run from 0 to 3, Latin indices i, j, etc. run from 1 to 3, and the usual Einstein summation rule is assumed.

Chapter 1. Formulations and Numerical Methods

The numerical time-evolution scheme used in our study can be split into two main parts: the Einstein evolution equations, and the fluid dynamics equations. These two parts are evolved in a coupled manner. The numerical code that we use has been developed within the CACTUS computational infrastructure [45], and uses the CARPET mesh refinement and multi-mesh driver [46, 47]. A separate module based on CARPET provides a range of multiblock systems to represent a variety of computational domains for 3D evolution codes [48]. The module for evolving the GR hydrodynamics equations uses the THOR multiblock code [49], which has been coupled to the multiblock-based module QUILT for evolving spacetime [50]. The latter implements the Generalized Harmonic formulation of the Einstein equations in first-order form [51]. In the following sections, we give a brief description of the methods implemented in each module.

1.1 Multiblock Approach

For our three-dimensional simulations we use finite differences (FD) discretization with multiple blocks infrastructure developed by [48]. It is a common approach in differential geometry to define a manifold via a set of overlapping blocks, with each block mapped into an open, simply-connected subset of Euclidean space (see, for example, [52]). The blocks are connected by coordinate transformations in the areas where they intersect or overlap. This approach allows to describe manifolds with arbitrary topology. Finite differences discretization introduces a discrete multidimensional grid into every block, which can be thought of as a discrete coordinate chart, mapped into a region of $\mathbb{Z}^3$. It is then required to communicate data between the FD grids of any two neighboring blocks in order to supply boundary conditions on the interpatch boundaries. In the *multi-block* approach the blocks abut rather than overlap, and the

grids are constructed in such a way that neighboring grids share boundary points. In this case, the boundary conditions can be imposed either directly or by adding penalty terms (so-called penalty boundary conditions). If two neighboring blocks do not share common points, then interpolation can be used; this approach is commonly referred to as *overlapping-grids* [53].

The multiblock approach is widely used in astrophysical and numerical relativity simulations (see [53–72] and references therein). In many cases the domain of interest is asymptotically flat. If it contains one or more black holes, then each hole can be excised from the computational domain by introducing an inner smooth boundary around the singularity. If appropriately chosen, this boundary does not require any physical boundary conditions, since all characteristic modes leave the domain. It is preferable that this boundary is smooth, which in general requires the use of multiple blocks; this approach is called the BH excision with multiple blocks [63,73,74]. Similarly, the preferred shape for the outer boundary when simulating asymptotically flat spacetimes is a sphere, as this is the topology of null infinity $\mathcal{J}^+$, which is best suited for extracting gravitational waves. A multipatch domain structure easily accommodates both types of boundaries while avoiding coordinate singularities, such as those associated with spherical or cylindrical coordinates. The use of multiple blocks can also be helpful in cosmological simulations with highly complex non-trivial topologies.

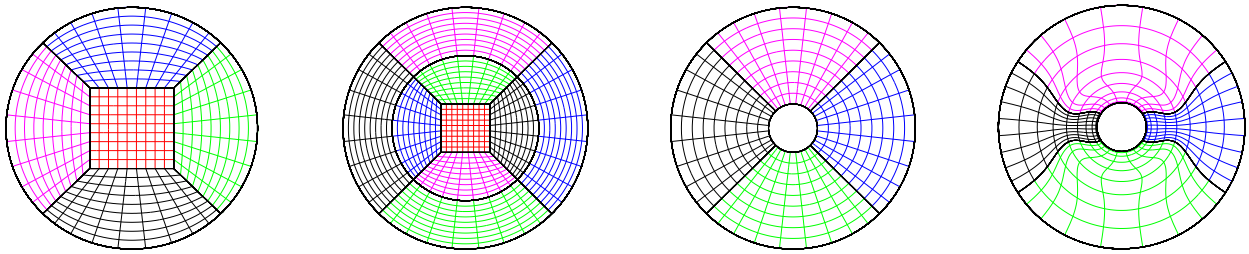

(a) (b) (c) (d)

Figure 1.1: Cross-sections of the block systems used in this work in the xz-plane: (a) seven-block system; (b) thirteen-block system; (c) six-block system with straight coordinate lines; (d) six-block system with distorted radial coordinate lines, described in Section 4.3 below.

Figure 1.1 shows meridional cuts of the patchsystems (cuts in the xz-plane), that are used in this thesis. The first two block systems on Fig. 1.1 are the seven-block and the thirteen-block systems, which realize different representations of a spherical domain. They both have spherical

outer boundary and no coordinate singularities. The seven-block system is also known as the "cubed sphere" [75]. The thirteen-block system additionally has spherical grid coordinate surfaces in the outer layer of blocks, which is very convenient for computing spherical harmonics and extracting gravitational waves. The thirteen-block system is well adapted for simulating radiation processes: the central cubical block has high resolution and can be used to accurately model the dynamics of a source, the intermediate layer can represent a near zone, while the outer layer of blocks models the radiation zone, which carries the outgoing radiation away from the source while maintaining the constant angular and radial resolution. These two systems are used in the Chapter 2 below for evolutions of rotating and non-rotating polytropic stars.

The remaining two block systems on Fig. 1.1 are the six-block system and the adapted six-block system for simulating accretion disks around black holes (described in details below in Section 4.3). Both block systems contain empty spherical region in the middle, which is suitable for simulating BHs with the so-called excision approach. We use the BH excision in our simulations.

It is also necessary to mention that the additional advantage of multiple blocks is their efficiency from the point of required computational resources. For example, if we want to simulate a radiating system, then the number of points in outer blocks of the systems such as displayed on Fig. 1.1 grows linearly with radius of the domain, while both the angular resolution and the radial resolution stay the same. This allows to simulate very large domains at relatively low cost compared to Cartesian rectangular grids, where the number of points is proportional to the cube of the domain size. This is a very important advantage of the numerical method, because modern 3D codes can take several months to complete, and any improvements in terms of their speed or memory resources need to be appreciated. Finally, large domain size makes it possible to causally disconnect the system dynamics from the outer boundary, which is often the main source of numerical noise in a simulation.

1.2 High-order SBP Operators

In our multi-block evolutions, we use new efficient high-order finite differencing (FD) operators satisfying the summation-by-parts (SBP) property developed by [76]. If D is a one-dimensional

differential operator, the SBP property means that for any grid functions u and v on a segment $[a, b]$ with a constant grid spacing h, the following condition is satisfied

$$\langle Du, v\rangle + \langle u, Dv\rangle = u(b)v(b) - u(a)v(a),$$

where $\langle \cdot, \cdot \rangle$ denotes the scalar product between two grid functions, defined by the SBP matrix $\Sigma = ||\sigma_{ij}||$ associated with D:

$$\langle u, v\rangle = \sum_{i,j} \sigma_{ij} u_i v_j$$

In our code we can select from a range of high-order FD operators: D_{2-1}, D_{4-2}, D_{4-3}, D_{6-3}, D_{6-5} and D_{8-4}. The pair of numbers in the FD operator's subindex reflects the convergence order at interior points and at points at and close to the boundary. In more detail: for a generic FD operator D_{a-b}, the convergence order in the interior is a and at and close to the boundaries it is $b \leq a$. The convergence of the numerical derivative in the l_2 norm is at least of order $b + 1$ [77] and in the l_∞ norm – it is at least of order b.

The operators D_{2-1}, D_{4-2}, D_{6-3} and D_{8-4} are diagonal norm (scalar product) based, as they satisfy SBP with respect to certain diagonal scalar product (norm) of grid functions. D_{4-3} and D_{6-5} are so-called "full restricted norm" operators. They satisfy SBP with respect to norms which are not necessarily diagonal, but only restricted to be diagonal at the boundary points. The diagonal norm FD operators have several advantages compared to full restricted norm ones in terms of stability properties. However, they exhibit lower order of convergence at and close to boundary points. While the full restricted norm operators are only one order less convergent at the boundary, diagonal norm operators lose half the convergence order compared to the interior points.

1.3 Hydrodynamics Equations

The evolution equations of a relativistic ideal fluid are derived from the covariant equations of conservation of mass $\nabla_a(\rho u^a) = 0$ and the energy-momentum $\nabla_b T^{ab} = 0$, with the latter

assumed to have the following form [49,78]:

$$T^{ab} = (\rho + u + P)u^a u^b + P g^{ab},$$

where P is the fluid pressure, ρ is the rest mass density, u is the internal energy density [1], and g^{ab} is the spacetime metric in contravariant form. The quantities $\{\rho, u, u^i\}$ then form a set of *primitive variables* that uniquely define the state of the relativistic fluid at every point in space.

The evolution equations read:

$$\partial_t(\sqrt{-g}\rho u^t) + \partial_i(\sqrt{-g}\rho u^i) = 0,$$
$$\partial_t(\sqrt{-g}T^t{}_a) + \partial_i(\sqrt{-g}T^i{}_a) = \sqrt{-g}T^c{}_d\Gamma^d{}_{ac},$$

where t is the time coordinate, $g \equiv \det(g_{ab})$ is the determinant of the spacetime metric and $\Gamma^d{}_{ac}$ are the Christoffel symbols associated with this metric. After introducing a set of *conservative variables* $\{D \equiv \sqrt{-g}\rho u^t, Q_a \equiv \sqrt{-g}T^t_a\}$ the equations can be cast into a flux-conservative form (as in [81]; see details specific to our scheme in [49]):

$$\partial_t D + \partial_i D^i = 0,$$
$$\partial_t Q_a + \partial_i Q^i_a = S_a,$$

where D^i, Q^i_a are the fluxes of the conserved variables D, Q_a, while the S_a are the source terms for Q_a. These equations are then solved using a finite volume cell-centered scheme in the local block basis. The reconstruction of the primitive variables on the cell interfaces is done using the piecewise-parabolic monotonous (PPM) [82] method, while the fluxes through the interfaces are calculated using a Harten-Lax-van Leer (HLL) [83] Riemann solver. In order to compute fluxes, source terms and the stress-energy tensor T^{ab}, the conservative variables need to be converted into primitive ones at every timestep. This is done using a Newton-Rhapson iterative $2D_W$ solver [84] with the Γ-law equation of state. If at a particular cell on the grid the procedure of primitive variables recovery fails to produce physically meaningful values (which can happen

[1] It is also common to define a specific internal energy $\varepsilon = u/\rho$ [79,80]

for number of reasons; see [84]), we use a $1D_P$ solver with a polytropic equation of state.

The boundary conditions for the hydrodynamic variables are imposed on the interpatch boundaries using interpolation from neighboring blocks. The overlap regions where interpolation is done are created by adding extra layers of grid points on each block face. For the outer boundary, outflow boundary conditions are imposed. Further details on the grid setup and numerical methods can be found in [49].

1.4 Spacetime Evolution Equations

For the evolution of the spacetime metric g_{ab} we use the generalized harmonic (GH) formulation of the Einstein equations in the first-order representation developed by Lindblom et al. [51] In this formulation, the coordinate gauges are fixed using a set of four gauge source functions H_a, which need to be prescribed a priori. In our simulations, we have chosen the so-called "stationary gauge" [51,85], in which the gauge source functions stay frozen at their initial values, $H_a(t, x^i) = H_a(t_0, x^i)$. Such a choice of the gauge is convenient for quasi-stationary spacetimes, such as a perturbed BH [50] or an accretion disk around BH.

The first-order representation that we use has advantages of being linearly degenerate, symmetric hyperbolic [86–88] and possessing the constraint damping property. Linear degeneracy guarantees that the system will not develop gauge shocks during the evolution [89]. Symmetric hyperbolicity with boundary conditions imposed on incoming characteristic fields is the necessary condition for well-posedness of the initial boundary value problems (see e.g. Chapter 6 of Gustafsson et al. [90]).

The constraint damping property, which is one of the most important advantages of the chosen formulation, means that the constraints on the variables are included into the evolution equations in such a way that they are automatically damped out in the process of evolution. Such a property not only reduces the error in the solution, but also eliminates variety of numerical instabilities associated with unbounded growth of the constraints.

The spacetime metric evolution equations are discretized using finite differences on multiple grid blocks that cover the computational domain [48, 49]. Advantages of using multiple blocks were outlined in the Section 1.1 above. The grids on any two neighboring blocks in the system

are designed so as to share a 2D interface grid, where the so-called penalty boundary conditions are imposed [91]. For the spatial numerical differentiation, we employ high-order convergent finite differencing operators, that satisfy summation by parts (SBP) property [76], as described in the Section 1.2 above. The SBP property together with penalty boundary conditions guarantee strict linear numerical stability [91]. All simulations of self-gravitating disks with dynamical treatment of relativistic gravity are performed with the finite differencing operators of 8-th order convergence in the bulk of the grid, and 4-th order convergence at the boundaries. Time integration is performed with a 3-rd order accurate Runge-Kutta method of lines, satisfying total variation diminishing (TVD) property [92].

1.5 Constraint Damping

The constraint damping scheme depends on two freely-specifiable parameters, κ and γ_2. These parameters can be assigned per-point, i.e. the system of equations does not depend on their spatial or temporal derivatives. Here we describe how these parameters are specified in our simulations.

In this formulation, the set $u^\alpha = \{g_{ab}, \Phi_{iab}, \Pi_{ab}\}$ of dynamical fields consists of the metric g_{ab} and linear combinations of its derivatives $\Phi_{iab} = \partial_i g_{ab}$, $\Pi_{ab} = -n^c \partial_c g_{ab}$, where n^c is normal to a $t = \text{const.}$ hyperslice. The fields evolution equations can be written in the following form,

$$\partial_t g_{ab} = G_{ab}(x^a, u^\alpha), \tag{1.1}$$

$$\partial_t \Phi_{iab} = \mathcal{F}_{iab}(x^a, u^\alpha) - \gamma_2 C_{iab}, \tag{1.2}$$

$$\partial_t \Pi_{ab} = P_{ab}(x^a, u^\alpha) - \kappa C_{ab} - \gamma_2 \beta^i C_{iab}, \tag{1.3}$$

where C_{ab}, C_{iab} are the constraints, β^i is the shift vector, and G_{ab}, $\mathcal{F}_{iab}$, P_{ab} are right-hand sides of the formulation *without* the constraint damping terms. At the continuum limit, the constraints are zero, and the system (1.1) reduces to the original Einstein equations. At the discrete level, the constraints can be non-zero, and the constraint damping terms provide a non-vanishing contribution to the right-hand sides of the system (1.1). Since constraint damping terms should act only as small corrections to the evolution system, their contribution should not exceed that

of functions G_{ab}, $\mathcal{F}_{iab}$, P_{ab}. Otherwise, the evolution of the system will be dominated by the numerical constraint violations.

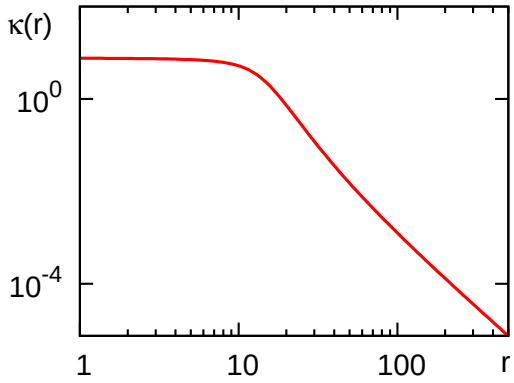

Figure 1.2: Radial dependence of the constraint damping coefficient κ in logarithmic scale. This coefficient stays approximately constant close to the BH and falls off like $1/r^4$ as $r \to \infty$.

We noticed that in our simulations the functions $\mathcal{F}_{iab}$, P_{ab} on the right-hand sides of (1.1) fall off as $1/r^{\alpha}$ with $\alpha \sim 4$ beyond $r > r_{\rm disk}$, where $r_{\rm disk}$ is the approximate outer radius of the disk. At the same time, the constraint violations C_{ab}, C_{iab} fall off as $1/r^{\beta}$ with $\beta \sim 1$. This means that if we use constant values for γ_2 and κ, the constraint damping terms will dominate the dynamics of the system for sufficiently large r. In order to avoid this situation, functions κ and γ_2 must fall off with radius as $\sim 1/r^3$.

We have found that the following radial profiles of κ and γ_2 for our simulations lead to satisfactory results:

$$\kappa(r) = \kappa_* \left[1 - \frac{2}{\pi}\left(\frac{r_*}{1+r_*^2} + \arctan r_*\right)\right] \tag{1.4}$$

$$\gamma_2(r) = \gamma_* \left[1 - \frac{2}{\pi}\left(\frac{r_*}{1+r_*^2} + \arctan r_*\right)\right] \tag{1.5}$$

where $r_* = (r - r_0)/\sigma$, and κ_*, γ_*, r_0, σ are (positive) constants. This radial profile (as depicted on Fig. 1.2) approaches a constant value of $\sim \kappa_*$ (or $\sim \gamma_*$) for $r < r_0$, and falls off as $\sim 1/r^3$ for $r \gg r_0$. The parameter σ determines the extent of the smooth transition region between these two regimes.

We used $\kappa_* = \gamma_* = 4$, $r_0 = 12$, and $\sigma = 8$ in our simulations. This profile of the constraint damping coefficients allows to impose strong constraint damping near the BH and the disk without introducing spurious dynamics far away from the origin.

Chapter 2. Code Tests

Numerical methods for solving the general relativistic hydrodynamics equations are inherently complex and the codes need to be thoroughly tested before they can be successfully applied to physical problems (see e.g. [93,94]). The code used in this work is based on an existing and well tested computational infrastructure. Our contribution was to couple the two existing codes and to test the resulting coupled system.

The hydrodynamics code THOR was tested by Zink et al. in [49], where it was demonstrated that the code can handle models representative of many astrophysical situations, including relativistic shocks, rotating polytropes and equilibrium tori around BHs [95].

The spacetime evolution code QUILT was tested by Pazos et al. [50], who used this code to study a perturbed Schwarzschild and Kerr metric in the context of an accurate wave extraction. Another test of the QUILT is presented in Chapter 12 of this thesis, where we demonstrate convergent evolutions of nonlinear Brill waves with wave extraction.

In this chapter, we report the results of two tests of the coupled hydrodynamics and spacetime evolution codes: the stable convergent evolution of a rapidly rotating polytropic star is reported in Section 2.1, and reproducing fundamental frequencies of a non-rotating polytropic star is reported in Section 2.2, These tests serve as prerequisites to our main work (reported in Chapters 5 and 6), which is to study non-axisymmetric instabilities in self-gravitating disks using 3D simulations in full GR.

2.1 Stable Evolution of a Uniformly Rotating Polytrope

In this section, we present results of testing the time evolution of a uniformly rotating polytropic star for numerical stability and convergence. In our tests, we use geometrized units based on the solar mass, in which $G = c = \mathcal{M}_\odot = 1$. The parameters of the star in the geometrized and

Table 2.1: Physical parameters of the uniformly rotating polytropic star used for the code tests, in geometrized and CGS units, where: R_p/R_e is the ratio of the polar to equatorial radii of the star, J/M^2 is its angular momentum, normalized with the square of the ADM mass of the star M, and $T/|W|$ is the ratio of the kinetic to binding energy of the star.

	geom.	CGS
polytropic scale K	100	$1.46 \cdot 10^5$ cm^{5}g^{-1}s^{-2}
polytropic index Γ	2	2
central rest-mass density ρ_c	0.001	$6.17 \cdot 10^{14}$ g cm^{-3}
ratio R_p/R_e	0.7	0.7
ADM mass M	1.49	1.49
rest mass M_0	1.59	1.59
equatorial radius R_e	12.32	$1.823 \cdot 10^6$ cm
angular momentum J	1.32	$1.16 \cdot 10^{49}$ g cm^{2}s^{-2}
normalized ang. mom. J/M^2	0.59	0.59
kinetic / binding en. $T/\|W\|$	0.0748	0.0748
angular velocity Ω	0.0215	4300 s^{-1}
Keplerian angular velocity Ω_K	0.0286	5801 s^{-1}
rotational period P	292.1	$1.44 \cdot 10^{-3}$ s

CGS units are summarized in Table 2.1. We use thirteen-block cubed sphere system that was described in [49] (see Fig. 1.1b and the related discussion in Section 1.1 above). For the current setup, we fix the sizes of the blocks by choosing $a = 2.5$, $R_{med} = 9$ and $R_{out} = 14$ (see Fig. 10.1b for definition of a, R_{med} and R_{out}), with each block having an equal number of N^3 grid cells. The sizes of the domain and its blocks are selected in such a way that the star occupies $\approx 90\%$ of the entire domain in radial equatorial direction, and the inner seven blocks of the system lie inside the star. This setup allows to test how much the accuracy and convergence of our numerical scheme are affected by interpolation errors on the interblock boundaries which thread the bulk of the star.

The stability of the numerical scheme for evolving the spacetime metric depends on the numerical dissipation parameter ϵ [76] and the constraint damping coefficients κ, γ_2 (see Section 1.5). In general, higher values of numerical dissipation restrict the timestep, while lower values are undesirable because they do not provide enough suppression of the numerical noise, which needs to be dissipated for stability [96]. For the current setup, we choose $\epsilon = 0.2$ and $\kappa = \gamma_2 = 0.1$. The values of the constraint damping parameters higher than ≈ 0.5 lead to

numerical instabilities in our simulations of stars.

Initial data for the time evolution is generated by the RNSID code [97], which uses the KEH(SF) method [97,98] to produce equilibrium models of stationary rotating relativistic stars. Since the RNSID is a 2D solver which uses its own grid that is different from the 3D multiblock grid of our time evolution code, we interpolate the data from 2D grid to the 3D multiblock grid using the 4-th order Lagrange interpolation. Also, because the variables in the GH formulation contain first derivatives of the metric and because the resolution on the 2D grid is usually much higher than on the multiblock 3D grid, we perform numerical differentiation on the 2D grid. The resulting derivatives are then interpolated onto the 3D grid. Note that the interpolation procedure is not consistent with the Einstein constraint equations, and hence produces constraint violations.

The system is evolved up to $t = 350$, which corresponds to 1.73 ms, or 10 dynamical timescales of the star[1]. In vacuum regions outside the star, we use artificial atmosphere, which has density of $\rho_{\rm atm} = 10^{-7}\rho_{\rm max}(0)$, where $\rho_{\rm max}(0)$ is the maximum density at $t = 0$. If during the evolution the density in a cell drops down below a threshold value set to $\rho_{\rm thr} = 2\,\rho_{\rm atm}$, the density in this cell is reset to the artificial atmospheric value. To estimate the accuracy of our code, we have performed convergence study using three different resolutions with $N^3 = 20 \times 20 \times 20$, $40 \times 40 \times 40$ and $80 \times 80 \times 80$ grid points in each block. We have analyzed various integral norms of the errors in all evolved variables, including 50 spacetime variables, 5 primitive variables and 5 conserved variables. We have also analyzed integral norms of the Hamiltonian and momentum constraints, as well as the behavior of conserved integral quantities such as total rest mass and total angular momentum.

In all cases, we observe the expected 2-nd order convergence. As an example, Fig. 2.1a shows the time evolution of the L_1 norm of the normalized density deviation $\delta\rho \equiv [\rho(t) - \rho(0)]\,/\rho_{\rm max}(0)$ for the three resolutions. Due to accumulation of truncation errors, this deviation exhibits a steady growth (modulo small variations because of oscillations of the star) throughout entire evolution. The deviation for $N = 40$ is larger than that for $N = 80$ by a factor of ≈ 4, which is a clear signature of 2-nd order convergence. However, the deviation for $N = 20$ is larger than that

[1]The dynamical time t_D is defined as $t_D = R_e\sqrt{R_e/M}$, where R_e is a proper equatorial circumferential radius, and M the ADM mass of the star. It corresponds to the inverse of the orbital frequency $\Omega = \sqrt{M/R_e^3}$ at R_e.

for $N = 40$ by a smaller factor of ≈ 1.5, which means that the resolution $N = 20$ is insufficient for achieving a convergent regime. A similar convergent behavior is observed for integral norms of the deviations of all of the rest of the variables.

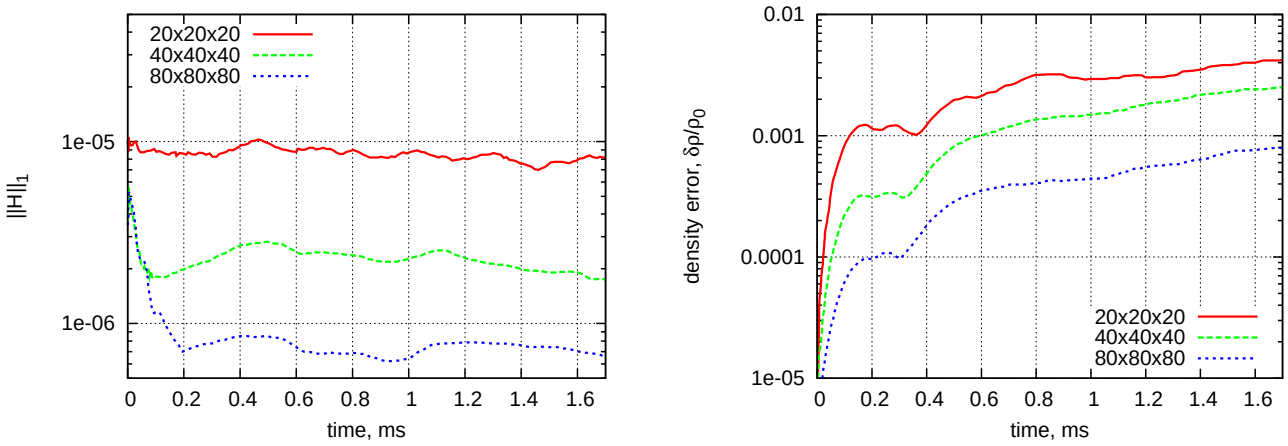

Figure 2.1: Time evolution of (a) L_1 norms of the Hamiltonian constraint; and (b) density solution error $\delta\rho/\rho_{max}(0)$ for three different resolutions.

Figure 2.1b shows the plot of the L_1 norm of the Hamiltonian constraint violation as a function of time. This quantity is not zero at $t = 0$, since initial conditions were interpolated from the 2D grid and interpolation errors were introduced. However, because of the constraint damping scheme, the Hamiltonian constraint violation significantly drops for medium and high resolutions within the first 0.2 ms. During subsequent evolution the value of the Hamiltonian constraint remains stable and clearly shows the 2-nd order of convergence with resolution, i.e. the values of the Hamiltonian constraint for $N = 20$, 40 and 80 are in an approximate ratio $16 : 4 : 1$. Momentum constraints show a similar behavior.

Figure 2.2 demonstrates time evolution of the total rest mass (left panel) and total angular momentum (right panel) of the star. In our numerical simulations these quantities are not conserved mostly due to interpolation errors on the interblock boundaries that pass through the bulk of the star. By the end of the simulation, for $N = 20$, 40 and 80, the total rest mass decreases by 0.88, 0.84 and 0.25 percent, while the total angular momentum decreases by 0.07, 0.12 and 0.05 percent. These numbers show that the smallest necessary resolution for the convergent regime is $N = 40$, which amounts to $\approx 70 - 100$ points across the star.

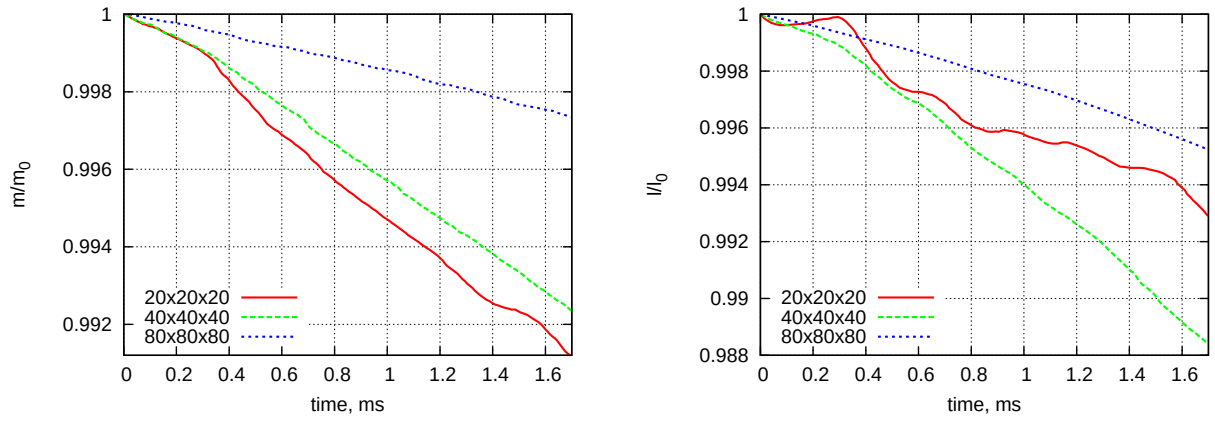

(a) (b)

Figure 2.2: Time evolution of: (a) the total rest mass, and (b) the total angular momentum for three different resolutions. Both quantities are normalized to their values at $t = 0$.

2.2 Fundamental Modes of a TOV Star

As another test of the coupling between the GR and hydro parts of the code, we evolved a Tolman-Oppenheimer-Volkoff (TOV) solution on a seven-block system, and measured the frequencies of its fundamental oscillations both in the Cowling approximation and in full GR. In these tests, we use geometrized units in which $G = c = \mathcal{M}_\odot = 1$. We choose a star with $\Gamma = 2$, $K = 100$ and the value of rest-mass density in the center $\rho_c = 1.28 \cdot 10^{-3}$. These parameters produce a TOV star with gravitational mass $M = 1.4$ and circumferential radius $R_e = 9.8$. This system has already been extensively studied in the literature and used for the assessment of relativistic hydrodynamical codes (e.g. [99,100]). The seven-block cubed sphere system that we used (see Fig. 10.1a) has the outer radius $R_{out} = 12$, which makes the star occupy 82% of the domain in radial direction and leaves extra room for small oscillations. The size of the cubical block in the center is $2a = 4.8$, placing it completely inside the star. The bulk of the star is therefore threaded by interpolation boundaries between the blocks. The cubical block contains N^3 volume cells, and the outer blocks have $N^2 \times (2N)$ cells. For the tests, we used resolutions $N = 20$, 40 and 80, which roughly correspond to 40, 80 and 160 points across the star.

To observe and measure the fundamental mode, we artificially add a small initial perturba-

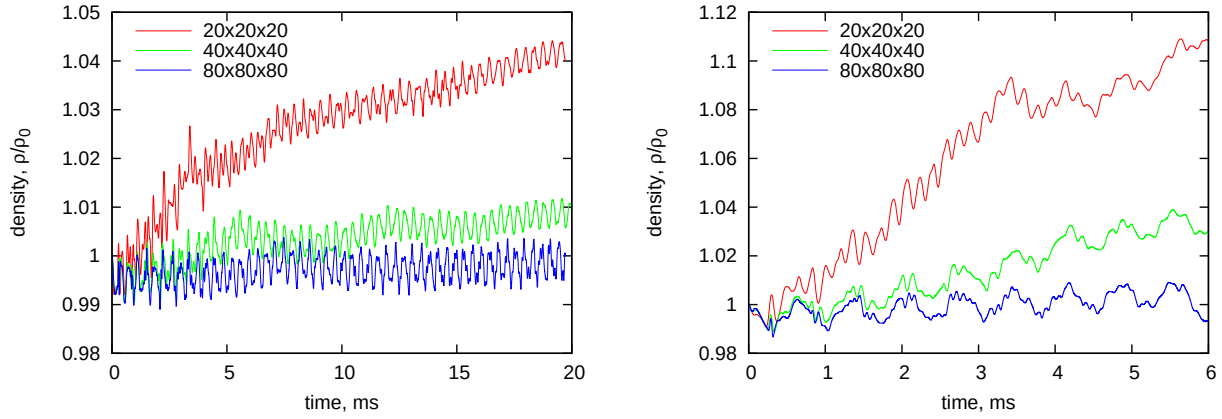

Figure 2.3: Time evolution of the density $\rho_c(t)$ at the center of a TOV star, normalized by its initial value ρ_0, for three different resolutions. Left panel: Cowling approximation. Right panel: fully dynamical GR case.

tion, roughly corresponding to the shape of the mode:

$$\frac{\delta\rho}{\rho} = A\cos\frac{\pi r}{2R_e},$$

The amplitude was chosen to be $A = 0.005$. Fig. 2.3 displays the resulting oscillatory behavior of the rest-mass density in the center of the star for three different resolutions. Left and right panels correspond to fixed (Cowling approximation) and dynamical spacetime geometries, respectively. Oscillations of the density are accompanied by a secular drift, which reflects accumulation of truncation errors and converges away with resolution at approximately second-order convergence rate. Conserved quantities such as the total rest mass and the total angular momentum (not shown) also exhibit the second-order convergence, as expected. In particular, for the Cowling approximation case, the simulation continued up to 20 ms, and the final rest mass is conserved up to 8.3, 3.7 and 1.1 percent for resolutions with $N = 20$, 40 and 80. For the full GR case, the simulation continued for 6 ms and the rest mass is conserved up to 3.2, 1.3, 0.4 percent for the same three resolutions. This shows that the rate of the mass loss in Cowling and full GR simulations is approximately the same, as expected. Because the bulk of the star is threaded by interpolation boundaries between the blocks, the mass loss is significantly higher in this setup than in case of a regular Cartesian grid, where we normally observe that the mass is conserved up to 7-8 significant digits for a similar resolution.

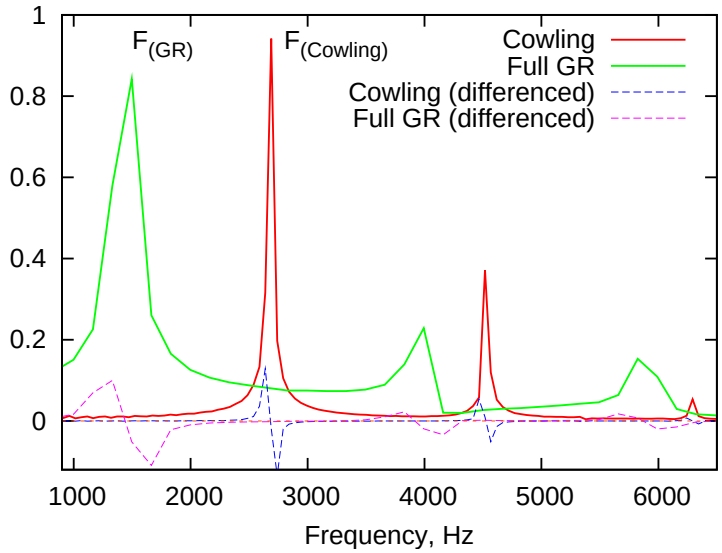

Figure 2.4: Power spectrum of the density oscillations $\rho_c(t)$ at the center of a TOV star for the highest resolution simulations in Cowling approximation (red solid line) and in full GR (green solid line). Also shown are derivatives of the power spectrum with respect to the frequency, obtained using the central finite-differencing scheme. The derivatives allow to localize peaks in the power spectrum more accurately. Vertical axis has arbitrary units.

A Fourier transform of $\rho_c(t)$ allows to measure the frequencies of the dominant oscillation modes. Fig. 2.4 shows the Fourier power spectrum of $\rho_c(t)$ in Cowling and full GR cases for simulations with the highest resolution $N = 80$. Both spectra contain three easily identifiable peaks corresponding to the fundamental radial modes F, H_1 and H_2. The same plot also shows derivatives of the spectral power with respect to the frequency, computed using the central finite differencing scheme. Zeroes of these numerical derivatives provide accurate estimates of the location of frequency peaks. The frequency of the F-mode in Cowling approximation is $\nu(F) = 2.684(40)$ kHz, which is in agreement with the value of 2.706 kHz, found in [100]. In the fully general relativistic case, we obtain the frequency $\nu(F) = 1.440(50)$ kHz, which also agrees with the value 1.458 kHz, found in [101]. Note that the error in the values of fundamental frequencies above is estimated as the distance between the root of the power spectrum derivative and the nearest point with a non-zero value.

Chapter 3. Self-gravitating Disks

Thick relativistic accretion disks and tori around BHs can form as transient structures in several astrophysical scenarios, including core-collapse of massive stars [22, 102] and merger of NS-NS and NS-BH binaries [103, 104]. In the general picture of relativistic figures of equilibrium [105, 106], the sequence of self-gravitating equilibrium tori around BHs branches off the sequence of quasi-toroidal stars [105, 107, 108].

Many models of gamma-ray bursts (GRBs) rely on the existence of massive dense accretion disks around BHs [102,109,110]. The observed $\sim 10^{51}$ erg energy powering GRBs [20,109,111] is believed to be coming either from the accretion disk and/or rotation of the central object. If this energy comes from the disk[1], then – assuming that the efficiency of converting disk energy into that of GRB can at most be $\sim 10\%$ as in many other astrophysical scenarios [114] – the accretion disk should have a mass of $\gtrsim 0.01\ \mathcal{M}_{\odot}$. Recent numerical simulations have demonstrated that the mass of the disk resulting from binary NS-NS (BH-NS) mergers – which are thought to be candidates for central engine of short GRBs – can be in the range of $\sim 0.01 - 0.2\ \mathcal{M}_{\odot}$ [104, 115] ($\sim 0.01\ \mathcal{M}_{\odot}$ [116]). Due to their larger initial mass, core-collapse of massive stars, which are believed to be progenitors of long GRBs[2] [22, 102], can perhaps produce much more massive disks.

The neutrino-annihilation mechanism for triggering GRBs [110], in which neutrinos emitted by the disk annihilate predominantly at the rotation axis to produce $e^+ - e^-$ pairs and deposit energy behind the jet, rely on super-Eddington accretion rates, which can take place only in

[1] In alternative models, the GRB is powered by the rotation energy of the central object. If the latter is a BH, then the rotation can be converted through Blandford-Znajek mechanism [112]. If the central object a NS, then its energy can be transformed through magnetic fields [23, 113].

[2] Note that although all of the long GRBs are believed to be produced by core-collapse of massive stars, not all of the latter can produce long GRBs: In order to produce a GRB, precollapse star is probably required to be rapidly rotating [102, 117, 118].

high-density ($\rho \sim 10^{12}$ g cm^{-3}) disks. Moreover, the efficiency of neutrino annihilation at the rotation axis and the requirement of a small baryon load of the relativistic ejecta [109, 111, 119] strongly favors a toroidal structure for accreting matter [120, 121].

The duration of prompt GRB emission is $\gtrsim 2$ s ($\lesssim 2$ s) for long (short) GRBs, while that of the later-time X-ray emission can be as long as $\sim 10^5$ s (e.g., [18]). Recent observations of GRB X-ray afterglows have revealed a variety of late-time emission processes, including plateaus, bright X-ray flares, chromatic breaks, some of which can persist up to $\sim 10^5$ s following the initial GRB prompt emission (see, e.g., [20] for a recent review). The amount of energy released in the late-time emission phase can be comparable to that produced during the prompt emission phase. Both the prompt and the late-time emissions can be explained as the result of the activity of the central engine (see, e.g., [18, 20]), although alternatives models exist [122–124]. If the emission energy comes from the disk, such a long duration of the observed GRB emission requires the disks to accrete in a quasi-stable manner for a sufficiently long period of time.

3.1 Runaway Instability

Early studies of the stability of accretion disks have revealed that they can be subject to several types of axisymmetric and/or non-axisymmetric instabilities in a number of circumstances [24, 25,27,41,82,125,126]. Instabilities can lead to highly variable and unstable accretion rates, posing a serious challenge to the viability of "accretion-powered" GRB models. The so-called dynamical runaway instability of thick accretion disks around BHs was first discovered by Abramowicz, Calvani & Nobili [125]. This instability is similar to the dynamical instability in close binary systems, when the more massive companion overflows its Roche lobe. In such a case, the radius of the Roche lobe shrinks faster than the radius of the companion, leading to a catastrophic disruption of the latter. In disk+BH systems, a toroidal surface analogous to the Roche lobe can be found. A meridional cut of this surface has a cusp located at the L_1 Lagrange point. If the disk is overflowing this toroidal "Roche lobe", then the mass-transfer through the cusp will advance the cusp outwards inside the disk. This can result in a catastrophic growth of the mass-transfer and disruption of the disk in just a few dynamical timescales.

Abramowicz et al. [125] studied the properties of mass transfer using many simplifying as-

sumptions: a pseudo-Newtonian potential for BH gravity [127], constant specific angular momentum of the disk, and approximate treatment of the disk self-gravity. They found that the runaway instability occurs for a large range of parameters, such as the disk radius and the disk-to-BH mass ratio $M_{\rm D}/M_{\rm BH}$. Subsequent and somewhat more detailed studies found that the rotation of the BH has a stabilizing effect [37, 128], while non-constant radial profile angular momentum was found to strongly disfavor the instability [35, 37, 42, 129]. Moreover, studies using a Newtonian pseudopotential for the BH [38, 130] and relativistic calculation with fixed spacetime background [126, 131] found indications of the self-gravity of the disk to favor the instability. However, Montero et al. [43] recently performed the first self-consistent and fully general relativistic simulations of thick accretion disks around BHs in axisymmetry for a few dynamical timescales. They found no signatures of a runaway instability during the simulated time, perhaps implying that the self-gravity of the disk does not play a critical role in favoring the instability, at least during the first few dynamical timescales.

3.2 Non-axisymmetric Instabilities

The problem of the existence and development of non-axisymmetric instabilities has a long history. For thin Keplerian self-gravitating disks it was found that the Toomre parameter [132–134] can be used to determine stability against both local clumping or fragmentation, and formation of global non-axisymmetric modes. For thick pressure-supported disks, Papaloizou and Pringle discovered [24] the existence of a global hydrodynamical instability that develops on a dynamical timescale in disks with negligible self-gravity and constant specific angular momentum. A follow-up publication [25] found this instability also in disks with power law distribution of specific angular momentum $\ell(r) = \ell_0 (r/r_c)^{2-q}$ for all $q > \sqrt{3}$. Kojima [27, 28] found the Papaloizou-Pringle (PP) instability in equilibrium tori on a fixed Schwarzschild background [95] using a linearized perturbative approach.

Subsequent works clarified the nature of the PP instability [26, 29, 135, 136], established how it redistributes specific angular momentum [137] and discovered that accretion has a stabilizing effect on the disk [138, 139]. In particular, Narayan et al. [26] showed that the PP modes are formed by two boundary wave-like perturbations with energy and angular momentum of

opposite signs that are coupled across a forbidden region near the mode corotation radius. For wide disks around BHs, the accretion suppresses the development of the inner boundary wave and therefore has a stabilizing effect on PP modes [138,139]. For slender disks, the development of PP modes is mostly unaffected by accretion [139]. The PP instability itself amplifies accretion by exerting torques on the disk and redistributing specific angular momentum [137].

When the self-gravity of the disk has been taken into account, it was found [30–32] that two new types of non-axisymmetric instabilities appear, while the PP instability disappears for most of the models and remains only in slender models with a low value of self-gravity. The first type of unstable modes (J-modes) appears in strong self-gravity regime, and it is an analog of the classical Jeans instability. The second type of unstable modes was found in the strong and medium self-gravity regimes [30]. The modes of this type are referred to as intermediate modes (I-modes) and represent elliptic deformations of the disk (or triangular, square, etc. deformations for higher azimuthal numbers – see e.g. [32]).

Yet another type of instability, so-called "eccentric instability" was discovered in [140] for thin nearly Keplerian self-gravitating disks when the central mass was allowed to move. An elaborate mechanism called "SLING amplification" [141] was proposed to describe this instability. Subsequent investigation [142] of this instability in thin disks suggested a different mechanism and predicted that the system is dynamically unstable only when the mass of the disk exceeds the mass of the central object.

In [82], Woodward, Tohline and Hachisu presented an extensive parameter study of thick self-gravitating disks in Newtonian gravity to determine the type, growth rate and pattern speed of non-axisymmetric modes. The central mass in their simulations was allowed to move, and they used 3D time evolutions of the disk models with wide range of parameters, including disk-to-central object mass ratios $M_{\rm D}/M_c = 0, 1/5, 1$ and ∞. Another study of the principal modes in thick self-gravitating disks with fixed central objects was performed in [143].

Several recent publications address accretion disks and instabilities in these disks in context of GRB central engines. In [115], Rezzolla et al. studied the properties of accretion disks resulting from binary NS mergers. They obtained almost Keplerian accretion disks with masses $\sim 0.01 - 0.2\ \mathcal{M}_\odot$ and no evidence of growing non-axisymmetric modes or runaway instability. In [144],

Taylor, Miller, and Podsiadlowski used 3D SPH simulations with detailed microphysics and neutrino transport to follow a collapse of an iron core up to the formation of a thin massive accretion disk and development of global non-axisymmetric modes. They found that torques created by the non-axisymmetric modes provide the main mechanism for angular momentum transport, leading to high accretion rates of $\sim 0.1 - 1\ \mathcal{M}_{\odot}/\mathrm{s}$, which may create a favorable conditions for powering GRBs.

3.3 Purpose of This Work

Despite significant theoretical and computational effort, previous studies of the runaway instability do not give a definite answer to the question of its existence in general case. Additionally, it remains unclear if and how the non-axisymmetric dynamics may affect the likelihood of the runaway instability in such models. It is important to create a comprehensive overall picture of the stability of accretion disks for wide range of parameters. The aim of the work reported in this paper is to investigate stability of the disk against non-axisymmetric and runaway instabilities using three-dimensional hydrodynamical simulations in full GR. We study slender and moderately slender disks with constant distribution of specific angular momentum, which are expected to be more unstable both to runaway [35,129] and to non-axisymmetric instabilities [138,139].

We model our disks using the ideal fluid approximation (i.e. without viscosity) with a Γ-law equation of state (EOS) and $\Gamma = 4/3$. We do not include additional physics such as magnetic fields or neutrino and radiation transport due to the complexity and computational cost of the resulting problem. Nevertheless, the adopted approach will allow us to identify GR effects which can operate in more complex setting that include more realistic microphysics, neutrino/radiation transport and magnetic fields. Also, we limit ourselves to the case of non-rotating BHs, while the case of rotating BHs will be studied in our future publications.

Chapter 4. Initial Setup

We set up initial equilibrium disk configurations by solving Einstein constraints using a version of the RNSID solver [97] adapted to the problem of equilibrium tori. The method of solution is similar to the one used in [145]. The spacetime is assumed to be stationary, axisymmetric, asymptotically flat and symmetric with respect to reflections in equatorial plane. The metric is a general axisymmetric metric in quasi-isotropic coordinates:

$$ds^2 = -\lambda^2 dt^2 + e^{2\alpha}(dr_*^2 + r_*^2 d\theta^2) + B^2/\lambda^2 r_*^2 \sin^2\theta (d\varphi - \omega dt)^2. \tag{4.1}$$

where $(t, r_*, \theta, \varphi)$ are the coordinates, and λ, α, B and ω are metric potentials which depend only on r_* and θ. The RNSID code implements the KEH(SF) method [97, 98], in which the Einstein equations for the metric potentials λ, B and ω are transformed into integral equations [145] using Green's functions for the elliptical differential operators. The remaining metric potential α can then be found by integrating an ordinary differential equation, once the rest of the potentials are known. The KEH(SF) method uses compactified radial coordinate s which maps the region $[0, \infty)$ into a segment $[0, 1]$:

$$s \equiv \frac{r}{r + r_+}$$

where r_+ is the outer radius of the disk. The boundary conditions are imposed at symmetry interfaces and at the event horizon. The latter can always be transformed to a sphere of compactified radius s_h, while preserving the form of the metric given above [145]. At the horizon, we impose the boundary conditions for a non-rotating BH: $\lambda = B = \omega = 0$, and we set $B/\lambda = e^{\alpha}$ at the symmetry axis. The corresponding integral equations are then solved using Newton-Raphson iterations [97] in the upper quadrant $\theta \in [0, \pi/2]$, $s \in [0, 1]$ of the meridional plane.

The resulting quasi-isotropic metric is degenerate at the event horizon, which is very prob-

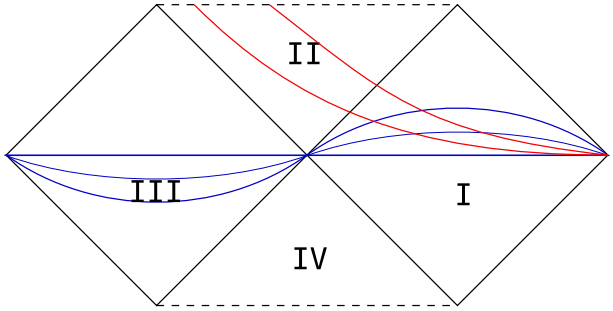

Figure 4.1: Conformal Penrose diagram of an axisymmetric spacetime, consisting of a non-rotating BH, distorted by a massive stationary disk around it. Each point on the diagram corresponds to a spheroid, located at a given geodesic distance from the BH horizon. Blue lines represent a quasi-isotropic foliation of the spacetime, while red lines show a horizon-penetrating foliation.

lematic for the evolution with excision of the BH interior using the generalized harmonic formulation, since this method requires coordinates without pathologies at the event horizon. This situation is best illustrated by a conformal picture of the complete spacetime, shown in Fig. 4.1. All quasi-isotropic slices meet the horizon of the BH at its throat, which makes the metric degenerate at the horizon. Regions II and IV are not covered by the quasi-isotropic foliation. It is necessary for our time evolution methods to have a time-independent foliation which penetrates the horizon and continues in region II rather than region III.

There are several options to address this issue:

(1) solve the complete system of equations in horizon-penetrating coordinates rather than quasi-isotropic ones;

(2) use puncture initial data, as developed in [146], and choose such a gauge for the evolution that after some time the spatial slices move from region III to region II, similarly to what happens with punctures in the BSSN formulation and $1 + \log$ slicing [147];

(3) apply a spacetime coordinate transformation from quasi-isotropic to horizon-penetrating coordinates. Since there is still no solution provided in region II, it needs to be extrapolated into that region.

We use option (3), since it is easier to implement in the context of the generalized harmonic system, and fits more naturally in the gauge choice employed by RNSID. Details on the spacetime

transformation that we apply to the initial data can be found in Appendix A.

4.1 Blending Numerical and Analytical Metrics

We could not extrapolate the initial data produced by the elliptic solver to the region II inside the horizon, because the data does not have enough smoothness near the horizon. The problem with initial data at the horizon seems to be similar to the problem with Gibbs phenomena, when solutions exhibit an oscillatory behavior and a lower order of convergence near a stellar surface. To handle this problem, we use an approximation, which combines the numerical metric in the region where it is accurate with the analytic Kerr-Schild solution of the same mass. We use a finite-size blending zone between the two metrics to avoid discontinuities. The blending of two different metrics introduces constraint violations in the system.

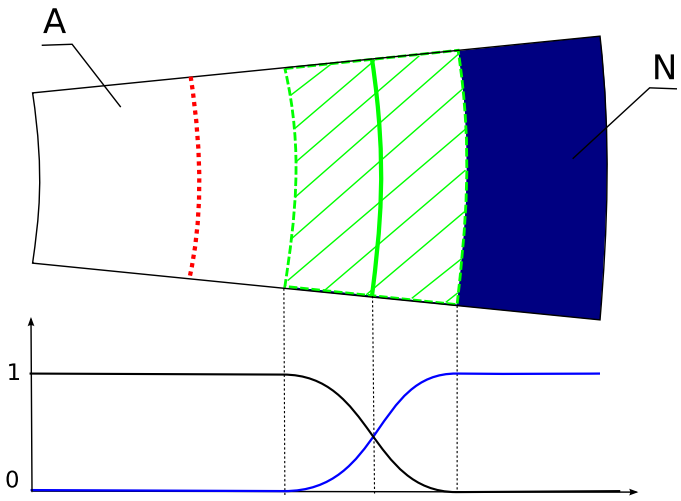

Figure 4.2: Blending the analytic (A) and numerical (N) metrics. The red line signifies location of the event horizon. Two metrics are added with smooth weight functions which add up to 1.

Fig. 4.2 illustrates how the blended initial data are constructed. The blended metric is a weighted sum of two metrics with smooth weight functions which add up to 1. The weight functions are non-constant only in a narrow spherical layer located outside the horizon.

Blending two metrics introduces constraint violations at the continuum level, but they quickly subside due to the constraint damping. The constraint damping scheme, however, doesn't respect the conservation of mass, so after the constraint violations are suppressed, the system arrives at a different state, which can be characterized as a close equilibrium configuration with

an imposed axisymmetric gravitational perturbation.

The location and width of the blending layer can be adjusted to minimize the initial unphysical jump in a BH mass and constraint violations. For the evolutions presented below, we used the radius of the blending layer $1.1r_{AH}$ and the width $0.05r_{AH}$, where the r_{AH} is the radius of the apparent horizon.

4.2 Initial Disk Models

We have prepared three initial disk models with disk-to-BH mass ratios $M_{\rm D}/M_{\rm BH} = 0.235, 0.174$ and 0.108, labeled A, B and C. Model C is slender, which means that its width is much smaller than the radius the torus, i.e. $r_c \gg (r_+ - r_-)$. Models A and B are moderately slender, i.e. for these models $r_c \approx (r_+ - r_-)$. Fig. 4.3 shows the contours of the disk surfaces for our models and the location of black hole horizon in the meridional plane. All models are constructed using a polytropic equation of state with polytropic index $\Gamma = 4/3$, constant specific entropy, and a constant specific angular momentum distribution.

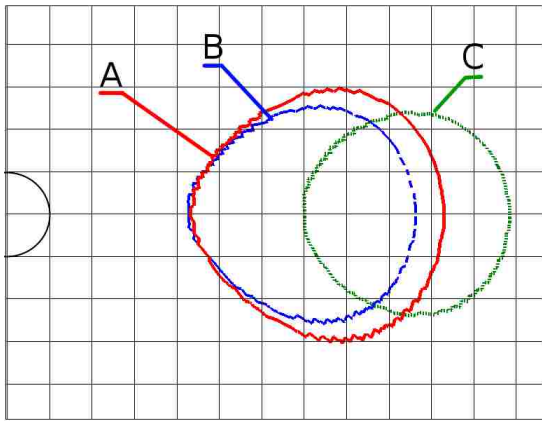

Figure 4.3: Contours of the disk surfaces for models A, B and C, and the location of black hole horizon in the meridional plane.

Table 4.1 lists physical and geometrical parameters of the disk, including the ratio of disk to BH mass $M_{\rm D}/M_{\rm BH}$, the ratio of kinetic energy T to potential energy W and the self-gravity parameter τ. The self-gravity parameter τ can be defined as ρ_c/ρ_{sph}, where $\rho_{sph} \equiv \Omega_c^2/4\pi G$ is the density of a uniform sphere with radius r_c, that creates equivalent gravity at that radius. Notice that $T/|W|$ correlates to the "slenderness" of the disk r_-/r_+. The value of specific an-

Table 4.1: Physical parameters of the self-gravitating initial disk models, used in our simulations.

Model	A	B	C
Specific angular momentum $\ell[M_{\rm BH}]$	4.50	4.32	4.87
Polytropic constant $K[10^{14}{\rm cm}^3{\rm g}^{-1/3}{\rm s}^{-2}]$	1.28	1.04	0.519
Maximum density $\rho_c[10^{13}{\rm g/cm}^3]$	1.23	1.17	0.755
Disk-to-BH mass ratio $M_{\rm D}/M_{\rm BH}$	0.235	0.174	0.108
Kinetic to potential energy $T/\lvert W\rvert$	0.479	0.497	0.499
Central radius r_c/r_g	6.51	5.58	8.23
Ratio of inner to central radius r_-/r_c	0.655	0.655	0.756
Ratio of inner to outer radius r_-/r_+	0.385	0.407	0.600
Orbital frequency at r_c, $\Omega_c[{\rm s}^{-1}]$	1713	1912	1121
Self-gravity parameter $\tau = 4\pi G\rho/\Omega_c^2$	3.52	2.68	5.04

gular momentum ℓ is given in units of the BH mass. These parameters allow us to make qualitative and quantitative comparisons between our models and the models studied in previous works [30–32, 82, 143].

4.3 Adapted Curvilinear Grid

In order to accurately resolve both the disk and the BH while minimizing the computational cost, we have designed a series of curvilinear multiblock grids adapted to each of the disk models. To obtain such a grid, we start from a six-block system (displayed on Fig. 1.1c) that was previously used in QUILT for computationally efficient and numerically accurate simulations of perturbed BHs [50]. We apply a radial stretching and an angular distortion to the six-block system so as to create a uniformly high resolution near the BH, nearly cylindrical grid near the disk, and approach a regular six-block spherical grid in the wave zone. These mappings are described in detail below. Figure 1.1d shows an illustration of the grid distortion, while Fig. 4.4a shows the actual curvilinear grid used in some of our simulations.

A regular six-block system consists of two polar blocks (near the z-axis) and four equatorial blocks (near the xy-plane). We can assign quasi-spherical coordinates $\{r, \theta, \varphi\}$ and $\{r, \theta_1, \theta_2\}$ to the equatorial and polar blocks, respectively. They can be related to the Cartesian coordinates $\{x, y, z\}$ by the following transformation:

(a) for an equatorial block in the neighborhood of the positive x axis:

$$\begin{aligned} x &= r/\sqrt{1+\tan\varphi^2+\tan\theta^2}, \\ y &= x\tan\varphi, \\ z &= x\tan\theta, \end{aligned}$$

(b) while for a polar block in the neighborhood of the positive z axis:

$$\begin{aligned} x &= z\tan\theta_1, \\ y &= z\tan\theta_2, \\ z &= r/\sqrt{1+\tan\theta_1{}^2+\tan\theta_2{}^2}. \end{aligned}$$

(c) The remaining blocks are obtained by applying symmetry transformations.

We set the coordinate ranges for the polar blocks to be $r \in [R_{min}, R_{max}]$, $\theta_1, \theta_2 \in [-\theta_*, \theta_*]$, where the value of θ_* controls an opening angle of the polar blocks. For equatorial blocks, $r \in [R_{min}, R_{max}]$, $\theta \in \left[-\frac{\pi}{2}+\theta_*, \frac{\pi}{2}-\theta_*\right]$ and $\varphi \in \left[-\frac{\pi}{4}, \frac{\pi}{4}\right]$. The size of the numerical grid for each block is fixed by three numbers: N_r, N_x and N_z. The equatorial blocks have $N_r \times N_x \times N_z$ cells, and the polar ones have $N_r \times N_x \times N_x$ cells (see Fig. 10.1c).

In order to obtain a variable radial resolution, we apply a smooth one-dimensional radial stretching $S : r \to \bar{r}$ that yields the desired resolution profile $\Delta_r(r)$. This profile is chosen based on several stringent requirements imposed by an accuracy and available computational resources. First, there need to be at least 8 grid points between the excision radius and the BH horizon in order to prevent constraint violations from leaving the interior of the BH (this question is considered in some detail in [148]), as well as to allow for some (restricted) BH movement. Second, our convergence tests show that near the disk, the grid needs to allow for at least 40 points across the disk in order to achieve a global convergent regime in hydrodynamical evolutions. For this purpose, the radial resolution profile is adapted to have sufficiently high resolution near the disk as well. Third, in the wave zone, there is no need to maintain very high radial resolution. However, this resolution needs to be uniform (rather than, for example, exponentially decreasing) to be able to carry the radiation accurately without dissipation. All these

requirements result in the radial resolution profile $\Delta_r(r)$ shown on Fig. 4.4b.

The resolution in the θ direction Δ_θ near the disk also needs to have at least 40 points across the disk for convergence. However, simple increase of N_θ in the six-block system leads to a very small minimal grid step Δ_{min} at the excision radius R_{min} that is too restrictive for the time step due to CFL condition. To increase the grid resolution in the θ-direction near the disk only, we apply a radial-dependent distortion to the angular coordinates θ, θ_1 and θ_2:

$$\begin{aligned} \theta(\bar{\theta}, r) &= \bar{\theta}(1 - \beta(r)\tfrac{\cos 2\theta_*}{\pi - 2\theta_*}), \\ \theta_i(\bar{\theta}_i, r) &= \bar{\theta}_i(1 + \beta(r)\tfrac{\sin 2\theta_*}{2\theta_*}), \quad \text{i = 1,2} \end{aligned}$$

where the function $\beta(r)$ is the amplitude of the distortion, chosen to have a Gaussian profile $\beta(r) = \beta_* \exp(-(r - r_0)^2/\sigma^2)$, in which the parameters β_*, r_0 and σ are chosen to satisfy the above requirements. This distortion bends diverging radial coordinate lines towards equatorial plane around the radius r_0, making the grid resemble a cylindrical shape near that radius (as illustrated by Fig. 4.4a). Figure 4.4b shows the dependence of Δ_θ on r along the x-axis (dotted black line) and along the z-axis (dash-dotted red line). The radial-dependent θ-distortion increases Δ_θ on the x-axis at the expense of Δ_θ on the z-axis near the disk. Away from the disk, the distortion vanishes and Δ_θ approaches the linear dependence $\Delta_\theta(r) \propto r$.

Figure 4.4 shows an example of the resulting curvilinear grid. For this example, $\theta_* = 30^o$, $N_\theta = 49$ and $N_\varphi = 25$. These parameters make the grid spacing approximately uniform in angular direction near the BH and at large r. The inner (excision) radius is $R_{min} = 1.3$ and the outer one is $R_{max} = 500$, while the minimum grid spacing is $\Delta_{min} = \Delta_\theta(r_{min}) \approx 0.06$. The apparent horizon has radius of ≈ 1.7, so that as many as 8 grid points can be placed inside the horizon without decreasing the minimum grid spacing. Distortion parameters of the Gaussian have values $r_0 = 12$, $\sigma = 8$, and $\beta_* = 1.3$, which is sufficient to concentrate about 40 grid points across the disk in the vertical direction. The radial resolution is adapted to be $(\Delta_r)_{BH} \approx 0.06$ at the excision sphere, $(\Delta_r)_{disk} \approx 0.25$ around the disk, and $(\Delta_r)_{wz} \approx 5.2$ in the wave zone.

All of the time evolutions described in the next two Sections 5 and 6 use adapted six-block curvilinear grids. Table 4.2 summarizes dimensions and resolutions of the grids for each of the

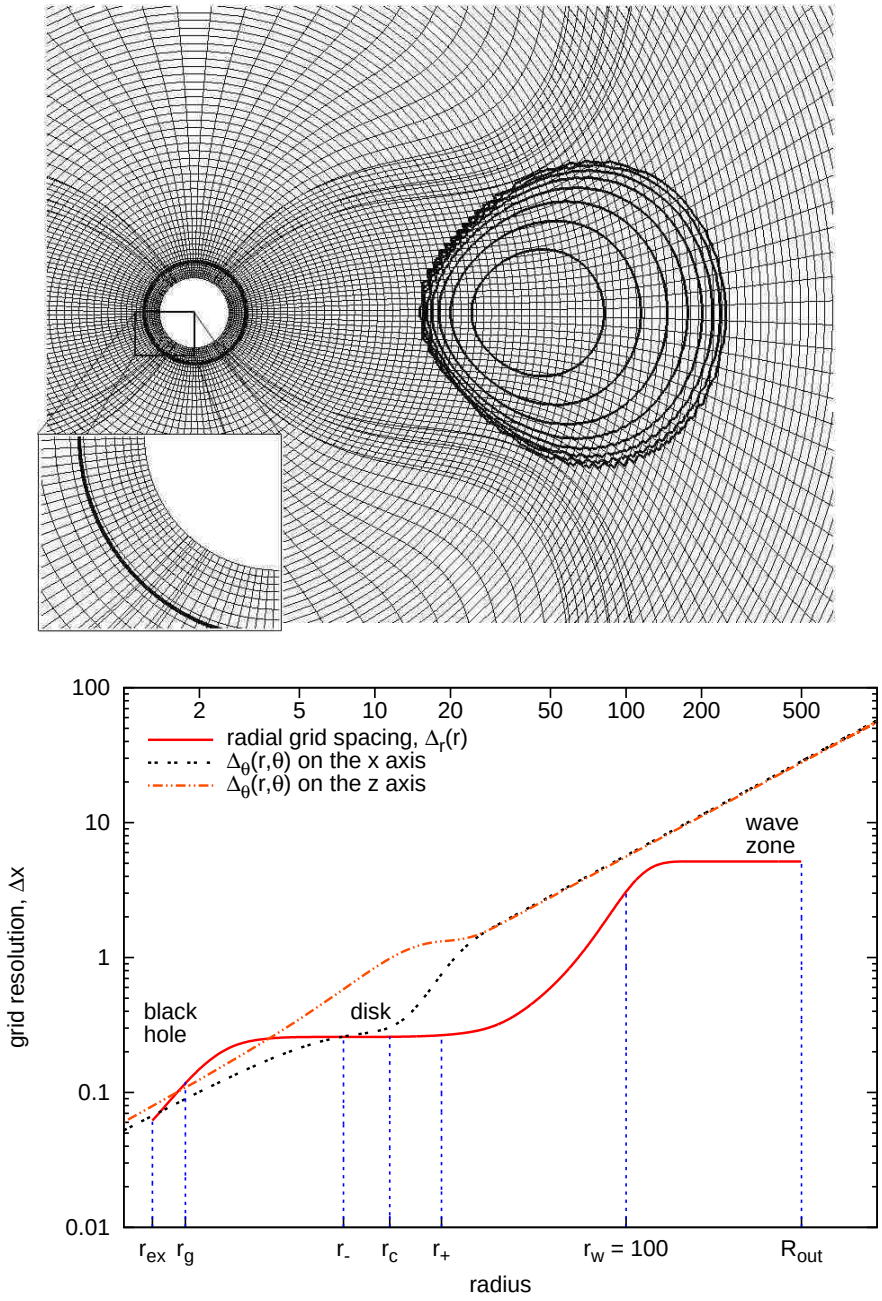

Figure 4.4: The top panel: meridional cut of an adapted curvilinear grid used in one of our simulations, combined with the logarithmic density contours of the disk at $t = 0$. The intersecting radial coordinate lines belong to the neighboring blocks in the overlapping (interpolated) regions. The thick black circle marks a location of an apparent horizon of the BH. The inset in the lower left corner of the plot shows the high-resolution grid around the BH, adapted in such a way that the resolution is uniformly high in every direction. The bottom panel: radial profile of the resolution in the r (red solid line) and the θ (dotted lines) directions for the grid shown in the top panel. The radial coordinate is plotted in logarithmic scale. The top horizontal axis shows the values of the radius in numerical units. The marks on the lower axis are: r_{ex} is the radius of the BH excision sphere; r_g is the gravitational radius of the BH; r_-, r_+ is the inner and outer radii of the disk; r_c is the radius of the density maximum; r_W is the "wave extraction" radius; R_{out} is the outer radius of the domain. The black dotted line is the resolution in the θ-direction on the x axis, and the red dashed-and-dotted line is the resolution in the θ-direction on the z axis.

simulations used in these two sections. The first column lists simulation names, which consist of two or three symbols. Models K1-K6 are considered in Section 6.1. In the rest of the model names, the first letter denotes the initial disk model (A, B or C), the second letter signifies whether the simulation is evolved in full GR (F) or Cowling (C) approximation (see corresponding Sections 6.2 and 6.3). The next number (if present) is the azimuthal number m of an added non-axisymmetric perturbation (as explained in Section 6). Simulations AFc, AF and AFf represent disk model A evolved in full GR using coarse, medium and fine resolution grids. These models are used in Chapter 5 for convergence studies. Finally, note that the adapted curvilinear grid example above (displayed in Fig. 4.4) corresponds to the the grid used in simulation AF, and the grids of simulations AFf and AFc are obtained by increasing and decreasing the resolutions in the AF grid by a factor of $3/2$.

4.4 Data Analysis

To identify and characterize non-axisymmetric instabilities, we will adopt an approach commonly used in linear perturbative studies of accretion disks (e.g. in [28, 82]). Namely, we analyze first few terms in Fourier expansion in angle φ of the disk density $\rho(r, \varphi)$ on a sequence of concentric circles in the equatorial plane:

$$\rho(t, r, \varphi) = \bar{\rho}(t, r) \left(1 + \sum_{m=1}^{\infty} D_m e^{-i(\omega_m t - m\varphi)} \right).$$

where $\bar{\rho}$ is a φ-averaged density at a given radius. The quantity D_m represents the (complex) amplitude of an azimuthal mode m, the real part of the quantity ω_m determines a mode pattern speed, while its imaginary part determines a mode growth rate. Following [82, 149], we quantify the growth rate and the pattern speed of a non-axisymmetric mode by two dimensionless parameters y_1 and y_2, defined as

$$y_1(m) = \frac{\mathrm{Re}(\omega_m)}{\Omega_{orb}} - m, \qquad y_2(m) = \frac{\mathrm{Im}(\omega_m)}{\Omega_{orb}}.$$

We calculate a value of the parameter $y_2(m)$ from a slope of $\log |D_m|$ versus t at an arbitrary radius, while $y_1(m)$ is obtained from a slope of the mode phase angle $\varphi_m = \varphi_m(t)$. Notice that

Table 4.2: Parameters of numerical grids for all the simulations of accretion disks used in this study. The naming convention of the simulations is explained in the main text in Section 4.3 on adapted curvilinear grids. All resolutions and linear dimensions are given in computational units. The first column, which lists the values of the BH gravitational radius r_g, allows to convert all quantities from computational to CGS units. The remaining columns contain: R_{min}, R_{max} are radial extents of the computational domain; N_x is the number of grid points in the horizontal x- or y-direction; N_z is the number of grid points in the vertical direction; N_r is the number of grid points in the radial direction; Δ_{min} is the minimal grid step size, in θ direction at the excision sphere; $(\Delta_r)_{disk}$ is the resolution in the r-direction at radius r_c; $(\Delta_\theta)_{r_c,x}$ is the resolution in the θ-direction on the x-axis at radius r_c; $(\Delta_\theta)_{r_c,z}$ is the resolution in the θ-direction on the z-axis at radius r_c; $(\Delta_r)_{wz}$ is the radial resolution in the wave zone (not used for simulations on fixed background).

Model	r_g	R_{min}	R_{max}	$N_x \times N_z \times N_r$	Δ_{min}	$(\Delta_r)_{disk}$	$(\Delta_\theta)_{r_c,x}$	$(\Delta_\theta)_{r_c,z}$	$(\Delta_r)_{wz}$
K1	2.0	4.0	30	$25 \times 49 \times 96$	0.07	0.25	0.32	0.72	–
K2	2.0	4.0	25	$25 \times 49 \times 96$	0.07	0.25	0.32	0.72	–
K3	2.0	4.0	22	$25 \times 49 \times 96$	0.09	0.20	0.17	1.28	–
K4	2.0	6.0	17	$25 \times 49 \times 96$	0.08	0.18	0.13	1.68	–
K5	2.0	7.0	16	$25 \times 49 \times 96$	0.03	0.10	0.05	0.50	–
K6	2.0	8.0	14	$25 \times 49 \times 96$	0.02	0.08	0.03	0.53	–
AC, AC1, AC2	1.760	1.7	25	$37 \times 73 \times 144$	0.05	0.17	0.21	0.48	–
BC, BC1, BC2	1.806	1.7	25	$37 \times 73 \times 144$	0.05	0.17	0.21	0.48	–
CC, CC1, CC2, CC3	1.812	1.7	25	$37 \times 73 \times 144$	0.05	0.16	0.16	0.54	–
AF, AF1, AF2	1.760	1.3	500	$25 \times 49 \times 280$	0.06	0.25	0.22	0.95	5.2
AFc	1.760	1.3	1000	$17 \times 33 \times 180$	0.09	0.37	0.33	1.43	7.8
AFf	1.760	1.3	1000	$37 \times 73 \times 420$	0.04	0.17	0.15	0.62	3.4
BF, BF1, BF2	1.806	1.3	1000	$25 \times 49 \times 280$	0.06	0.25	0.22	0.95	5.2
CF, CF1, CF2, CF3	1.812	1.3	1000	$25 \times 49 \times 280$	0.06	0.22	0.22	1.01	5.2

because the modes that we consider are global, their growth rates and pattern speeds do not depend on a radius.

We use the parameter $y_1(m)$ to obtain the value of a corotation radius r_{cr} for a given mode: using the mode pattern speed,

$$\Omega_p = \Omega_{orb}\left(1 + \frac{y_1(m)}{m}\right),$$

and the radial profile $\Omega = \Omega(r)$ of a fluid angular velocity in the disk, we can calculate r_{cr} from the equation $\Omega(r = r_{cr}) = \Omega_p$.

In those simulations where the disk is oscillating radially, the values of the mode amplitudes at a given radius oscillate with the disk, which makes it more difficult to extract their growth rates. For such cases we found that more accurate growth rates can be obtained if we use nor-

malized root mean squared (RMS) mode amplitudes G_m, defined as:

$$G_m = \langle D_m \rangle_2 \,/\, \langle D_0 \rangle_2$$

where the angle brackets $\langle \dots \rangle_2$ denote an RMS value over radii from r_- to r_+:

$$\langle D_m \rangle_2 \equiv \frac{1}{r_+ - r_-} \left(\int_{r_-}^{r_+} |D_m|^2 dr \right)^{1/2}$$

Chapter 5. Time Evolution

In this chapter, we present the results of the fully general relativistic time evolution of the initial data for the reference model A, constructed as described above in Section 4. Overall, the dynamics of model B is qualitatively similar to that of A, while model C exhibits a qualitatively different time evolution. The BH initial mass in all of our models is 2.5 $\mathcal{M}_{\odot}$, as in some of the previous works [39,41,42], and the disk rotational period $t_c = 3.667$ ms is used as a unit of time in all of the plots in this section.

At the beginning of time evolution, the metric blending procedure (described earlier in Section 4.1) introduces axisymmetric constraint-violating perturbation to the spacetime near the BH, causing an unphysical oscillation in the BH mass, which damps out in about one orbital period of the disk. We discard the first orbital period when drawing physical conclusions and analyzing simulation data. In the meanwhile, the axisymmetric perturbation propagates outwards and triggers axisymmetric disk oscillations. Disk oscillations lead to formation of shock waves, which transform kinetic energy of the shock to the thermal energy, resulting in damping of the oscillations. We discuss different aspects of the dynamics of the disk in more detail below.

After about three orbital periods, the disk develops an $m = 1$ non-axisymmetric mode, which we have identified as Papaloizou-Pringle (PP) type instability [24,25] (discussed in more detail below in Chapter 6). The same type of mode develops in model B, while the more slender model C develops an $m = 2$ mode of an intermediate type (see Section 6.3). As the $m = 1$ mode grows, the center of mass of the disk drifts away from its initial position along a spiral-like trajectory, as shown in Fig. 5.1 (red squares). As a result of gravitational interaction between the deformed disk and the BH, the latter also starts spiraling away, mirroring the motion of the disk center of mass, as shown in Fig. 5.1 (black line). This plot also shows dashed lines that connect the positions of the center of mass of the BH and the disk at different moments of time. As we can

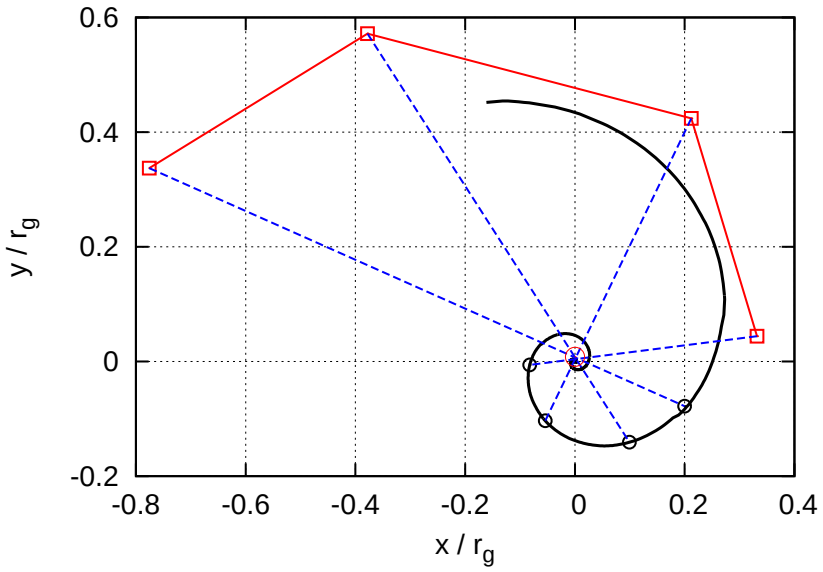

Figure 5.1: Trajectories of the center of mass of the accretion disk (red line) and the BH (black line). Dashed lines show four consecutive simultaneous locations of the two centers of mass, and a small red circle at the origin marks the location of their common center of mass. The spiral motion of the BH is caused by the development of the non-axisymmetric $m = 1$ mode in the disk.

see, all of the these lines intersect with each other at one point at the initial location of the center of mass of the disk-BH system, implying that the center of mass of the system does not move, as should be the case for BH motion caused by physical interaction with the disk (but not gauge effects). Notice that the mass loss due to emission of GWs is negligible in this case.

Fig. 5.2 shows the time evolution of the amplitude $|D_1|$ of the $m = 1$ PP non-axisymmetric mode and the distance $r_{\rm BH}$ (normalized to $r_{\rm g}$) from the BH center to its initial position. As we can see, both $|D_1|$ and $r_{\rm BH}$ have the same growth rate. This feature provides another evidence that the BH motion is a result of the physical interaction with the $m = 1$ disk deformation, but not due to gauge effects.

We point out that, as a result of the interaction of the $m = 1$ deformed disk with the BH, the latter acquires significant orbital angular momentum from the disk. Fig. 5.3 illustrates how angular momentum of the disk ($J_{\rm D}$), BH ($J_{\rm BH}$)[1] and BH+disk system ($J_{\rm BH} + J_{\rm D}$) changes with

[1]We calculate the total angular momentum of the disk using expression $J_D = \int d^3x\sqrt{-g}T^t_\varphi$ [150], while the orbital angular momentum of the BH is calculated using a simple Newtonian estimate: using the BH speed $r\dot{\varphi}$ and its distance from the origin r, we get $J_{BH} \simeq M_{\rm BH} r^2\dot{\varphi}$.

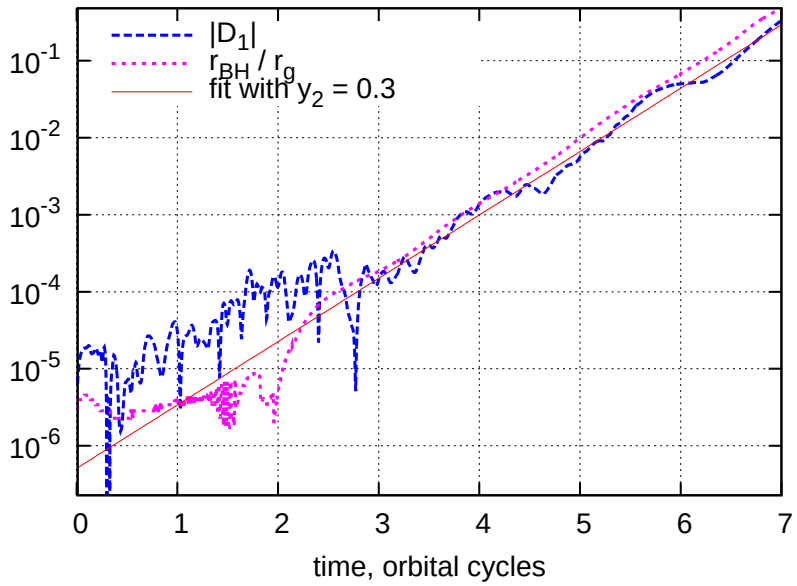

Figure 5.2: Time evolution of the amplitude $|D_1|$ of the non-axisymmetric $m = 1$ mode in the disk and the length of the BH position vector r_{BH}/r_g. The growth of these quantities is correlated, i.e. they develop at the same time and with the same rate.

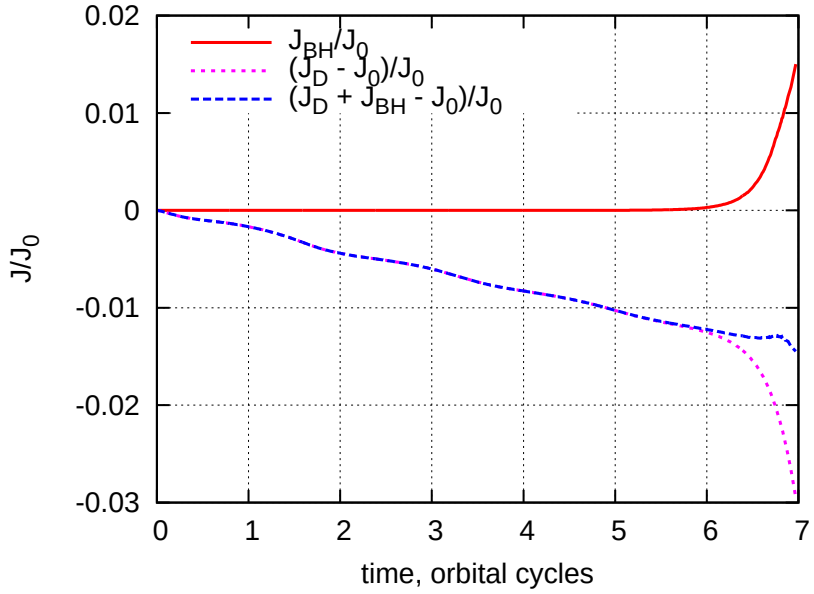

Figure 5.3: Illustration of the angular momentum transfer from the disk to the BH. The solid (red) line shows the orbital angular momentum of the BH J_{BH}, the dotted (magenta) line shows the decrease in the angular momentum of the disk $J_D - J_0$, and the dashed (blue) line shows the total decrease of the angular momentum of disk+BH $(J_D + J_{BH}) - J_0$. All quantities are divided by the initial value of angular momentum of the disk J_0. The noticeable angular momentum transfer can only be seen in the last orbital period, when the $m = 1$ distortion reaches significant amplitude. The gradual decrease in total angular momentum is due to the mass loss at the interpolation boundaries. This is a numerical artifact which converges away with resolution.

time with respect to initial disk angular momentum (J_0). The total angular momentum of the disk+BH system decreases by $\sim$ 1.5% ($\sim$ 3%/$\sim$ 0.7%) in $\sim$ 7 orbital periods due to numerical errors such as interpolation at the block boundaries and evaporation to the artificial atmosphere in the case of medium (coarse/high) resolution simulations. As a result of angular momentum transfer, $J_{\rm D}/J_0$ additionally decreases by $\sim$ 1.5%, which is completely compensated by the $\sim$ 1.5% increase of $J_{\rm BH}/J_0$.

Unfortunately, the continued outspiraling motion of the BH ultimately leads to the intersection of the apparent horizon with the excision boundary. At this point, the inner excision boundary conditions become ill-posed, and we have to terminate our simulations.

Similarly to the findings of Montero et al [43], we did not observe runaway instability in all three models. We also do not expect this instability to occur at a later time. In the most likely scenario of the subsequent evolution, the development of non-axisymmetric instabilities will redistribute disk angular momentum and lead to a profile of specific angular momentum that increases outwards [32, 137]. Such angular momentum profile was shown to strongly disfavor runaway instability [35]. Moreover, the damping of radial disk oscillations in models A and B reduces and eventually completely terminates mass transfer from the disk to the BH, preventing onset of runaway instability.

To determine how much our results depend on numerical resolution, we have performed simulations of model A for three different resolutions with grid cell size scaling as $1 : 1.5 : 1.5^2$. We refer to these resolutions as coarse, medium and fine resolutions hereafter. The curvilinear geometry of the blocks was chosen to be the same for all of the three resolutions. We list the parameters of the resulting coarse, medium and fine (denoted as AFc, AF and AFf, respectively) grid models in Table 4.2.

Figure 5.4a shows the L_1- and L_∞-norms of Hamiltonian constraint violation for the coarse, medium and fine resolution simulations. This plot shows that there are two distinct regimes in the evolution of the constraints: initial exponential decrease and subsequent steady plateau. The former is due to the constraint damping mechanism of our evolution scheme, which saturates at the plateau when the constraints reach the level of discretization errors. Since the discretization error depends on grid cell size, the value of the plateau decreases with increasing resolution. In

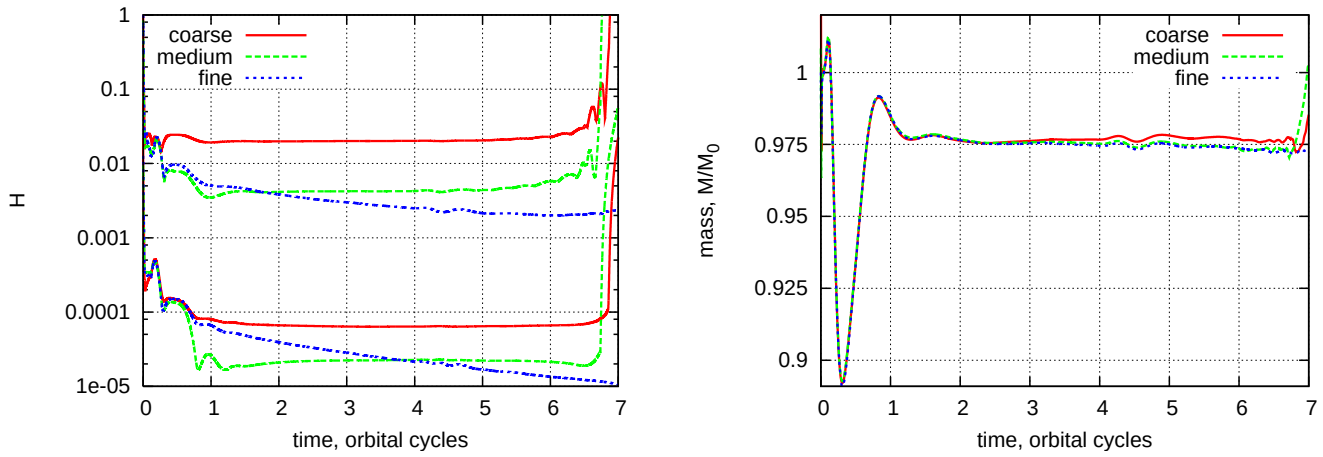

Figure 5.4: Damping of the constraints and its influence on the black hole mass for simulations using the coarse, medium and fine resolution grid. (a) L_∞- and L_1-norms of the Hamiltonian constraints. For the cases of coarse and medium resolutions, the plot shows that the constraints are reduced down to the discretization error level during the first orbital period. See further discussion in the main text. (b) BH mass, measured from the area of apparent horizon, normalized by its initial value. After the initial transitional oscillatory phase, the BH mass settles down to $\sim 97.5\%$ of its initial value. The oscillation in the first orbital period is caused by the constraint violations due to blending procedure in the construction of our initial data (see Section 4.1).

the case with the highest resolution, the "plateau regime" is not reached during the time span of the simulation. Fig. 5.4a also shows that there is a small region of a rapid growth of the constraints at the very end of the simulations. This increase is caused by the approach of the BH apparent horizon too close to the inner excision boundary as a result of the interaction of the BH with the $m = 1$ deformation of the disk described above.

Figure 5.4b shows the time evolution of the BH mass [2]. Because the constraint violations due to the metric blending are introduced at the continuum limit, the BH mass shows an unphysical oscillation that does not converge away with resolution, but which completely damps out in about one orbital period. The BH mass then stabilizes at $97.5 \pm 0.5\%$ of its initial value and remains near this value until the end of the simulation.

We now proceed to the analysis of the induced axisymmetric disk oscillations. Fig. 5.5 shows the time evolution of the maximum disk density ρ_{max} (solid line) and the radial position of the disk center r_c (dashed line), normalized to their values at $t = 0$. As can be seen from this plot,

[2] We measure irreducible BH mass $M_{\rm BH}$ using the area of apparent horizon [151].

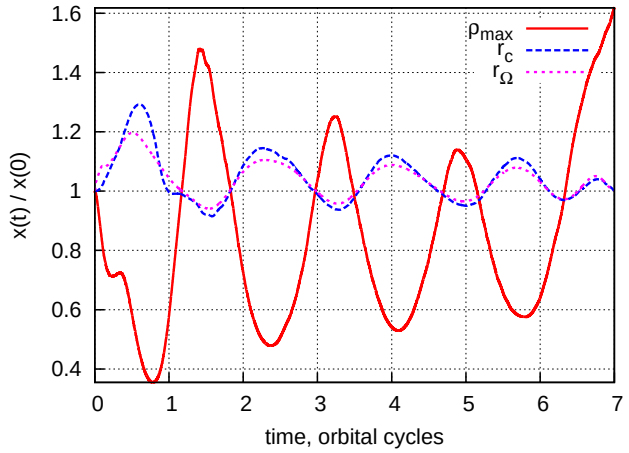

Figure 5.5: Time evolution of the maximum rest-mass density, the location of a rest-mass density maximum $r(\rho_{max})$, and $r(\Omega_K = \Omega_{fl})$, a point where the radial profiles of Keplerian angular velocity $\Omega_K(r)$ and fluid angular velocity $\Omega_{fl}(r)$ on the x axis at $t = 0$ intersect with each other.

the evolution of both ρ_{max} and r_c is dominated a single mode of oscillation. The disk expands while moving away from the BH, and contracts while moving towards the BH. This can be seen on four panels of Fig. 5.6, which shows meridional cuts of the disk in the xz-plane in different phases of the oscillation.

The radial oscillation of the disk has frequency of $\sim$ 164 Hz, a value that is slightly smaller than the epicyclic frequency $\kappa = 201$ Hz at $r = r_c$ for a Schwarzschild BH of the same mass [3]. Rezzolla et al. [153] studied relativistic axisymmetric oscillations of accretion disks in Cowling approximation using disk models that have the same Γ ($= 4/3$) and (constant) specific angular momentum profile as the ones studied here. They found that the disks with $r_c = 3.860\ r_g$ have the radial oscillation frequency of $\simeq$ 261 Hz ($= 0.02017$ for their c2 model in normalized units [153]), which is higher than the $\sim$ 164 Hz frequency that we obtain in our case. Part of this difference stems from the difference in the disk models: while model of [153] has $r_c = 3.860\ r_g$, our disk model A has $r_c = 6.51\ r_g$ (cf. Table 4.1). Rezzolla et al. [153] has found that the oscillation frequency f depends on the disk extent L in a particular way. Namely, f decreases with increasing L, and in the limit of very thin disks ($L \to 0$), f approaches the local value of the epicyclic frequency κ (see Fig. 4 of [153]). If we assume this dependence $f(L)$ to hold for any

[3]The relativistic epicyclic frequency for the Schwarzschild metric is given by $\kappa = \frac{1}{2\pi}\sqrt{\frac{GM}{r^3}\left(1 - \frac{3r_g}{r}\right)}$ [152].

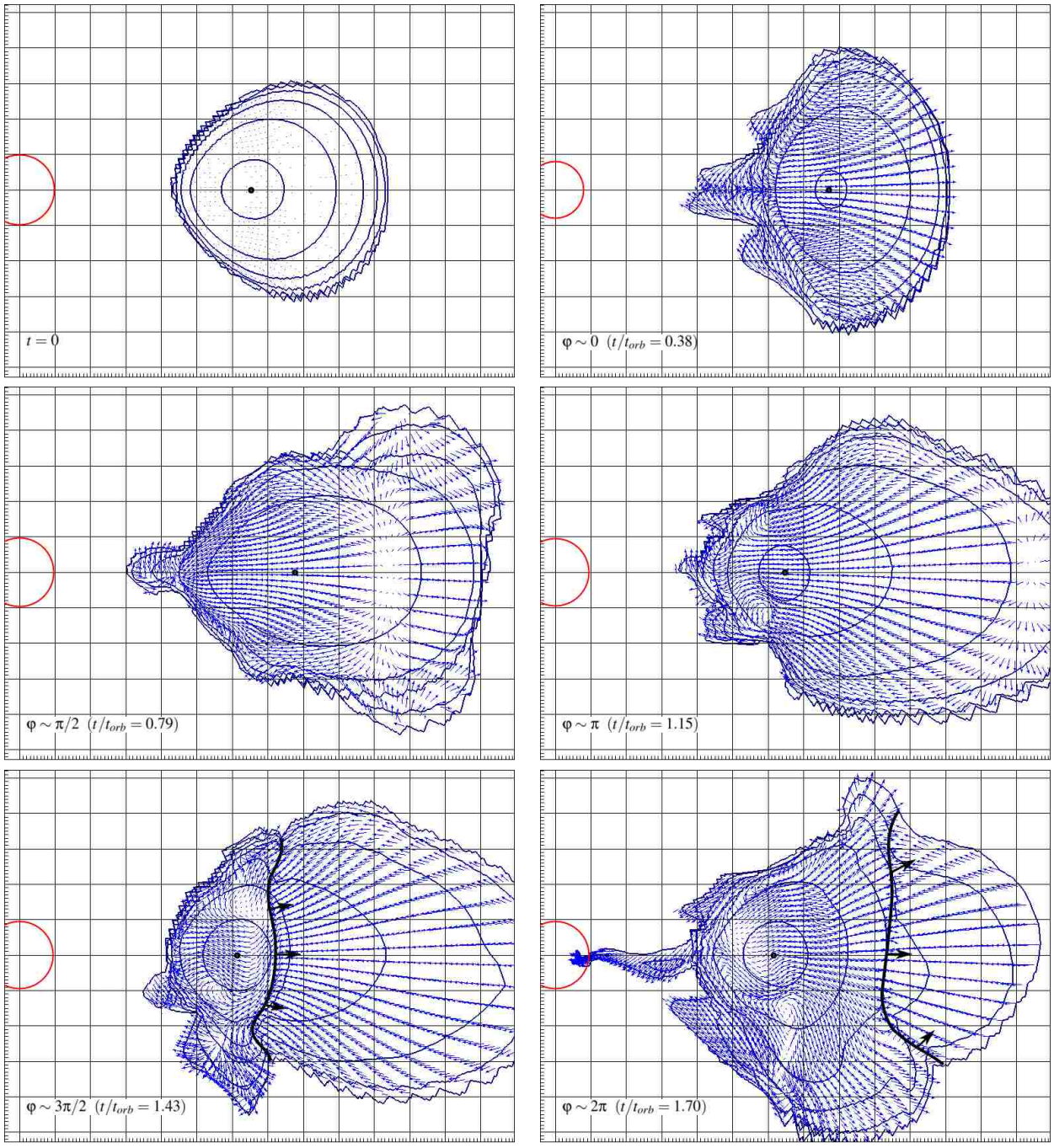

Figure 5.6: Meridional cuts of the disk and the BH horizon in the xz-plane at several consecutive phases $\varphi \sim 0 - 2\pi$ of the radial oscillation. Each frame shows six density contours, equally spaced in logarithmic scale between the initial maximum density $\rho_{\max}(0)$ and 10^{-6} times that value. Also shown is the velocity field in the meridional plane and the location of the density maximum. The bottom two frames show the position of the shock that is propagating outwards. The last frame shows a brief episode of accretion.

r_c, we can obtain the value of radial oscillation frequency for a disk with the same L and r_c as our model. This frequency turns out to be ~ 168 Hz, which is very close to $f = 164$ Hz that we obtain in our simulations. This result might indicate that for the disks that are similar to the ones considered here, the disk self-gravity does not significantly affect the frequencies of the radial oscillations. Note that in the case of NSs, the frequency of the fundamental quasi-radial modes was found to differ by a factor of ~ 2 between Cowling and full GR simulations [93], perhaps implying that the self-gravity plays more important role in the case of NSs. However, since it is unclear whether such dependence of f on L holds exactly for other values of r_c, this result should be taken with caution. We will revisit this issue in a future publication.

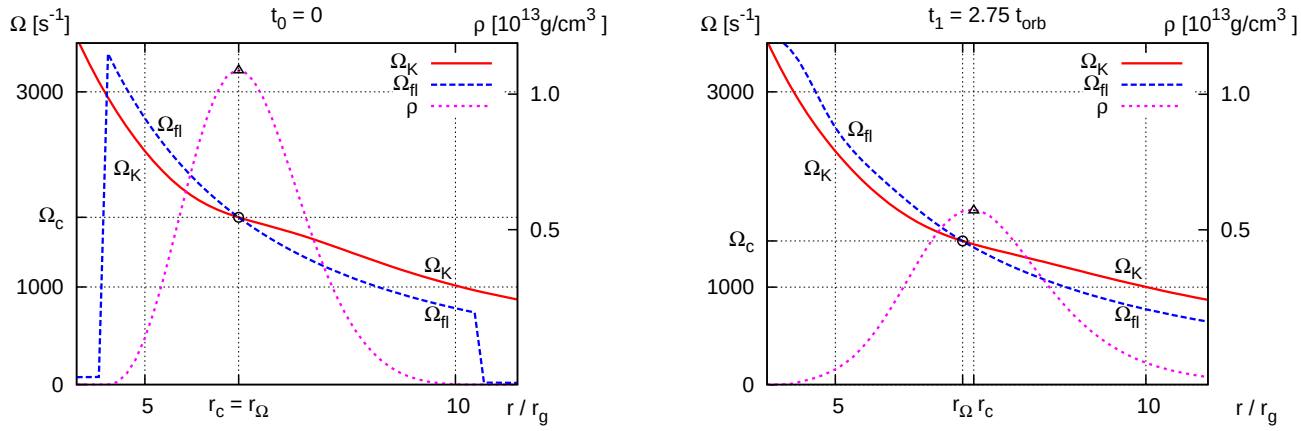

Figure 5.7: This plot illustrates the mechanism of disk oscillations by showing a combined radial profiles of $\Omega_K(r)$, $\Omega_{fl}(r)$ and the rest mass density $\rho(r)$ at two moments of time, $t_0 = 0$ and $t_1 = 2.75 t_{orb}$. A small black circle marks the location of the intersection point $\Omega_K = \Omega_{fl}$, and the small black triangle marks the density maximum. In equilibrium, the location of the density maximum has to coincide with the location of the intersection point $\Omega_K = \Omega_{fl}$. See the main text for further discussion of the mechanism of radial oscillations.

To understand the mechanism of the oscillations, we consider the behavior of radial profiles of the fluid angular velocity $\Omega_{fl}(r)$ and Keplerian velocity $\Omega_K(r)$ [4]. Left (right) panel of Fig. 5.7 shows the profiles $\Omega_K(r)$, $\Omega_{fl}(r)$ and the density ρ_{max} at the initial time t_0 (at a later time $t_1 = 2.75 t_{orb}$). As can be seen in the left panel of this figure, functions $\Omega_{fl}(r)$ and $\Omega_K(r)$ intersect at

[4]The Keplerian velocity is defined in a usual way [150] as that of a test particle on a circular orbit of radius r in the reference frame of remote observers: $\Omega_K(r) = u^\varphi / u^t$ (where u^φ and u^t are the nonzero components of 4-velocity of the particle). We point out that although this definition of $\Omega_K(r)$ is only valid in assumption of axisymmetry and stationarity of the spacetime, we can consider it as a reasonable approximation for the first six orbital periods of the disk, before the non-axisymmetric instability becomes significant.

the location of density maximum r_c, as indeed should be the case for equilibrium tori. At a later time, when the equilibrium is violated, the intersection point r_Ω, where $\Omega_{fl}(r_\Omega) = \Omega_K(r_\Omega)$, does not coincide with r_c. This can be seen in the right panel of Fig. 5.7.

Figure 5.5 (dotted line) shows time evolution of r_Ω. The initial perturbation of gravitational field modifies the radial profile of Ω_K, resulting in an outward displacement of r_Ω and violation of the disk equilibrium. This triggers the motion of the disk, so that r_c follows r_Ω. It eventually reaches r_Ω but because of the obtained outward radial momentum r_c overshoots r_Ω, resulting in the deceleration and inward motion of r_c. The location of r_Ω is mainly determined by r_c, and the inward motion of r_c leads to the inward motion of r_Ω. r_c again overshoots r_Ω, and this process repeats in oscillatory manner, reflecting the radial oscillations of the disk. Such oscillatory motion, when r_c follows r_Ω, cannot be a gauge effect. This oscillation also cannot be driven by the pressure gradients, because they are zero at r_c. We note that the radial profile of Ω_{fl} does not change noticeably with time, while that of the density oscillates significantly. This implies that the conservation of total angular momentum can only be achieved by compensating oscillations in the metric. Therefore, the dynamical spacetime plays significant role in this type of oscillations.

The oscillating disk emits gravitational waves at the frequency f_0. Their amplitude can be estimated from the quadrupole formula [154], which gives $A_{20}^{E2} \simeq 210$ cm. The average gravitational luminosity due to the axisymmetric wave emission,

$$L_{GW} = \frac{c^3}{32\pi G}\left(\frac{dA_{20}^{E2}}{dt}\right)^2 \simeq 2.0 \cdot 10^{47}\ \mathrm{erg}/s,$$

produces overall energy loss during the evolution to the gravitational radiation $\Delta E_{GW} \simeq 5 \cdot 10^{45}$erg. This is five orders of magnitude smaller than the average kinetic energy of radial disk motion $T \simeq 1.37 \cdot 10^{50}$erg, and can not be responsible for the damping of the oscillations.

Therefore, the main process responsible for the damping of oscillations is the shock heating: shock waves convert the kinetic energy of the oscillations into the thermal one. At the end of the contraction phase of the disk, the high-density inner part of the disk bounces back earlier than the lower-density outer part. The collision of the former with the still-infalling lower-density

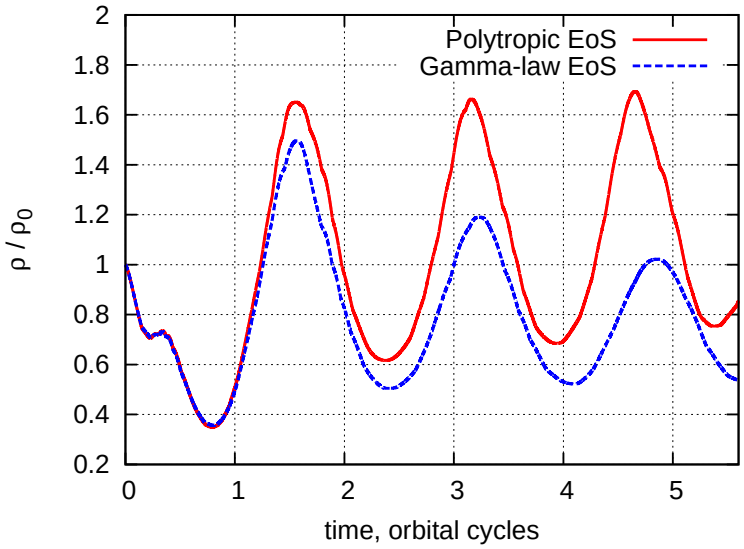

Figure 5.8: Time evolution of the maximum density of the disk evolved with polytropic and Γ-law EOSs. In the case of polytropic EOS, disk oscillations show little damping, while in the case of Γ-law EOS, oscillation amplitude decreases by a factor of ~ 2 during ~ 4 orbital periods due to shock heating.

outer material leads to formation of an outward-propagating shock wave (see two bottom panels on Fig. 5.6). The shock accelerates during propagation and reaches relativistic velocities of $\sim 0.3c$ in the rarefied outer disk shells. In order to quantify the amount of the shock dissipation, we evolve this model with isentropic polytropic EOS with the same $\Gamma = 4/3$ (in addition to the evolution with the non-isentropic Γ-law EOS), which does not allow entropy changes and thus shock heating. Fig. 5.8 shows time evolution of the maximum density for models evolved with polytropic and Γ-law EOSs. In former case, the oscillations exhibit little damping, while in the latter case, amplitude of $\rho_{\rm max}$ decreases by a factor of ~ 2 in ~ 7 orbital periods. Note that dissipation of oscillation kinetic energy into heat has been found to operate in many astrophysical scenarios: damping of NS oscillations in a migration from an unstable to a stable branch [155, 156], in phase-transition-induced collapse of NSs [157], damping of ring-down oscillations of nascent proto-NSs in core-collapse supernovae and accretion-induced collapse of white-dwarfs (e.g., [158]).

Chapter 6. Non-axisymmetric Instabilities

In this chapter, we discuss non-axisymmetric instabilities in the disks. First, we test our method by reproducing results obtained by Kojima [28] for thick tori with negligible mass on a Schwarzschild background. In the next two sections we analyze the non-axisymmetric instabilities in our models first on fixed background, and then with fully dynamical general relativistic treatment.

In various astrophysical scenarios, the disk might be formed with different non-axisymmetric structures, leading to preferential excitation of unstable non-axisymmetric modes. The subsequent nonlinear evolution of the disk is determined not only by the growth rates of the modes, but also by the sequence in which the modes were excited. In other words, depending on the azimuthal number m of the initial perturbation, the disk may take different evolution paths and arrive into different final states. In order to account for these possible scenarios, in our work we evolve initial disks with added small non-axisymmetric perturbations.

We expect [27, 29, 82] our thick disk models A and B to be dominated by non-axisymmetric unstable modes with azimuthal numbers $m = 1$ and $m = 2$, while for more slender model C instabilities with $m = 3$ and $m = 4$ should also play an important role. In our simulations without initial perturbations, these modes are triggered by numerical errors and start to grow at random moment in time. In order to explore evolutionary scenario in which a particular mode is excited initially, we add small density perturbation of the form $\tilde{\rho} = \rho[1 + A \cos m(\varphi - \varphi_0)]$ to our initial disk models. We use a perturbation amplitude $A = 0.001$, which we have found to be both large enough to trigger the instability, and sufficiently small to remain in the linear regime. The amount of constraint violations due to these artificial perturbations, which is quickly suppressed by our constraint damping scheme is too small to significantly affect the subsequent evolution of the disk.

For each initial disk model A, B and C we have completed a sequence of evolutions both

in Cowling and in full GR treatment. As explained in the end of Section 4.3, corresponding simulations are referred to by two- or three-letter notation (such as AC, AC1, AC2, AF, etc.), in which the first letter denotes the initial disk model (A, B or C), the second letter is either 'C' for Cowling or 'F' for full GR treatment, and the third one is the azimuthal number m of the initial perturbation (absent if evolved without initial perturbation).

6.1 Comparison with Previous Work

Below we present the growth rates of PP instability in evolutions of equilibrium tori in Cowling approximation and compare them with the results obtained by Kojima [28], who studied PP instability in thick disks around Schwarzschild BHs using a linear perturbative approach. Kojima analyzed tori with constant distribution of specific angular momentum, constructed in a relativistic framework using the Abramowicz-Sikora-Jaroszynski (AJS) prescription [95]. Kojima calculated the $m = 1$ mode growth parameter y_2 for several sequences of disk models with different values of specific angular momentum ℓ ($= 3.8,\ 4.0,\ 4.2$) . In particular, [28] found that, due to relativistic redshift effects, y_2 for GR models is generally smaller than in Newtonian case [27].

We have constructed a sequence of AJS tori of varying radial extent with the same physical parameters as in [28]. All these models have polytropic index Γ of $4/3$ and specific angular momentum ℓ of 4.0. The mass of the black hole is set to $M_{\rm BH} = 1$. The models in this sequence are labelled as K1-K6, and their parameters are listed in Table 6.1. To excite the $m = 1$ mode, we add a small non-axisymmetric perturbation as described above, and evolve the disk in Cowling approximation, using a curvilinear grid (as described in Section 4.3), adapted to each of the models. Parameters of the curvilinear grids for each model are listed in Table 4.2. We then measure the growth rate y_2 as described in Section 4.4 above and compare it with the results of Kojima.

Figure 6.1 shows the values of y_2 as a function of the disk radial extent for our models and for those of Kojima. As we can see, y_2 for our models are within estimated error bars from the values, calculated by Kojima in [28], as should be the case.

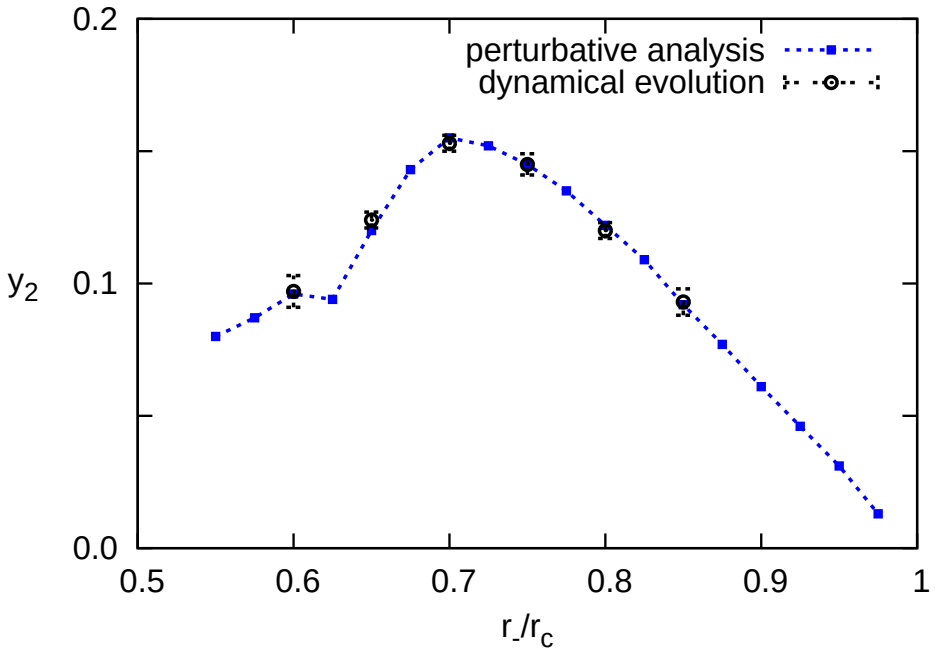

Figure 6.1: Comparison of the $m = 1$ PP mode growth rates y_2 obtained by Kojima [28] in linear perturbative approach with the values measured from the evolutions of the same initial data models in Cowling approximation. The abscissa represents the ratio of the inner radius of the disk r_- to the radius of the maximum disk density r_c. The error bars of the measured growth rates originate from the uncertainty in determining the time span of a clear exponential growth of the mode.

Table 6.1: Physical parameters of the initial disk models, used for comparison with calculations by Kojima [28]. Here, r_c/r_g is the location of the density maximum in units of the BH gravitational radius r_g, r_- (r_+) is the inner (outer) radius of the torus, and ρ_{max} is the maximum density. For all models, the mass of the BH is $\mathcal{M}_\odot$, specific angular momentum has constant value $\ell = 4.0$, and polytropic constant $K = 0.06$ (the latter two quantities are given in the normalized system of units, in which $G = c = \mathcal{M}_\odot = 1$).

Model	r_c/r_g	r_-/r_c	r_+/r_-	$\rho_{\max}$
K1	5.236	0.60	3.952	$1.715 \cdot 10^{-4}$
K2	5.236	0.65	2.956	$5.321 \cdot 10^{-5}$
K3	5.236	0.70	2.351	$1.472 \cdot 10^{-5}$
K4	5.236	0.75	1.939	$3.522 \cdot 10^{-6}$
K5	5.236	0.80	1.640	$5.809 \cdot 10^{-7}$
K6	5.236	0.85	1.419	$8.682 \cdot 10^{-8}$

Table 6.2: Parameters of the $m = 1$ PP instability, measured for the dynamical evolutions of Kojima disk models K1-K6. y_1 and y_2 are the pattern speed and growth rate parameters, Ω_p is the mode pattern speed, and r_{cr} is the mode corotation radius.

Model	y_1	y_2	Ω_p/Ω_c	r_{cr}/r_c	Type
K1	-0.174	0.097(6)	0.826	1.136	PP
K2	-0.147	0.124(3)	0.853	1.112	PP
K3	-0.113	0.153(3)	0.887	1.083	PP
K4	-0.084	0.145(4)	0.916	1.041	PP
K5	-0.048	0.120(3)	0.952	1.060	PP
K6	-0.011	0.093(5)	0.989	1.007	PP

6.2 Fixed Background

In this section, we analyze non-axisymmetric instabilities which develop when our initial disk models are evolved on fixed spacetime background (so-called Cowling approximation). We find that all of our models develop Papaloizou-Pringle (PP) instability. More specifically, for moderately slender models A and B the fastest growing mode is $m = 2$, while for more slender model C it is $m = 3$. Below, we first describe instabilities in models A and B, after which we focus on model C. As mentioned above, we evolve our models with and without artificial density perturbations. For models A and B, we add $m = 1, 2$ and for model C we add $m = 1, 2, 3$ perturbations. Notice that all simulations contain small spurious $m = 4$ perturbation which is a numerical artifact of interpolation at the boundaries between four blocks near equatorial plane. The evolutions without artificial perturbation are therefore similar to the ones in which an $m = 4$ density perturbation is added.

To analyze the non-axisymmetric modes, we adopt an approach from Woodward et al [82]. Namely, we expand the disk density in equatorial plane in Fourier series, as explained in Section 4.4 above. Then we construct the following four diagrams:

(a) $D_m - t$ diagram: logarithm of the normalized mode amplitude D_m as a function of time at some radial location close to the disk density maximum r_c. The slope of this curve yields the growth rate y_2.

(b) $D_m - r$ diagram: a radial profile of the normalized mode amplitude D_m.

(c) $\varphi_m - t$ diagram: a phase angle of the non-axisymmetric mode m as a function of time at a specified radius. The slope of this function determines the mode pattern speed and parameter y_1, related to it.

(d) $\varphi_m - r$ diagram: mode phase angle as a function of radius. This diagram provides very convenient way to identify the type of the mode.

Such diagrams allow to identify types of non-axisymmetric modes [82] and extract their quantitative characteristics such as mode growth rate y_2 and pattern speed parameter y_1. These quantities for our evolutions are summarized in Table 6.3.

We found that instabilities which develop during evolutions of models A and B are very similar. Therefore we present the properties of these instabilities on example of model A.

Figure 6.2 shows the four mode diagrams for the case of model AC1, which represents time evolution of initial disk model A in Cowling approximation with an added $m = 1$ non-axisymmetric density perturbation. Panel (a) shows the $D_m - t$ diagram for the first six non-axisymmetric modes with $m = 1, 2, \ldots, 6$. Three lowest-m modes exhibit clear exponential growth, with $m = 1$ being the dominant mode throughout the time span of the simulation (first 6.5 orbital periods). This is the case because an $m = 1$ perturbation is artificially added from the beginning and has more time to grow and to remain the dominant mode. The mode $m = 2$ has higher growth rate, but appears subdominant, since it is triggered later than the $m = 1$ mode and has less time to develop. It may eventually overshoot the $m = 1$ mode at a later time, when both modes reach nonlinear regime. Notice that the relatively high values of the $m = 4$ mode amplitude are due to the effect of interpolation errors on four interpatch boundaries of the grid near the equatorial plane.

Panels (b) and (d) of Fig. 6.2 demonstrate the radial structure of the $m = 1$ mode at $t = 4\ t_{orb}$, when it is sufficiently developed. The $D_m - r$ diagram on Fig. 6.2b represents the radial profile of the amplitude of the mode. This amplitude is highest near the edges of the disk, it does not have nodes (does not become zero), and it reaches its minimum near the radius of corotation. Previous works on PP instability in Newtonian gravity [24, 29] suggest such radial behavior for

Table 6.3: Quantitative characteristics and types of the non-axisymmetric modes for the simulations studied in Section 6.

Cowling							Full GR						
Model	m	type	y_1	y_2	Ω_p/Ω_0	r_{cr}/r_c	Model	m	type	y_1	y_2	Ω_p/Ω_0	r_{cr}/r_c
AC	2	PP	-0.10(5)	0.21(1)	0.89(2)	1.07(1)	AF	1	PP	-0.17(5)	0.300(8)	0.83(5)	1.12(4)
AC1	1	PP	-0.08(4)	0.17(1)	0.93(2)	1.04(1)	AF1	1	PP	-0.18(5)	0.294(8)	0.82(5)	1.11(4)
AC2							AF2	1	PP	-0.17(3)	0.30(1)	0.83(3)	1.12(3)
	2	PP	-0.09(5)	0.22(1)	0.95(2)	1.03(1)		2	I	-0.6(1)	0.17(3)	0.68(5)	1.26(6)
BC	1	PP	-0.04(5)	0.16(1)	0.96(5)	1.03(3)	BF	1	PP	-0.16(5)	0.28(3)	0.84(5)	1.12(4)
	2	PP	-0.12(6)	0.18(1)	0.94(3)	1.04(2)							
BC1	1	PP	-0.06(5)	0.16(1)	0.94(5)	1.04(3)	BF1	1	PP	-0.12(5)	0.270(8)	0.88(5)	1.08(4)
BC2	1	PP	-0.04(5)	0.17(1)	0.96(5)	1.03(3)	BF2	1	PP	-0.13(5)	0.29(2)	0.87(5)	1.09(4)
	2	PP	-0.08(6)	0.17(1)	0.96(3)	1.03(2)		2	I	-0.5(1)	0.11(2)	0.75(5)	1.19(5)
CC	3	PP	-0.06(5)	0.21(2)	0.98(2)	1.01(1)	CF						
	4	PP	-0.04(5)	0.14(1)	0.99(2)	1.00(1)		4	I	-0.84(8)	0.16(1)	0.79(2)	1.14(2)
CC1	3	PP	-0.04(5)	0.24(1)	0.99(2)	1.00(1)	CF1	1	PP*?	??	??	–	–
	4	PP	-0.04(5)	0.16(2)	0.99(2)	1.00(1)		4	I	-0.84(8)	0.15(1)	0.79(2)	1.14(2)
CC2	2	PP	-0.04(5)	0.20(1)	0.99(2)	1.00(1)	CF2	2	I	-0.6(1)	0.279(7)	0.66(5)	1.26(5)
	3	PP	-0.06(5)	0.22(1)	0.98(2)	1.01(1)		4	I	-0.8(2)	0.16(1)	0.80(5)	1.14(4)
CC3	3	PP	-0.07(5)	0.23(1)	0.98(2)	1.01(1)	CF3	3	I	-0.7(1)	0.318(8)	0.76(3)	1.17(3)
	4	PP	-0.04(5)	0.15(2)	0.99(2)	1.00(1)		4	I	-0.80(8)	0.16(2)	0.80(2)	1.14(2)

*For the simulation CF1, it was not possible to accurately determine the growth rate and pattern speed of the $m = 1$ mode. We classified this mode as a PP-type due to the character of its $\varphi_m - r$ and $D_m - r$ diagrams, which are typical for the PP-modes.

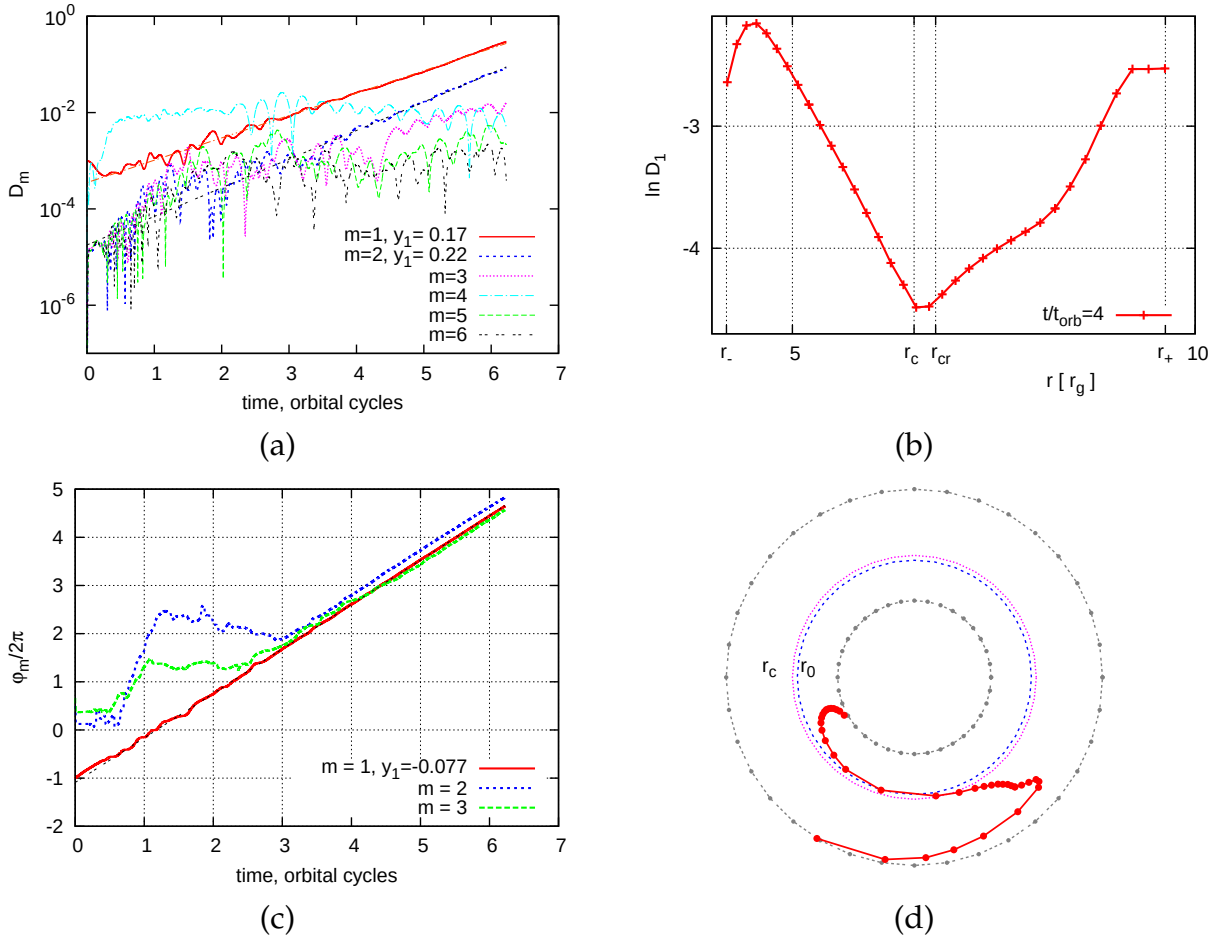

Figure 6.2: The behavior of the dominant non-axisymmetric modes and the radial character of the $m = 1$ (0,0) PP-mode in the simulation AC1: (a) $D_m - t$ diagram shows the time evolution of the mode amplitudes D_m for $m = 1 - 6$; (b) $D_m - r$ diagram shows the radial character of the $m = 1$ mode amplitude (in logarithmic scale); (c) $\varphi_m - t$ diagram shows the time evolution of the Fourier angle φ_m, which allows to determine a pattern speed and a corotation radius for each mode; (d) $\varphi_m - r$ diagram shows the dependence of the mode Fourier angle from the radius r in equatorial plane at $t/t_{orb} \simeq 4$. The $D_m - r$ and $\varphi_m - r$ diagrams on panels (b) and (d) also show the locations of the mode corotation radius.

the principal PP mode, or a mode of (0,0)-type in Blaes and Hawley classification [139]. The $\varphi_m - r$ diagram on Fig. 6.2d has a specific S-shaped structure, which is also a well-known feature of the PP instability, discovered in previous Newtonian works [29, 82].

Finally, panel (c) of Fig. 6.2 shows the $\varphi_m - t$ diagram for the $m = 1 - 3$ modes. It shows that while all modes initially have arbitrary phases and pattern speeds, they eventually settle to the pattern speed of the dominant $m = 1$ mode possibly due to nonlinear interaction between the modes. The pattern speed of the $m = 1$ mode is slightly below the speed of the disk at

r_c, which means that the mode corotation radius r_{cr} lies just outside r_c. The close proximity of the mode corotation radius to the radius of the disk density maximum is also typical for PP non-axisymmetric instabilities, as discovered in previous Newtonian works [24,26,82]. All these features allow us to conclude that the observed $m = 1$ mode is indeed the PP instability.

Figure 6.3 shows the set of four diagrams for simulation AC2, in which an $m = 2$ density perturbation is added initially. Panel (a) represents $D_m - t$ diagram for the modes with $m = 1 - 6$. In this case, only the mode with $m = 2$ exhibits pronounced exponential growth. The rest of the modes remain either stable or not excited, showing rapid growth only in the very end of the simulation, when the amplitude of $m = 2$ mode reaches nonlinear regime and coupling between the modes becomes important. Panels (b) and (d) of Fig.6.3 show the radial profile and azimuthal shape of the mode. These are again typical for the principal (0,0)-type PP instability with $m = 2$. Fig. 6.3c shows the $\varphi_m - t$ diagram for the $m = 1 - 3$ modes. The dominant $m = 2$ mode rotates uniformly in the same direction as the disk, while other two modes do not exhibit clear rotation pattern until after ~ 4 orbital periods, when they align in phase with the $m = 2$ mode. The pattern speed of the dominant mode inferred from this plot corresponds to the corotation radius just outside of r_c. Similarly to the simulation AC1 above, all these features are typical of the PP instability, studied in previous works in Newtonian approximation.

While unstable modes in model B are very similar to those of model A, in model C higher order PP modes become dominant. This is expected [27] since model C is more slender than models A and B. Indeed we observe that the most unstable mode for the model C is the $m = 3$ PP mode, while $m = 2$ and $m = 4$ have comparable but smaller growth rates. The four diagrams for $m = 3, 4$ modes are not qualitatively different from those for the $m = 1, 2$ modes in simulations AC1 and AC2 above. They also exhibit all the features typical of the PP instability described above.

We can therefore conclude that the PP instability with various values of azimuthal number m is observed in all of our disk models. For reader's reference, the parameters of unstable modes calculated for all of our simulations are summarized in Table 6.3.

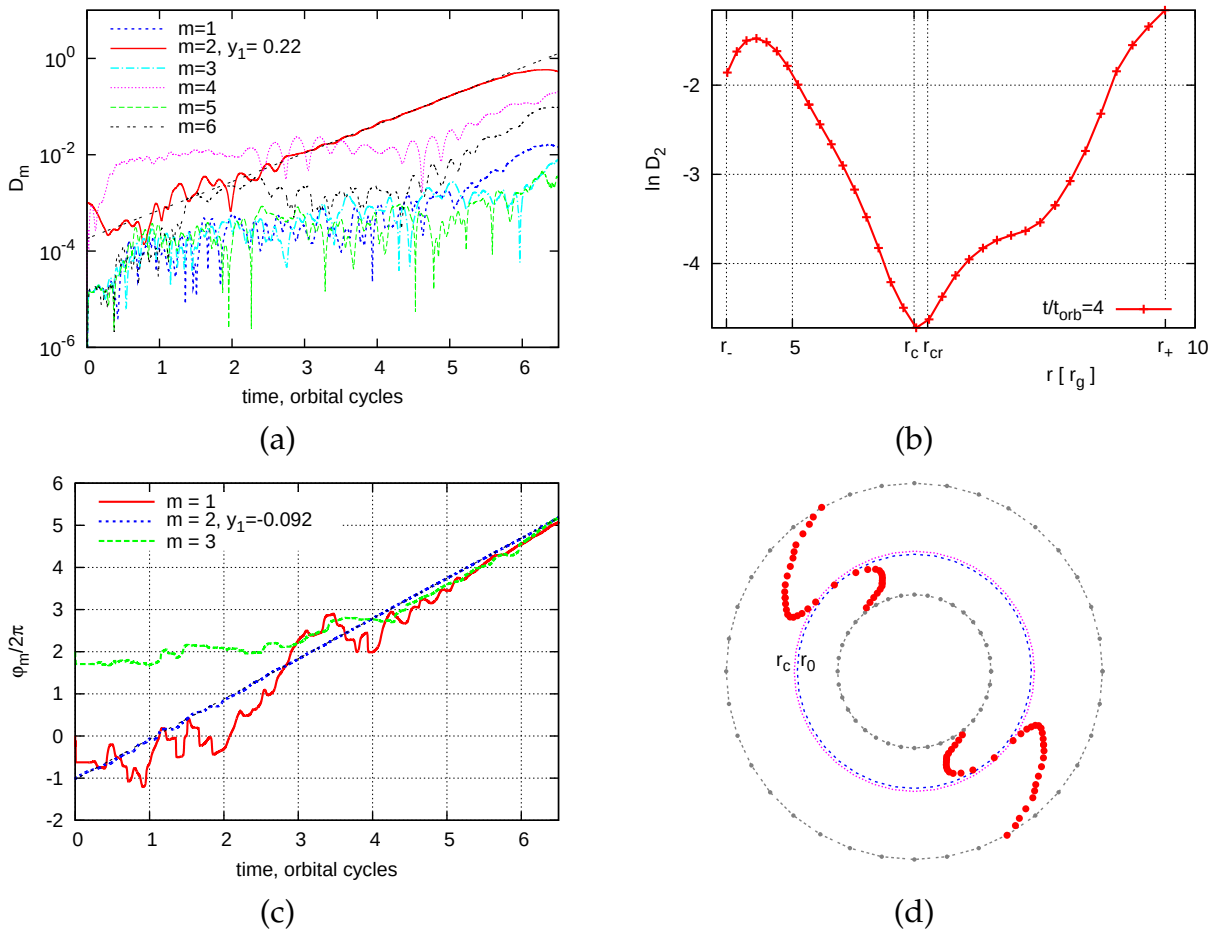

Figure 6.3: The behavior of the dominant non-axisymmetric modes and the radial character of the $m = 2$ (0,0) PP-mode in the simulation AC2 (see captions to Fig. 6.2 for details).

6.3 Dynamical Background

We now turn to the analysis of non-axisymmetric instabilities, which develop when the disks are evolved in a fully dynamical general relativistic framework. We again consider evolutions with and without artificial density perturbation, adding $m = 1, 2$ perturbations for models A and B and $m = 1, 2, 3$ perturbations for model C. While in the Cowling case we observe only instabilities of PP type for all models, in the fully dynamical GR case we observe two distinct types of instabilities, the Papaloizou-Pringle (PP) type and a GR analog of Newtonian so-called intermediate type (I-type) instability [30, 32]. Similarly to the Cowling case, instabilities in the moderately slender models A and B have very similar properties, so it suffices to present the result only for the case of model A. Model C is more slender and therefore favors instabilities with

higher azimuthal numbers than those of models A and B, so we consider this model separately.

For the analysis of non-axisymmetric modes we adopt the same approach as in Section 6.2 above for simulations on a fixed background, with one exception: for evaluating mode growth rates y_2, instead of D_m, we use quantities G_m introduced in Section 4.4 above. This is necessary because the values of the mode amplitudes D_m at a fixed radial location oscillate due to disk oscillations, making it hard to infer accurate growth rates of the modes. We have found that mode growth rate y_2 can be calculated more accurately from a time behavior of G_m, because it is expressed in terms of integrals over the radius and as such it is much less affected by radial oscillations. With this exception, we follow the approach described in Section 6.2 to determine mode types, growth rates and pattern speeds. These quantities for all models are tabulated in Table 6.3 for reference.

In most of the simulations with fully dynamical GR treatment the BH responds to the excitation of the $m = 1$ mode by developing an outspiraling motion, as described earlier in the Chapter 5. Position vector $\bar{r}_{BH}$ of the BH starts to rotate with approximately constant angular velocity Ω_{BH}, while the length of this vector grows exponentially. In order to characterize this motion and study it in the context of the development of non-axisymmetric modes, we plot the time evolution of the BH position vector length r_{BH}/r_g and phase angle φ_{BH} on the $G_m - t$ and $\varphi_m - t$ diagrams respectively. From these plots we can calculate the quantities Ω_{BH}/Ω_0 and $y_2(BH)$ that can be directly compared to those of non-axisymmetric modes. These quantities are also listed in the Table 6.3.

Figure 6.4 shows the time evolution and radial profiles of the amplitudes and Fourier angles of the dominant unstable modes for the simulation AF1, which represents fully dynamical GR evolution of the initial disk model A with an added $m = 1$ density perturbation. The top left panel contains the time evolution of G_m for $m = 1 - 4$ and the normalized coordinate length of the BH position vector r_{BH}/r_g. The diagram shows that the $m = 1$ mode is the dominant one. It also shows that the BH responds to the growth of the $m = 1$ mode and the distance from the BH to the origin grows exponentially at the same rate as the dominant $m = 1$ mode.

Panel (c) of Fig. 6.4 shows the time evolution of the Fourier phase angles φ_m for $m = 1, 2, 3$, measured at a fixed radial coordinate location near the inner edge of the disk r_-. The phase

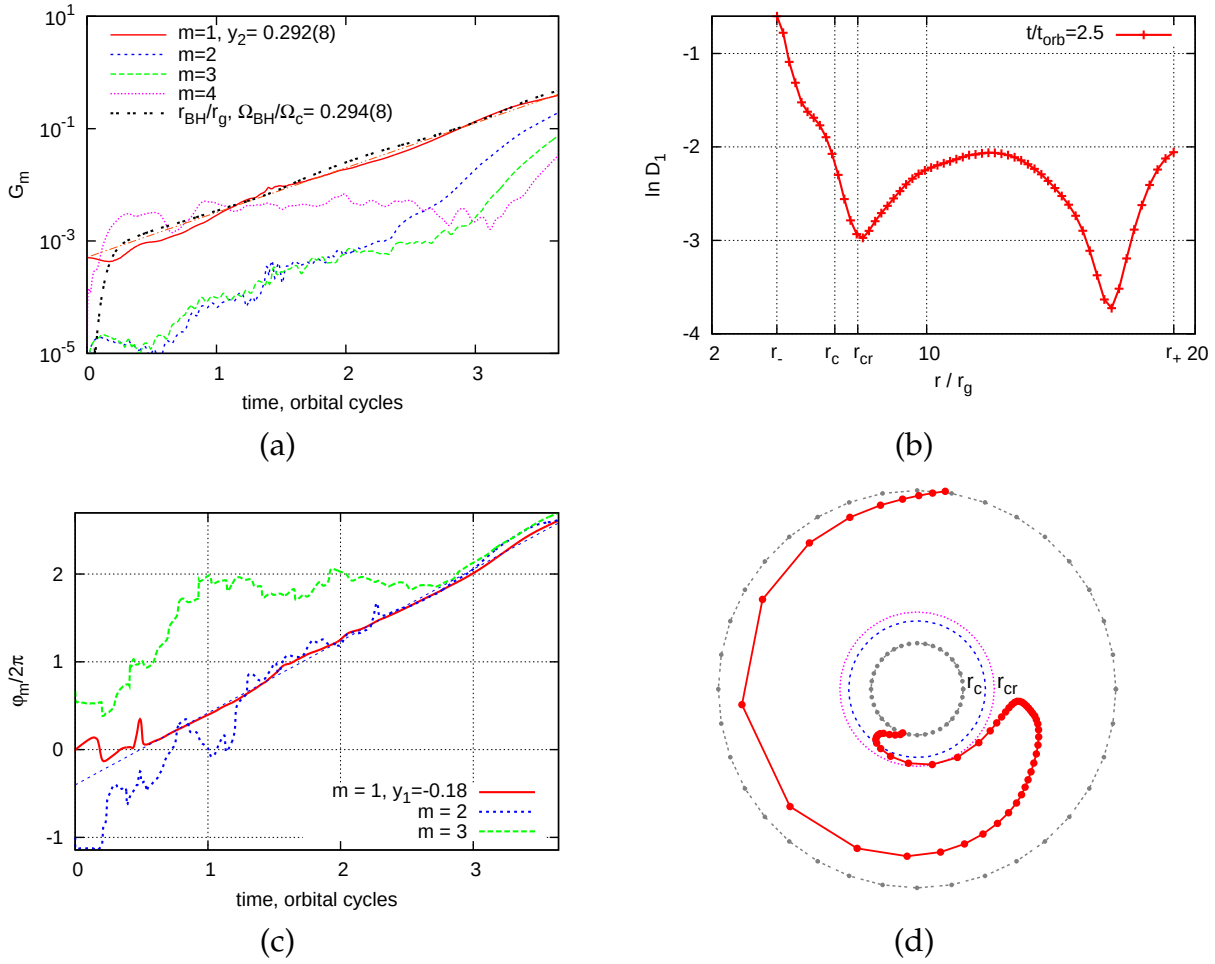

Figure 6.4: The behavior of the dominant non-axisymmetric modes and the radial character of the $m = 1$ (0,0) PP-mode in the simulation AF1 (see captions to Fig. 6.2 for details).

of the dominant $m = 1$ mode after short initial readjustment exhibits almost uniform linear growth. Readjustment of the mode happens because the added artificial perturbation initially does not have the right shape of the mode and needs some time (less than one orbital period) to readjust itself. Similar behavior is observed in the corresponding Cowling simulation, but it is less pronounced (see the $m = 1$ phase angle during the first half orbit on Fig. 6.2c). Phases of the rest of the modes initially do not show uniform linear growth, but as the amplitude of the $m = 1$ mode increases, the higher order modes start to align in phase with the dominant $m = 1$ mode, most likely due to nonlinear modes interaction. Notice that the pattern speed of the $m = 1$ mode calculated from this diagram is lower compared to the Cowling case.

Panels (b) and (d) of Fig. 6.4 show the radial and angular profiles of the dominant $m = 1$

mode at $t = 2.5\ t_{orb}$. The location of r_-, r_+ and r_c shown on the plot refers to the same time. Because the disk undergoes radial oscillations, special care must be taken when calculating the mode corotation radius r_{cr}, which is an important quantity that characterizes non-axisymmetric modes. To find r_{cr}, we solve an equation between the mode pattern speed Ω_p and the disk angular velocity: $\Omega(r_{cr}) = \Omega_p$. The latter changes during the evolution of the disk, so strictly speaking the value of r_{cr} will also depend on time. However, we have found that in all our simulations the change of the profile of Ω in the course of evolution is very small, therefore within the measured accuracy the corotation radius is independent of time. The values of r_{cr}/r_c, calculated in this way for all simulations on a dynamical background are also listed in Table 6.3. For simulation AF1, r_{cr} lies outside of r_c with $r_{cr}/r_c \approx 1.17$. Such a value of r_{cr}/r_c is typical for a PP instability and comparable to the values observed in previous Newtonian studies with a moving central object and a massive self-gravitating disk [82].

Similar to the Cowling case, the radial profiles of D_m and φ_m show structural features that are typical for a PP instability of (0,0)-type in the Blaes and Hawley classification [139]. In particular, the mode amplitude displayed on Fig. 6.4b is higher near the edges of the disk and has a minimum near the corotation radius r_{cr}. The mode amplitude does not vanish anywhere in the disk, which characterizes the mode as having type (0,0). The profile of the Fourier angle of the mode, shown on Fig. 6.4d, has a specific S-shaped structure, that consists of a trailing spiral pattern outside the corotation radius [1], a leading spiral pattern inside the corotation radius and a short segment near r_{cr} that connects the two spiral patterns.

However, compared to the Cowling approximation, the growth rate of the $m = 1$ mode is amplified by almost a factor of 1.5, and there are reasons to believe that the outspiraling motion of the BH is responsible for this amplification. The mechanism which drives the unstable outspiraling motion of the BH is similar to the one described in [142]. The disk creates a hilltop potential, which has a maximum at the origin, so the BH initially is located at the point of unstable equilibrium. The BH can reduce its potential energy by converting it into kinetic energy of orbital motion around common center of mass (CM) of the disk+BH system. Such orbital motion requires angular momentum which can be borrowed from the disk through the development of

[1] We remind the reader that the disk rotates counterclockwise on all $\varphi_m - r$ diagrams.

a non-axisymmetric $m = 1$ mode. Because the orbital motion of the BH requires a compensating displacement of the disk CM, removing angular momentum from the disk increases the amplitude of the $m = 1$ mode, in this case the PP-mode.

Next we consider the dominant non-axisymmetric modes that develop in the simulation AF2, in which an $m = 2$ density perturbation was added. Fig. 6.5 presents the time evolution and radial profiles of G_m and φ_m of these modes. Comparing Fig. 6.5 to Fig. 6.2 which presents the same set of diagrams for the Cowling simulation AC2, we can see that the type of the $m = 2$ mode in this simulation is quite different from the PP one observed in the simulation AC2. First, on the $D_m - r$ diagram in Fig. 6.5b, the minimum of D_m lies inside r_c, unlike the case of PP mode where such minimum is located close to the mode corotation radius r_{cr}. Second, the $\varphi_m - r$ diagram of the $m = 2$ mode in Fig. 6.5d consists only of trailing spirals and does not have a leading spiral pattern inside corotation, specific for PP modes. Finally, as Fig. 6.5d illustrates, the mode phase angle makes an abrupt turn by $\pi/2$ radians near r_c, which is the case when the disk were subjected to an elliptic (bar-like) deformation.

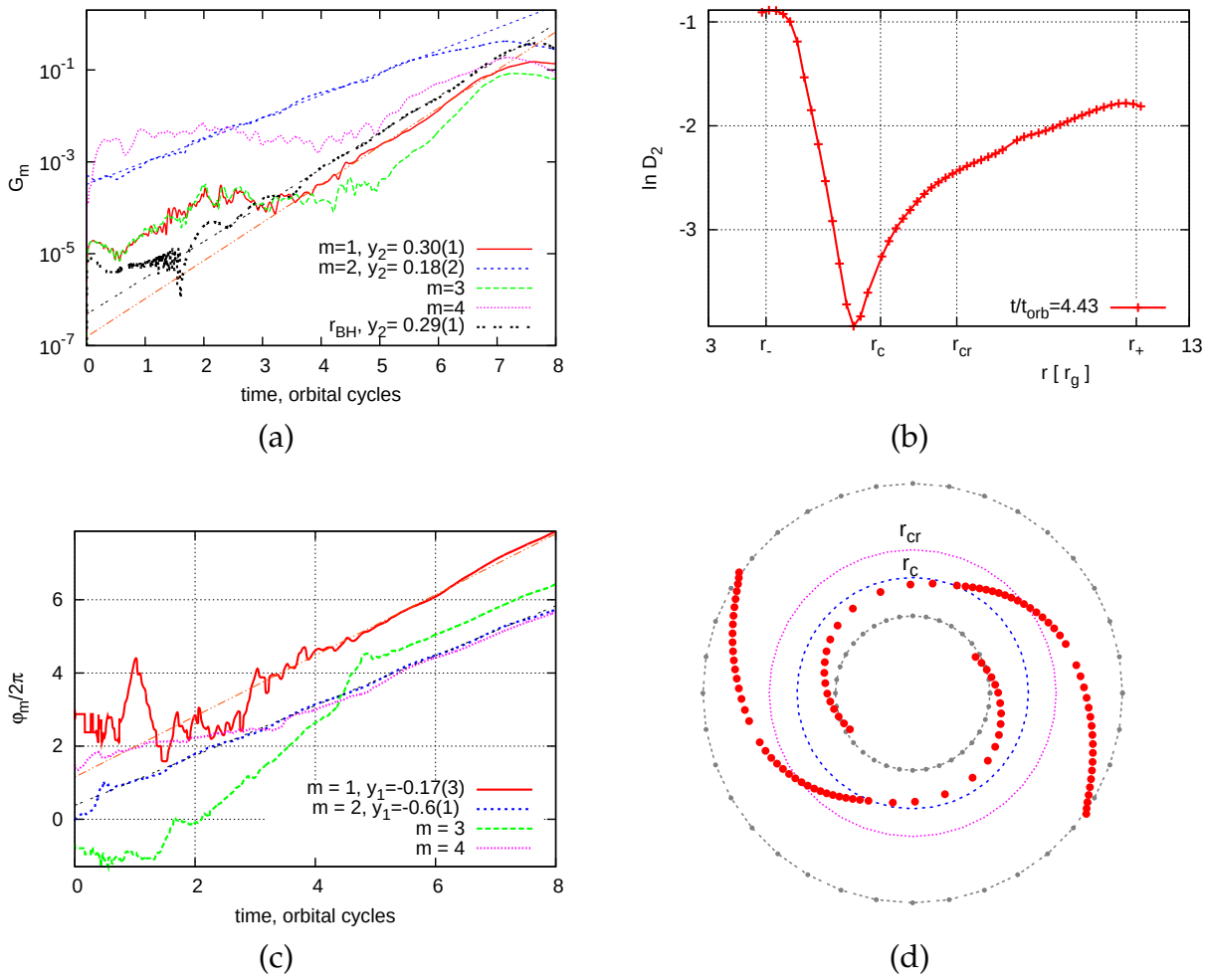

Figure 6.5: The behavior of the dominant non-axisymmetric modes and the radial character of the $m = 2$ I-mode in the simulation AF2 (see captions to Fig. 6.2 for details).

Overall, this mode looks very similar to the so-called intermediate type (I-type) modes found in earlier studies using Newtonian gravity (see, e.g. [30–32, 82]). In particular, [82] observed the I-modes in 3D Newtonian simulations of self-gravitating disks with various disk-to-central object mass ratios M_D/M_c and values of parameter $T/|W|$ (see Section 4 in [82]). A subset of their models that develop the I-mode instability (namely E31 and E32) have parameters $M_D/M_c = 0.2$, $T/|W| \sim 0.47$ and $4\pi G\rho/\Omega_c \sim 4$, which are comparable to those of our models A or B (listed in Table 4.1) [2].

Notice that in this simulation the $m = 1$ mode is also excited, as can be inferred from Fig. 6.5a.

[2]Note that in order to study the development of $m = 2$ modes [82] used a different approach from ours. Instead of adding an artificial perturbation with $m = 2$, they simulated only half of the domain, imposing the so-called π-symmetry, which leaves only even modes. In this regard, our method is more physically motivated.

The growth rate and pattern speed of this mode is the same as in simulation AF1 (cf. Table 6.3). The $m = 1$ mode development is again correlated in time with outspiraling motion of the BH, which is apparent in Fig. 6.5a. The analysis of the mode character, similar to the one performed above confirms that in this simulation the $m = 1$ mode has the same (0,0) PP type as in the simulation AF1. It grows faster than $m = 2$ mode, so that both modes become of comparable amplitude by the end of the simulation. The radial character of the two co-existing modes is depicted on Fig. 6.6, which shows a sequence of snapshots of the $\varphi_m - r$ diagrams at different times, superimposed with the disk density in equatorial plane.

In the case of model C, we used artificial density perturbations with $m = 1, 2, 3$ and observed the development of four unstable modes. The same analysis that we have done before for models A and B reveals that only the $m = 1$ mode has PP type, while the modes with $m = 2, 3, 4$ have I-type. The I-modes with $m = 3$ and $m = 4$ represent triangular and square deformations of the disk. Such modes were previously observed in Newtonian simulations of narrow self-gravitating annuli [31]. Fig. 6.7 shows the time behavior of G_m and r_{BH}/r_g for simulations of model C with different added perturbations. As can be seen from these plots, the fastest growing mode is the I-mode with $m = 3$, while the slowest one is the $m = 1$ PP mode (also, cf. Table 6.3). The latter remains subdominant in all simulations, its growth does not show clear exponential behavior and it is poorly correlated with the outspiraling motion of the BH. This happens because the $m = 1$ mode does not have enough time to form a global coherent pattern, which could counterbalance the BH with respect to their common center of mass. However, as soon as the amplitude of the $m = 1$ mode reaches $G_m \sim 10^{-4}$, it shows better correlation with the motion of the BH, as can be seen on Fig. 6.7 for simulations CC1 and CC3.

Finally, we need to point out that the comparisons with the Cowling simulations presented in this chapter should be taken with a grain of salt. The initial perturbation introduced by the blending of two metrics in the initial data changes the BH mass by small amount ($\sim 2\%$), which not only drives the disk out of equilibrium, but also changes the equilibrium configuration itself. Therefore, strictly speaking, the disks in Cowling and full GR represent different objects and cannot be compared. As a result, these disks will have different evolutionary paths not only due to dynamical GR effects, but also due to differences in BH masses. However, because the latter

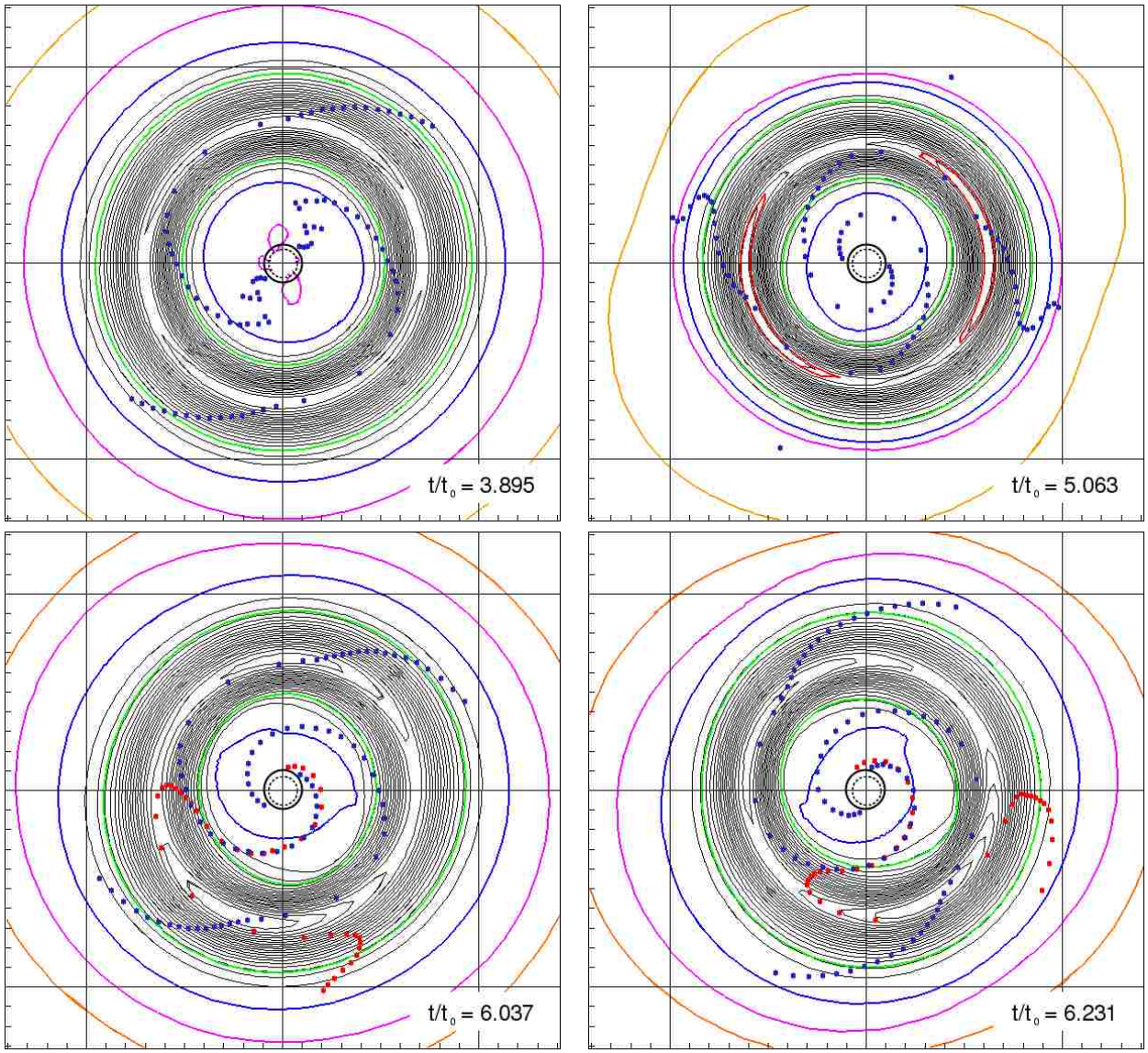

Figure 6.6: A sequence of four successive snapshots of the disk density in the equatorial plane, combined with the corresponding $\varphi_m - r$ diagrams for the $m = 1$ and $m = 2$ modes for the simulation AF2. The radial character of the $m = 1$ and $m = 2$ modes is represented by a sequence of red and blue dots resp.

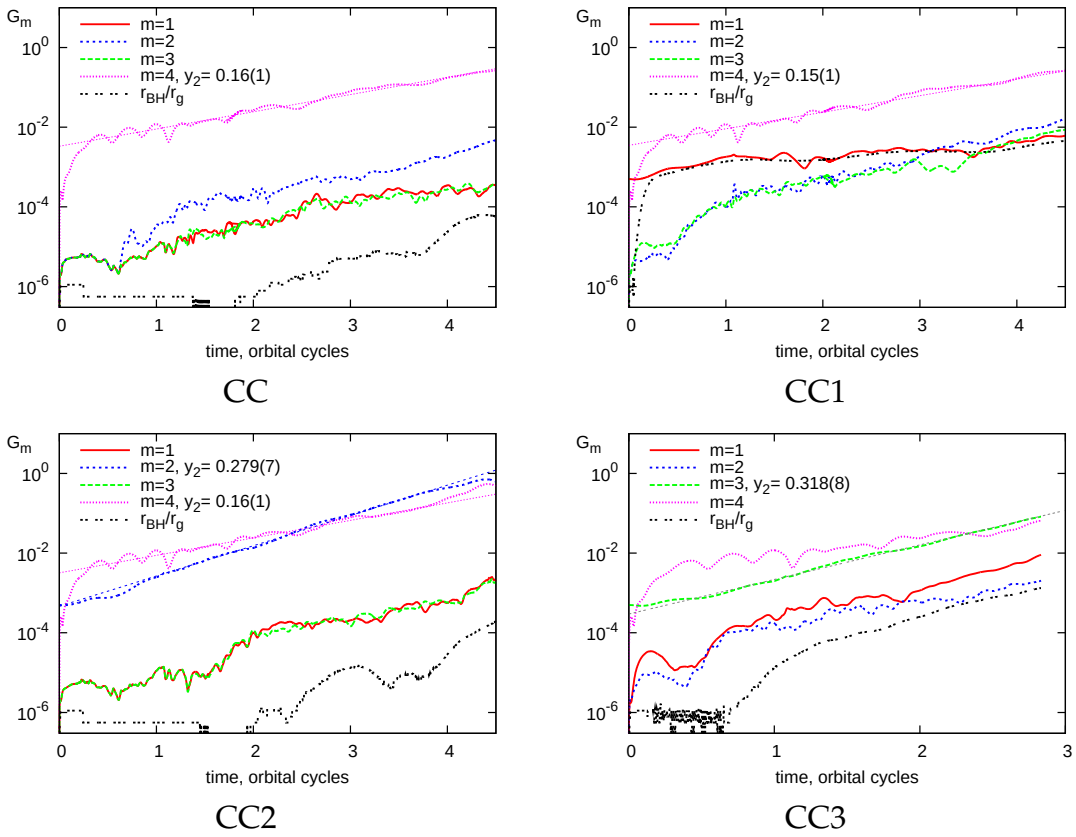

Figure 6.7: $G_m - t$ diagrams for modes with $m = 1 - 4$ in simulations with disk model C

is small, we assume that the differences in evolution are mainly caused by the former, implying that the comparison can indeed reveal GR effects.

Chapter 7. Solving Einstein Constraints with Finite Element Methods*

This work is part of an effort to numerically solve Einstein equations on general domains with arbitrary shapes and topologies. Accurate simulations on such domains require multiple numerical grids covering different areas of the domain, possibly refined where the solution has interesting features. For the numerical discretization one can use either finite differences (FD), spectral methods, or finite elements (FE). Current research in the numerical relativity community is dominated by finite differences methods, not the last reason for that being the relative ease of finite differences implementation and parallelization. A lot of important results in the areas of hyperbolic solvers, boundary conditions, domain representation, apparent horizon finders, wave extraction, stability proofs etc., were established and successfully implemented using the FD methods (see [159, 160] and references therein).

Spectral methods are also widely used [161, 162], mainly for solving elliptic equations, such as those arising in initial value problems [62, 163–166], constrained evolution [167] and apparent horizon finders [168, 169]. They can as well be applied to hyperbolic problems [170], as in the recent very successful simulations of the binary black holes merger [71] (using an approach, developed by the Cornell-Caltech collaboration [65, 171–173]). Spectral methods can produce exceptionally accurate results, but in order to use these results in a FD evolution code one needs to perform an additional interpolation step. The interpolation can be too slow for some applications, for instance, in constrained evolution schemes. In our approach, the interpolation is trivial, and the number of degrees of freedom on FE and FD grid is the same, which allows to exchange

*This chapter and the subsequent chapters are reprinted from the Article in a journal reference below. The Journal Permission to retain author rights to reprint the Article are given in Appendix B.

O. Korobkin, B. Aksoylu, M. Holst, E. Pazos, M. Tiglio, "*Solving the Einstein Constraint Equations on Multi-block Triangulations Using Finite Element Methods*", Class. Quant. Grav. **26** (2009) 145007

solution between the FE and FD solvers without reducing its accuracy by interpolation. Another advantage of FE methods compared to spectral methods is that the matrices resulting from FE discretizations are sparse.

Finite element methods can also be applied to hyperbolic problems, however, stable and accurate discretizations require using discontinuous Galerkin (DG) flavor of finite elements (otherwise the approximation is suboptimal: order of convergence falls to $(p-1)$ and the solution is not necessarily stable).

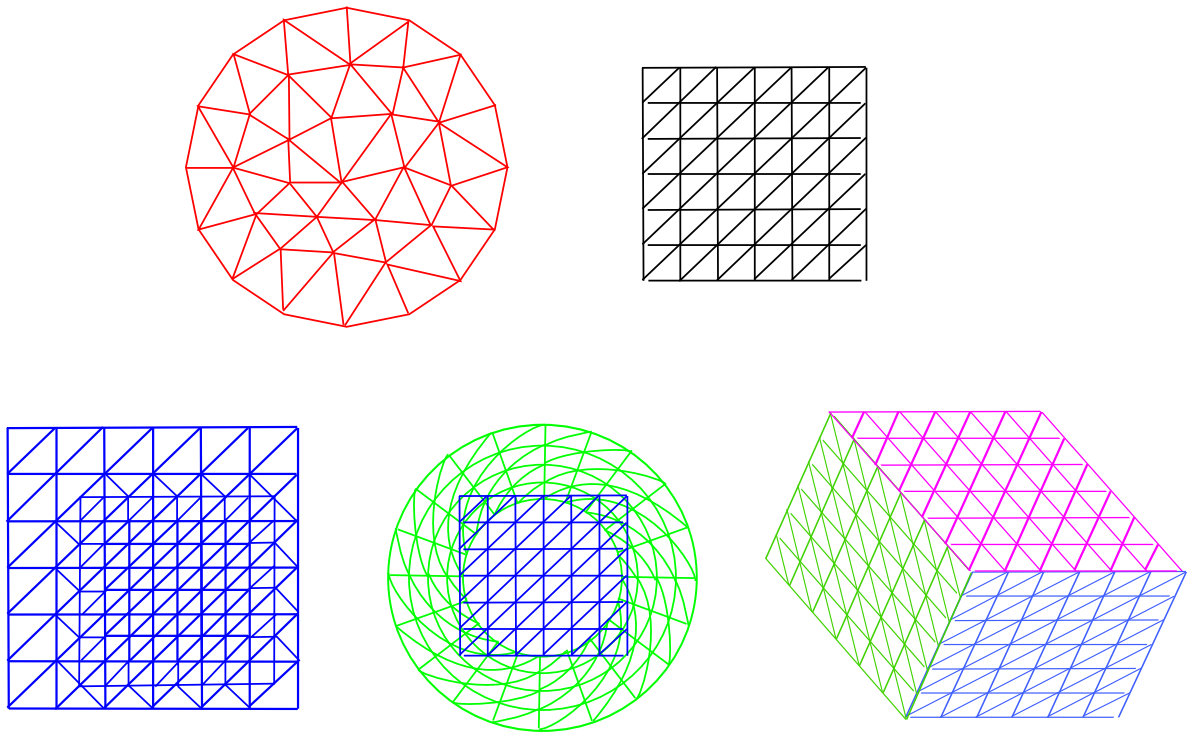

Figure 7.1: Types of FE meshes. Top left: unstructured mesh, top right: regular mesh, bottom: semistructured meshes.

In the following chapters, the term *grid* is used in reference to the finite differences grid (an ordered set of points), as opposed to the term *mesh* for the finite element triangulation. Domain triangulations can be classified as *regular*, *unstructured* or *semistructured*, depending on their degree of symmetry (see Fig. 7.1). Finite element methods can handle domains of arbitrarily complex shapes and topologies, since every geometrical shape admits approximation with successively refined unstructured symplectic triangulations. However, the domains encountered in numerical relativity are relatively simple in the sense that they can be covered with semistructured

meshes. We argue in favor of using semistructured meshes over unstructured ones. One of the motivations is that they can be quickly constructed on top of existing FD grids without the need to explicitly maintain all the information about mesh elements, such as edges, faces etc. Raising the order of finite elements, one can essentially achieve the spectral convergence; however, here we concentrate on lower-order finite elements (first- and second-order), and show how the *superconvergence* on semistructured grids for second-order elements can be exploited to obtain accurate 4-th order convergent solution, suitable for use in finite differences simulation.

This method is tested on the particular example of *multiblock* FD grid, introduced in Section 1.1. As described in that Section, this type of grid has several advantages over simple or refined rectangular grid with respect to solving the Einstein equations in 3D.

Einstein equations can be written in such a form that the equations split into hyperbolic (evolution) and elliptic (constraint) sub-systems. When solving the Einstein *vacuum* (that is, in the absence of matter) evolution equations, these can be cast in linearly-degenerate form, and the solutions are in general expected to be smooth. Those cases are ideally suited for high order or spectral methods. When including matter, on the other hand, for example when dealing with the general relativistic hydrodynamics equations, shocks are expected. In those cases a possible choice is high resolution shock capturing methods [80, 174] adapted to the presence of several blocks for the hydrodynamical sub-system and high order or spectral methods for the metric sub-system [49, 175].

This work is concerned with the elliptic sector of Einstein equations, more precisely with the generation of *initial data* needed for evolutions on multipatch geometries. Initial data on a space-like hyperslice has to satisfy a set of Einstein constraints, which can be cast into a coupled nonlinear elliptic system of partial differential equations (PDE). This elliptic PDE system has been studied extensively for many years, with a complete solution theory developed in the case of domains which are closed (i.e. compact without boundary) 3-manifold spatial slices of spacetime with constant or nearly-constant mean extrinsic curvature [176, 177]. More recently, this solution theory has been extended to both closed 3-manifolds and to compact 3-manifolds with boundary, having mean extrinsic curvature far from constant [178–180]. It has also been shown recently [44, 181, 182] that geometric partial differential equations of this type can be

solved accurately and efficiently using adaptive finite element methods on manifolds with general topologies. For general multi-block systems, the additional structure allows one to construct semi-structured triangulations, which generate superconvergent finite element solutions. The property of superconvergence holds at the vertices of the multi-block grid triangulation, which simplifies transport of the solution to the finite difference grid, since no interpolation is required.

The above considerations define the approach of this work, which involves solving the Einstein constraint equations on semi-structured multi-block triangulations using finite element methods. We apply this approach to the Brill wave initial data problem, which represents a linear vacuum case with zero extrinsic curvature, with the constraints system reducing to a single elliptic equation $\Delta\psi - V\psi = 0$ for the conformal factor ψ (where Δ is the flat 3-dimensional laplacian and V is a potential function related to the Ricci scalar of the freely given metric). Nevertheless, the results presented are expected to hold in general case, because the property of superconvergence is the property of the mesh and the finite element spaces used. If this property holds for a linearized problem, it is also expected to hold for the full nonlinear one (see Chapter 9 of [183]).

Chapter 8. Finite Element Toolkit (FETK)

In this paper we use the Finite Element ToolKit (FETK) [44] (see also [182, 184]) to solve the Einstein constraint equations. FETK is an adaptive multilevel finite element code developed over a number of years by the Holst research group at UC San Diego and their collaborators (see also [185]). It is designed to produce provably accurate numerical solutions to nonlinear elliptic systems of tensor equations on (Riemannian) multi-dimensional manifolds in an optimal or nearly-optimal way. We will summarize the main features of FETK here; more detailed discussions of its use for general geometric PDE may be found in [44, 181], and specific application to the Einstein constraint equations may be found in [182, 186].

FETK contains an implementation of a "solve-estimate-refine" algorithm, employing inexact Newton iterations to treat non-linearities. The linear Newton equations at each inexact Newton iteration are solved with unstructured algebraic multilevel methods which have been constructured to have optimal or near-optimal space and time complexity (see [187, 188]). The algorithm is supplemented with a continuation technique when necessary. FETK employs *a posteriori* error estimation and adaptive simplex subdivision to produce provably convergent adaptive solutions (see [189, 190]).

Several of the features of FETK are somewhat unusual, some of which are:

- Abstraction of the elliptic system: The elliptic system is defined only through a nonlinear weak form along with an associated linearization form over the domain manifold. To use the *a posteriori* error estimator, a third function $F(u)$ must also be provided (essentially the strong form of the problem).

- Abstraction of the domain manifold: The domain manifold is specified by giving a polyhedral representation of the topology, along with an abstract set of coordinate labels of the

user's interpretation, possibly consisting of multiple charts. FETK works only with the topology of the domain, the connectivity of the polyhedral representation.

- Dimension independence: The same code paths are taken for two-, three- and higher-dimensional problems. To achieve this dimension independence, FETK employs the simplex as its fundamental geometrical object for defining finite element bases.

8.1 Weak Formulation Example

We give a simple example to illustrate how to construct a weak formulation of a given PDE. Here we assume the 3–metric to be flat so that ∇ is the ordinary gradient operator and $\cdot$ the usual inner product. Let $\mathcal{M}$ represent a connected domain in $\mathbb{R}^3$ with a smooth orientable boundary $\partial\mathcal{M}$, formed from two disjoint 2-dimensional surfaces $\partial_0\mathcal{M}$ and $\partial_1\mathcal{M}$.

Consider now the following semilinear equation on $\mathcal{M}$:

$$-\nabla\cdot(a(x)\nabla u(x)) + b(x,u(x)) = 0 \text{ in } \mathcal{M}, \tag{8.1}$$

$$n(x)\cdot(a(x)\nabla u(x)) + c(x,u(x)) = 0 \text{ on } \partial_1\mathcal{M}, \tag{8.2}$$

$$u(x) = f(x) \text{ on } \partial_0\mathcal{M}, \tag{8.3}$$

where $n(x) : \partial\mathcal{M} \mapsto \mathbb{R}^3$ is the unit normal to $\partial\mathcal{M}$, and where

$$a : \mathcal{M} \mapsto \mathbb{R}^{3\times 3}, \qquad b : \mathcal{M}\times\mathbb{R} \mapsto \mathbb{R}, \tag{8.4}$$

$$c : \partial_1\mathcal{M}\times\mathbb{R} \mapsto \mathbb{R}, \qquad f : \partial_0\mathcal{M} \mapsto \mathbb{R}. \tag{8.5}$$

If the boundary function f is regular enough so that $f \in H^{1/2}(\partial_0\mathcal{M})$, then from the Trace Theorem [191], there exists $\bar{u} \in H^1(\mathcal{M})$ such that $f = \bar{u}|_{\partial_0\mathcal{M}}$ in the sense of the Trace operator (where $H^1(\mathcal{M})$ is the Hilbert space of all real L_2-integrable functions on $\mathcal{M}$ with L_2-integrable weak derivative [192].) Employing such a function $\bar{u} \in H^1(\mathcal{M})$, the weak formulation has the form:

$$\text{Find } u \in \bar{u} + H^1_{0,D}(\mathcal{M}) \text{ s.t. } \langle F(u), v\rangle = 0, \ \forall\, v \in H^1_{0,D}(\mathcal{M}), \tag{8.6}$$

where the nonlinear form is defined as:

$$\langle F(u), v\rangle = \int_{\mathcal{M}} \left(a\nabla u \cdot \nabla v + b(x,u)v\right)\, dx + \int_{\partial_1 \mathcal{M}} c(x,u)v\, ds. \tag{8.7}$$

The "weak" formulation of the problem given by equation (8.6) imposes only one order of differentiability on the solution u, and only in the weak or distributional sense. Under suitable growth conditions on the nonlinearities b and c, it can be shown that this weak formulation makes sense, in that the form $\langle F(\cdot), \cdot\rangle$ is finite for all arguments, and further that there exists a (potentially unique) solution to (8.6). In the specific case of the individual and coupled Einstein constraint equations, such weak formulations are derived and analyzed in [178, 179].

To analyze linearization stability, or to apply a numerical algorithm such as Newton's method, we will need the bilinear linearization form $\langle DF(u)w, v\rangle$, produced as the formal Gateaux derivative of the nonlinear form $\langle F(u), v\rangle$:

$$\begin{aligned}\langle DF(u)w, v\rangle &= \frac{d}{d\epsilon}\langle F(u+\epsilon w), v\rangle\Big|_{\epsilon=0} \\ &= \int_{\mathcal{M}} \left(a\nabla w \cdot \nabla v + \frac{\partial b(x,u)}{\partial u} wv\right)\, dx + \int_{\partial_1 \mathcal{M}} \frac{\partial c(x,u)}{\partial u} wv\, ds.\end{aligned} \tag{8.8}$$

Now that the nonlinear weak form $\langle F(u), v\rangle$ and the associated bilinear linearization form $\langle DF(u)w, v\rangle$ are defined as integrals, they can be evaluated using numerical quadrature to assemble a Galerkin-type discretization involving expansion of u in a finite-dimensional basis.

As was the case for the nonlinear residual $\langle F(\cdot), \cdot\rangle$, the matrix representing the bilinear form in the Newton iteration is easily assembled, regardless of the complexity of the bilinear form $\langle DF(\cdot)\cdot, \cdot\rangle$. In particular, the algebraic system for $w = \sum_{j=1}^{n} \beta_j \phi_j$ has the form:

$$AU = F, \quad U_i = \beta_i, \tag{8.9}$$

where

$$A_{ij} = \langle DF(\bar{u}_h + \sum_{k=1}^{n} \alpha_k \phi_k)\phi_j, \psi_i \rangle, \tag{8.10}$$

$$F_i = \langle F(\bar{u}_h + \sum_{j=1}^{n} \alpha_j \phi_j), \psi_i \rangle. \tag{8.11}$$

and $\{\phi_i\}_{i=1}^{N}$, $\{\varphi_j\}_{j=1}^{N}$ are the bases of the test and trial N-dimensional finite element spaces. As long as the integral forms $\langle F(\cdot), \cdot \rangle$ and $\langle DF(\cdot)\cdot, \cdot \rangle$ can be evaluated at individual points in the domain, then quadrature can be used to build the Newton equations, regardless of the complexity of the forms. This is one of the most powerful features of the finite element method, and is exploited by FETK to make possible the representation and discretization of very general geometric PDEs on manifolds. It should be noted that there is a subtle difference between the approach outlined here (typical for a nonlinear finite element approximation) and that usually taken when applying a Newton-iteration to a nonlinear finite difference approximation. In particular, in the finite difference setting the discrete equations are linearized explicitly by computing the Jacobian of the system of nonlinear algebraic equations. In the finite element setting, the commutativity of linearization and discretization is exploited; the Newton iteration is actually performed in function space, with discretization occurring "at the last moment."

Chapter 9. Semistructured Multiblock Triangulations

In order to avoid the extra step of interpolating the finite element numerical solution to a multi-block grid, we use finite element meshes with vertices located at the multi-block grid points. We construct such meshes by dividing a convex hull of the set of grid points into simplices with vertices only at those points. This procedure of building a simplicial mesh based on a set of points is usually referred to as *triangulation*. Delaunay's triangulation (see, for instance, [193]) is an example of such a procedure, generating meshes with simplices of the highest possible quality in flat space. Although Delaunay's triangulation minimizes a condition number in a resulting linear system, it is mostly used for sets of points of general position since it generates completely unstructured meshes; for more regular grids its algorithm is unnecessarily complex. Here we use a simpler and more straightforward algorithm to generate semi-structured meshes with the additional advantage of having superconvergent properties.

The term *superconvergence* applies in various contexts, when the local or global convergence order of a numerical solution is higher than one would expect [183, 194–196]. The type of superconvergence we are interested in is superconvergence by local symmetry [183], which occurs in function values for discretizations of second order elliptic boundary value problems, and amounts to an additional $0 < \sigma \leq 1$ in the convergence order. It occurs at any given point in which the finite element basis is locally symmetric, or approximately symmetric, with respect to local spatial inversion at that point (see Fig. 9.1). The triangulation method that we use produces simplicial meshes with this type of symmetry at all vertices inside each block, and at some vertices at the interblock boundaries. Therefore, in our meshes we expect superconvergence everywhere but at the non-symmetric interblock boundary points. For second order elliptic equations and piecewise polynomial finite elements of even degree superconvergence occurs in the solution itself, while for odd degree it occurs in the first derivatives of the solution [197,198].

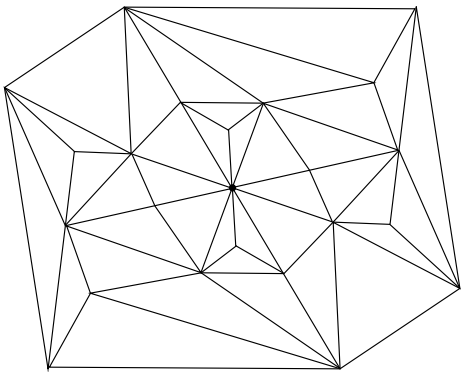

Figure 9.1: Example of two-dimensional symplectic mesh, locally symmetric with respect to the point [197].

With this in view, the quadratic Lagrange finite elements at the nodal points of the meshes that we use are expected to give solutions with convergence order $3 + \sigma$ (for some $0 < \sigma \leq 1$). This is an important advantage of multi-block triangulations: the resulting grid solutions have a convergence rate which is even higher than the global convergence rate of the original finite element solution, almost everywhere.

We start by dividing a cell, then combine cells into a block, and finally combine blocks together in a conforming way. Next we explain how these procedures are performed. The main complexity in building multi-block triangulations comes from the last step, since triangulations of each block are not necessarily conforming at their interfaces. We will show, however, that our method guarantees conforming simplicial triangulations.

Cell triangulation. For a cubical cell, there exist two possible triangulations (see Fig. 9.2): the cell can be divided into either five or six tetrahedra. The former is known as *middle cut triangulation* [199], and the latter as *Kuhn's triangulation* [200]. While Kuhn's triangulation produces simplices of equal shape and can be more easily extended to an arbitrary number of dimensions [201], the middle cut triangulation produces higher quality tetrahedra, in the sense that their angles are less acute than in a Kuhn triangulation, which produces to a finite element matrix system with better condition number. Usually, the quality of tetrahedra is described by the ratio $R/3r$ of radii of circumscribed (R) to inscribed (r) spheres. For a middle cut triangulation the central tetrahedron has, obviously, minimum possible aspect ratio $R/3r = 1$, while for corner tetrahedra we have $R/3r = \frac{1+\sqrt{3}}{2} \approx 1.37$. At the same time, in Kuhn's triangulation all

tetrahedra have aspect ratio $1 + 1/\sqrt{3} \approx 1.58$.

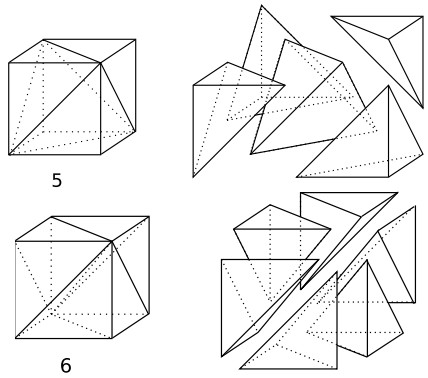

Figure 9.2: Middle cut triangulation and Kuhn's triangulation: dividing a cube into five or six tetrahedra, respectively.

Block triangulation. A block can be triangulated in many possible ways. We will consider the two most straightforward and symmetric ones, referring to them as *uniform* and *clustered* block triangulations. Both types of triangulation are locally symmetric with respect to local space inversion at any inner vertex of the mesh. In *uniform* block triangulation, exactly the same cell triangulation, with the same orientation, is applied to all cells in a block (see Fig. 9.3). This produces a conforming mesh for Kuhn's triangulation, but fails to produce a conforming one for the middle cut one, since the triangulation patterns between neighboring cell interfaces are not compatible.

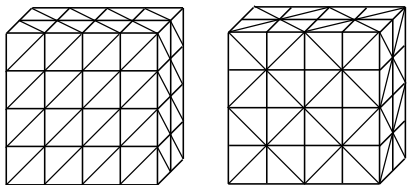

Figure 9.3: Uniform (left) and clustered (right) block triangulations. With Kuhn's triangulation of each cell, both types of block triangulation can be done in conforming way for neighboring cells. Cells, triangulated by middle cut, can only be arranged into clustered configuration.

To handle this compatibility problem, it is convenient to group neighboring cells into $2 \times 2 \times 2$ clusters and triangulate each cluster as shown in Fig. 9.4, with "union jack" patterns on each side. This guarantees conformity between neighboring clusters. We will label this type of triangulation as *clustered* block triangulation. It can be used with both types of cell triangulation.

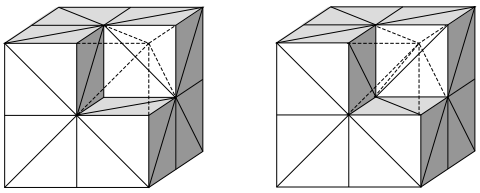

Figure 9.4: Union jack triangulation of $2 \times 2 \times 2$-cell cluster. The triangulation pattern on each side of the cluster is the same. Inside, each cluster can have either middle cut (left) or Kuhn (right) triangulations.

Multi-Block triangulation. In a multi-block system, both uniform and clustered triangulations of each block can be arranged into a conforming simplicial mesh. Obviously, clustered triangulations of each block with even number of cells on the interfaces between the blocks assemble themselves in a conforming manner. A uniform triangulations arrangement can be constructed from clustered triangulation of the same system by first removing and then replicating layers of cells with Kuhn's triangulation. Two different types of semi-structured multi-block triangulations, used in this paper, are shown in Fig. 9.5.

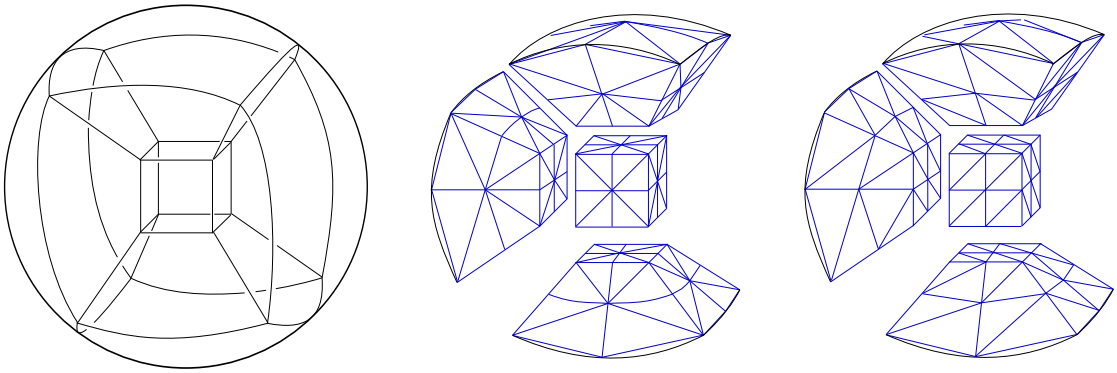

Figure 9.5: Seven-block system for the sphere (left), and its triangulations, generated using clustered (center) and uniform (right) block triangulations.

Chapter 10. Superconvergent FE Solutions

In this chapter we perform a numerical study of the quality of our finite element solutions obtained using semi-structured multi-block triangulations. We investigate not only the solution itself, but also answer the question of whether this solution is appropriate for finite-difference evolution codes with high-order numerical derivative operators. After introducing the domain structure and weak formulation of the second-order elliptic equation, we evaluate the solution convergence order, and show superconvergence for quadratic finite elements. Then we evaluate the finite element solution at the multi-block gridpoints, apply various high-order finite difference operators and check the convergence orders of its first and second numerical derivatives. The observed convergence orders are consistent with the expected values.

10.1 Domain Structure

Both FETK and QUILT were developed to handle equations on general manifolds, with an arbitrary number of charts. However, for the domain structures considered in this paper we can embed the computational domain into a reference Euclidean 3-dimensional space with a single fixed Cartesian system of coordinates to label all vertices and nodes of the mesh, and we do so. The domain of interest here will then be a spherical domain of radius R, equipped with a seven-blocks or thirteen-blocks system (see Fig. 10.1), with local block coordinate transformations defined as in [76], [91]. The seven-block geometry (see Fig. 10.1) is fully specified by fixing the outer sphere radius R_{out} and the side of the inner cubical block a_c. In the innermost, cubical block, there are $N_x \times N_y \times N_z$ points, where $N_x = N_y = N_z := N$. Since the grids are conforming, in the six blocks surrounding the inner one there are $N \times N \times N_r$ points. The thirteen-block geometry, in turn, can be seen as a seven-block one of radius R_{med} and $N \times N \times N_{r,in}$ points, surrounded by six additional blocks with $N \times N \times N_{r,out}$ points each, with a total radius R_{out}.

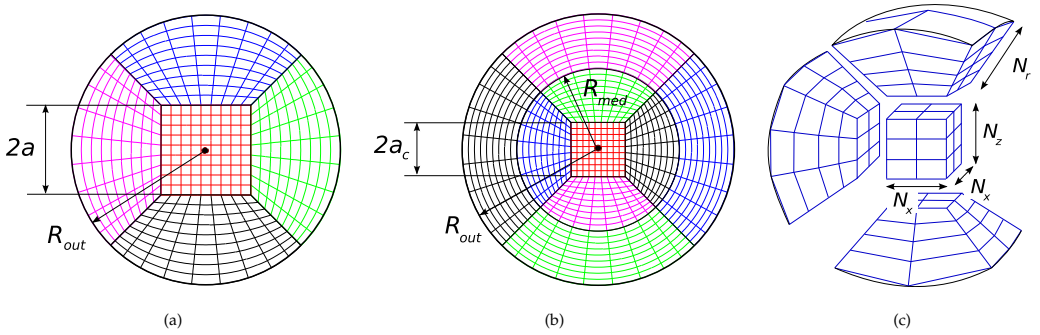

Figure 10.1: An equatorial cut of (a) seven-block and (b) thirteen-block systems. (c) Grid dimensions for the seven-block system.

The advantage of the thirteen-block setup is that the transversal grid layers in the outermost system are perfectly spherical surfaces. These are very convenient in certain applications which require integration over such surfaces, as in the the study of the multipole structure of radiation in the wave zone (see, for example, [50]), since no interpolation is needed for those integrations (resulting in both higher accuracy and speed). Throughout this paper, when we change the resolution we keep the ratios $N : N_r$ and $N : N_{r,in} : N_{r,out}$ in the seven- and thirteen-block systems, respectively, fixed. Multiple domains with different values of N produce a sequence of domain triangulations $\{\mathcal{T}_h\}$ with maximal simplex diameters h inversely proportional to N. Therefore, it is convenient to use N as a scaling factor in convergence tests, and we do so.

10.2 Test Problem

Let S_R represent our spherical domain with radius R, centered at the origin, and let ∂S_R be its outer boundary. The equations of interest in this paper are of the form:

$$-\nabla^2\psi(\bar{x}) + V(\bar{x})\psi(\bar{x}) = 0 \text{ in } S_R, \tag{10.1}$$

$$\psi(\bar{x}) = \psi_D \text{ on } \partial S_R \tag{10.2}$$

where ψ_D is a Dirichlet boundary condition, and ∇^2 is the Laplace operator. We only consider the case when both the potential V and the boundary conditions ψ_D are axisymmetric. Following the weak formulation example above (Section 8.1), we obtain the nonlinear weak form and the

bilinear linearization form:

$$\langle F(\psi), \phi \rangle = \int_{S_R} (\nabla\psi \cdot \nabla\phi + \psi V \phi) \; dx \tag{10.3}$$

$$\langle DF(\psi)\chi, \phi \rangle = \int_{S_R} (\nabla\chi \cdot \nabla\phi + \chi V \phi) \; dx \tag{10.4}$$

with $\psi(\bar{x}) \in \bar{\psi} + H_0^1(S_R)$, and $\phi(\bar{x})$, $\chi(\bar{x}) \in H_0^1(S_R)$ as discussed in Chapter 8. These two forms and the Dirichlet boundary function are everything we need to specify the problem in FETK.

We also consider the same problem with more complex Robin boundary conditions:

$$\partial_r \psi(\bar{x}) = \frac{1 - \psi(\bar{x})}{r} \text{ on } \partial S_R \,, \tag{10.5}$$

which has the following nonlinear weak and bilinear linearization forms,

$$\langle F(\psi), \phi \rangle = \int_{S_R} (\nabla\psi \cdot \nabla\phi + \psi V \phi) \; dx + \frac{1}{R} \int_{\partial S_R} (\psi - 1)\phi \; ds \tag{10.6}$$

$$\langle DF(\psi)\chi, \phi \rangle = \int_{S_R} (\nabla\chi \cdot \nabla\phi + \chi V \phi) \; dx + \frac{1}{R} \int_{\partial S_R} \chi \, \phi \; ds \tag{10.7}$$

where now $\psi(\bar{x})$, $\phi(\bar{x})$, $\chi(\bar{x}) \in H^1(S_R)$. We will use these Robin boundary conditions when solving for Brill waves below in Section 11.

10.3 Convergence of the Solution

As a test problem for our approach to solving elliptic equations on a semi-structured grid using finite elements, we solve equation (10.1) with three different potentials:

$$\begin{aligned} V_A &= -3\omega^2, \\ V_B(r) &= \frac{2(r^2 - 3r_0^2)}{(r^2 + r_0^2)^2}, \\ V_C(\rho, z) &= -\frac{2}{Z}\left(1 + \frac{4z^2}{R}(S + \frac{\sigma_r r_0^2}{Z})\right) + \frac{2(2C + 3S)}{R} + 2\left(\frac{2rS}{R}\right)^2, \end{aligned}$$

where $R = r^2 - \sigma_r r_0^2 \cosh \frac{r^2}{r_0^2}$, $Z = z^2 + \sigma_z^2$, $C = \sigma_r \cosh \frac{r^2}{r_0^2}$, $S = \sigma_r \sinh \frac{r^2}{r_0^2} - 1$.

These are such that they produce the following solutions:

(A) Plane wave: $\psi_A(x,y,z) = \cos(\omega x)\cos(\omega y)\cos(\omega z)$

(B) Spherically-symmetric pulse with width r_0, concentrated at the origin, falling off with order $1/r^2$ as $r \to \infty$: $\psi_B(r) = \frac{1}{1+r^2/r_0^2}$

(C) Toroidal solution, with radius $\sim r_0$ and width $\sim \sigma_r$ in the radial direction and σ_z in the vertical one: $\psi_C(\rho,z) = (\cosh(\frac{r^2}{r_0^2}) - \frac{r^2}{\sigma_r r_0^2})^{-1}(1 + z^2/\sigma_z^2)^{-1}$

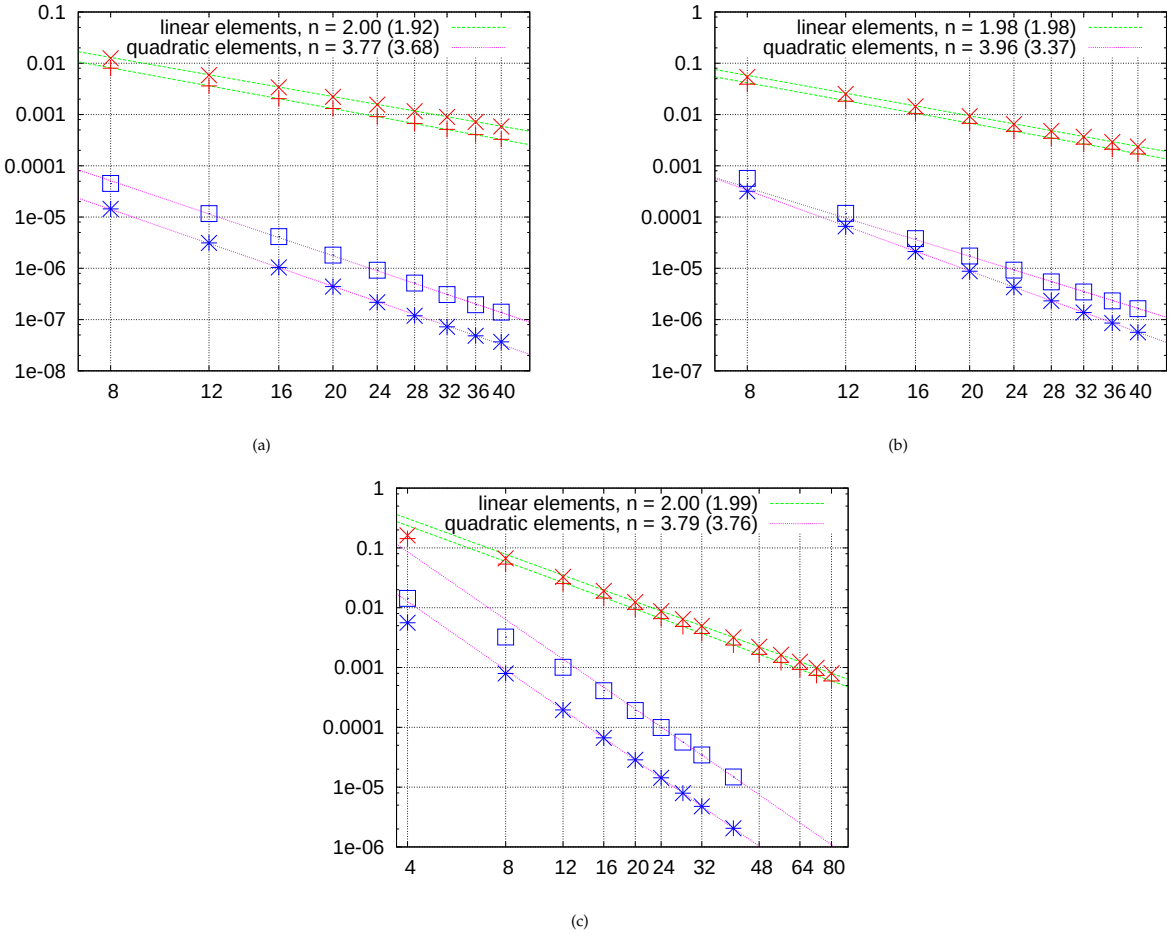

Figure 10.2: Convergence of the solution error, in the l_2 and l_∞ norms, with respect to the number of points N, for linear and quadratic finite elements. The plots (a), (b) and (c) correspond to the potentials V_A, $V_B(r)$ and $V_C(\rho,z)$, respectively. From each pair of lines, the upper one represents the l_∞ norm, and the lower one the l_2 norm. Each plot shows the convergence orders n, obtained by linear fit using the four points with highest resolution. The numbers in brackets give the convergence orders in the l_∞ norm.

These three potentials are chosen such that the solution for ψ is known in closed form, and they all differ in the way they are adapted to the underlying multi-block grid. The first potential, V_A, represents a simple periodic wave, with the mesh not adapted to the shape of the wave. Second potential is supposed to model a situation where the wave is concentrated near the origin, in the central cubical block of the "cubed sphere" domain. In this case, the grid resolution is adapted to the solution, but not the coordinate lines. Finally, for the potential V_C (which has toroidal shape), both the resolution (in the θ and r directions), and coordinate lines (in φ direction) are adapted to the solution.

All the test problems were solved on the same seven-block spherical domain, with dimensions $R_{out} = 10$, $a_c = 2.5$, and fixed grid size ratios $N : N_r = 1 : 2$. The test problems used the following set of parameters: for V_A: $\omega = 0.1$, for $V_B(r)$: $r_0 = 4$, and for $V_C(\rho, z)$: $r_0 = 8$, $\sigma_r = 1.2$, $\sigma_z = 4$.

It is well-known (see, for example, [202], [203], [204]) that in case of the optimal approximation, the convergence rate of continuum-level error norms, $||u_h - u_e||_2$ and $||u_h - u_e||_\infty$, defined in a usual manner,

$$||u_h - u_e||_2 = \left(\int_{\mathcal{M}} (u_h(x) - u_e(x))^2 dx \right)^{1/2}, \tag{10.8}$$

$$||u_h - u_e||_\infty = \max_{x \in \mathcal{M}} |u_h(x) - u_e(x)| \tag{10.9}$$

for the standard uniform refinement, is determined by the approximation power of the finite element function spaces (here, $u_e(x)$ is the exact solution, $u_h(x)$ is its finite element approximation, and index h denotes the maximum simplex diameter in the domain triangulation $\mathcal{T}_h$). If piecewise polynomials of fixed order p are used, then the order of convergence of the continuum-level error norms is $p + 1$.

In order to measure the error of the grid solutions, we use discrete l_2 and l_∞ norms, sampled at the nodes and normalized by the corresponding norm of u_e:

$$\epsilon_{h,2} = \frac{\left(\frac{1}{N}\sum_{k=1}^{N}(u_{h,k} - u_e(x_k))^2\right)^{1/2}}{\left(\frac{1}{N}\sum_{k=1}^{N} u_e(x_k)^2\right)^{1/2}} \qquad \epsilon_{h,\infty} = \frac{\max_k |u_{h,k} - u_e(x_k)|}{\max_k |u_e(x_k)|}$$

The plots on Fig. 10.2 show the convergence of $\epsilon_{h,2}$ and $\epsilon_{h,\infty}$ with N (N is inversely proportional to the maximum mesh diameter h, see Section 10.1). Note that the convergence orders in the l_2 and l_∞ norms agree, which means that the pointwise convergence order is the same everywhere. The observed convergence order for linear elements is 2, which is supposed to be the case, since the order of piecewise polynomials is odd. For quadratics, we expect to have superconvergence, and indeed, the observed convergence rate is ≈ 4.

10.4 Convergence of Numerical Derivatives of the Solution

To set up initial data for our General Relativity evolution codes, we need not only the solution itself but also its first spatial derivatives, because we use a first-order formulation of the Einstein evolution equations. In total, our finite element solution has to be differentiated twice: once, when setting initial data, and one more time when computing the evolution equations. In this section we numerically study how our obtained finite element solutions behave under two numerical finite-difference differentiations in terms of convergence.

If we were using completely unstructured meshes and interpolated the finite element solution to the multi-block grids used in our evolutions, the resulting grid solution would have an error of order $O(h^{p+1})$. Two numerical differentiations in this case would take away two orders of convergence, leading to an unacceptable low convergence order. However, as discussed above, when using semi-structured grids special conditions which lead to superconvergence can be met, and the convergence rate of numerical derivatives improve.

The procedure for converting the finite element solution into the grid solution is trivial: the value of the solution $u(x) = \sum_{i=1}^{N} c_i \phi_i(x)$ at a node i is simply the corresponding nodal coefficient c_i. In order for the nodes to coincide with the curvilinear gridpoint in the blocks, we restrict our finite element solutions only to vertex nodes, and omit other types of nodes, such as mid-edge ones.

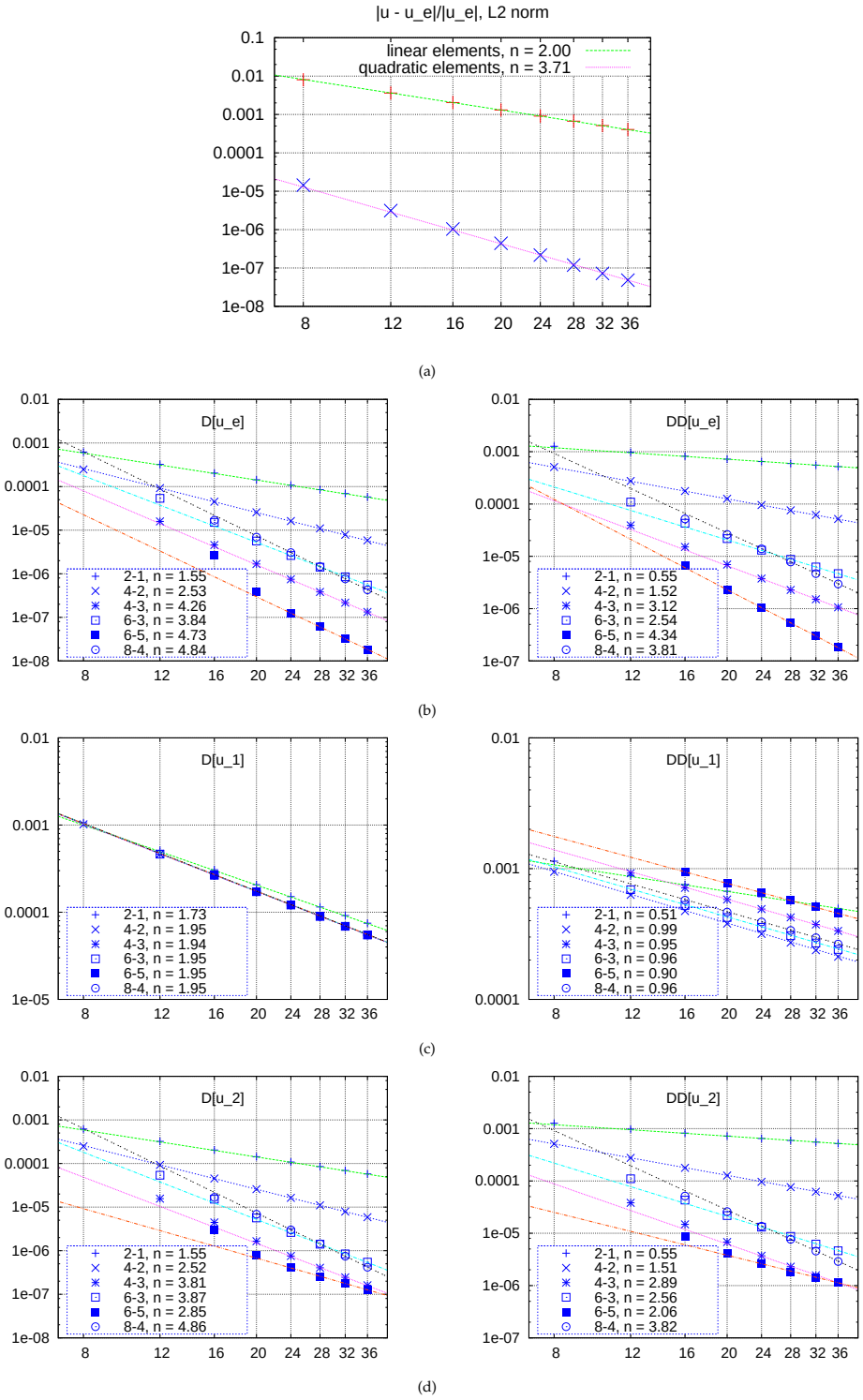

Figure 10.3: (a) Convergence of the solution error in the l_2-norm, for linear and quadratic finite elements, for the test problem with potential V_A and $\omega = 0.1$. (b,c,d) Convergence in the l_2-norm of the first (left) and second (right) numerical FD derivatives of: (b) the exact solution, restricted to the FD grid; (c) the numerical solution obtained using linear finite elements; (d) the numerical solution obtained using quadratic finite elements. In all cases several FD operators are used to compute the derivatives, and the resulting convergence factors (denoted by n) are shown

In our multi-block evolutions we use high-order finite differencing (FD) operators satisfying the summation-by-parts (SBP) property, as described in the Section 1.2 above.

After the finite element solution is converted to a grid function and then numerically differentiated with FD, the resulting convergence factor for the numerical derivatives depends not only on the order of the finite element basis polynomials, but also on the order of the FD operator. In general one expects that FD operators of sufficiently high order will preserve the original convergence of the finite element solution. This is a very nontrivial mathematical result in superconvergence theory (see Section 8.2 of [183] and references therein). In this section we test it for first and second FD derivatives (where by 'second FD derivative' we mean 'first FD derivative, applied two times', as opposed to a second-order FD derivative). The second FD derivative is expected be one order less convergent.

The results of our numerical experiments are illustrated by the Fig. 10.3 and summarized in tables 10.1 and 10.2. These tables list convergence orders in the l_2 and l_∞ norms for each SBP operator, applied once and twice to three different grid functions: the exact solution, the numerical solution obtained with linear elements, and the numerical solution obtained with quadratics. Test problem is the equation 10.1 with three test potentials: V_A with $\omega = 0.1$, V_B with $r_0 = 4$ and V_C with parameters $\sigma_r = 10$, $\sigma_z = 5$, $r_0 = 1.5$. For the potentials V_A and V_B we use a spherical domain with seven blocks, $R_{out} = 10$, $a_c = 2.5$, and grid size ratio $N : N_r = 1 : 2$. For V_C we use 13 blocks with $R_{out} = 20$, $R_{med} = 7$, $a_c = 1.5$, and grid size ratios $N : N_{r,in} : N_{r,out} = 1 : 1 : 1$.

Figure 10.3 shows in more details some of this information, displaying log-log plots of the l_2-norms of the errors of the solution and its first and second numerical derivatives, computed with various FD operators, for the problem 10.1 with the potential V_A.

Several conclusions can be drawn from these tables. In general, one expects the convergence order of the first FD derivative to be the smallest between the convergence order of the finite element solution itself and the convergence order of the SBP operator used to compute the derivative. Our results support this expectation: a) the first numerical derivative of the *exact solution* converges with the order of SBP operator used to compute it. b) The convergence order for the first derivative of the numerical solution obtained with linear elements approaches 2 for all SBP

Table 10.1: Top table: convergence orders of the solution error in the l_2-norm, for linear and quadratic finite elements, for the three test potentials. Middle and bottom tables: convergence orders of the first and second numerical derivatives, computed with different SBP operators.

potential	linear	quadratics
V_A	2.00	3.71
V_B	1.98	3.96
V_C	1.53	3.79

FE	V	D_{2-1}	D_{4-2}	D_{4-3}	D_{6-3}	D_{6-5}	D_{8-4}
u_e	V_A	1.55	2.53	4.26	3.84	4.73	4.84
	V_B	1.52	2.60	3.68	3.42	6.00	4.91
	V_C	1.59	2.59	3.98	3.85	6.34	5.61
u_1	V_A	1.73	1.95	1.94	1.95	1.95	1.95
	V_B	1.82	1.97	1.97	1.97	1.97	1.97
	V_C	1.47	1.47	1.47	1.47	1.47	1.47
u_2	V_A	1.55	2.52	3.81	3.87	2.85	4.86
	V_B	1.52	2.61	2.68	3.39	2.45	3.35
	V_C	1.60	3.15	3.91	3.93	3.82	4.06

FE	V	DD_{2-1}	DD_{4-2}	DD_{4-3}	DD_{6-3}	DD_{6-5}	DD_{8-4}
u_e	V_A	0.55	1.52	3.12	2.54	4.34	3.81
	V_B	0.51	1.60	2.65	2.36	4.69	3.72
	V_C	0.50	1.54	3.52	2.82	5.29	4.34
u_1	V_A	0.51	0.99	0.95	0.96	0.90	0.96
	V_B	0.49	1.26	0.93	1.01	0.87	0.97
	V_C	1.10	1.00	0.38	1.04	0.47	0.21
u_2	V_A	0.55	1.51	2.89	2.56	2.06	3.82
	V_B	0.52	1.60	2.06	2.33	1.61	2.86
	V_C	0.50	1.54	2.60	2.83	3.09	3.43

operators. c) The convergence order for the first derivative using quadratics improves as the SBP order increases. Eventually, when the operators D_{8-4} and D_{6-5} are used, the convergence order is either equal to the convergence of the finite element solution, or to the convergence order of the corresponding SBP operator.

The numerical results also show that second numerical differentiation takes away one order of convergence for all three grid functions. In particular, the second numerical derivative of linear elements solution fails to converge in the l_∞ norm (see table 10.2). Similarly, the second numerical derivative computed with the D_{2-1} operator fails to converge as well.

The most important conclusion from these results is that taking successive numerical derivatives of the grid function is only efficient for quadratics, i.e. when superconvergence takes place. In this case, the finite element error can be smaller than finite differencing one, and the conver-

Table 10.2: This table displays the same type of information of the previous one, but this time in the l_∞ norm.

potential	linears	quadratics
V_A	1.92	3.68
V_B	1.98	3.37
V_C	1.52	3.76

FE	V	D_{2-1}	D_{4-2}	D_{4-3}	D_{6-3}	D_{6-5}	D_{8-4}
u_e	V_A	0.99	2.02	4.70	3.33	4.32	4.69
	V_B	0.90	1.99	3.15	2.92	5.37	3.98
	V_C	1.04	2.14	3.63	3.47	6.26	4.99
u_1	V_A	0.95	0.99	0.98	0.98	0.98	0.98
	V_B	0.97	0.65	0.84	0.82	0.83	0.84
	V_C	1.47	1.47	1.47	1.47	0.55	1.46
u_2	V_A	1.00	2.02	2.13	3.19	2.00	4.52
	V_B	0.91	1.99	2.09	2.73	1.96	2.40
	V_C	1.04	2.09	3.03	3.70	3.13	3.35
FE	V	DD_{2-1}	DD_{4-2}	DD_{4-3}	DD_{6-3}	DD_{6-5}	DD_{8-4}
u_e	V_A	0.09	1.02	2.27	1.80	4.31	3.77
	V_B	-0.07	0.98	2.16	1.95	4.21	2.79
	V_C	0.05	1.10	2.09	2.29	4.89	3.80
u_1	V_A	0.11	-0.06	-0.05	-0.04	-0.07	-0.04
	V_B	-0.07	-0.27	-0.17	-0.10	-0.22	-0.08
	V_C	-0.47	-0.55	-0.60	-0.54	-0.61	-0.92
u_2	V_A	0.06	1.08	1.07	1.33	0.92	1.13
	V_B	-0.07	0.99	1.26	1.55	0.92	1.63
	V_C	0.05	1.11	2.42	1.65	2.56	2.41

gence rate of the latter is observed. For linear elements (and other elements of odd order), other techniques are required. One of the possible solutions is superconvergent gradient recovery, when the finite element solution is differentiated and then its discontinuous derivative is projected back onto original finite element space (sometimes with additional postprocessing, see, for example, [205], [206], [196], [207]) We do not pursue this direction, because superconvergent gradient recovery for linear element solution will only produce no more than second-order initial data, while for quadratics we already have third-order convergent initial data without extra effort.

10.5 Remarks about AMR

One of the main advantages of the finite element method in general and FETK in particular is fully adaptive mesh refinement (AMR). We have explored AMR in our semi-structured grids

through the following strategy: we start from a multi-block triangulation, adaptively refine it until the error reaches some predefined level, and read off the final result at the original multi-block triangulation nodes 10.4. In doing so, we have learned that for the type of problems we are solving for in this paper, AMR is not necessarily the most efficient strategy.

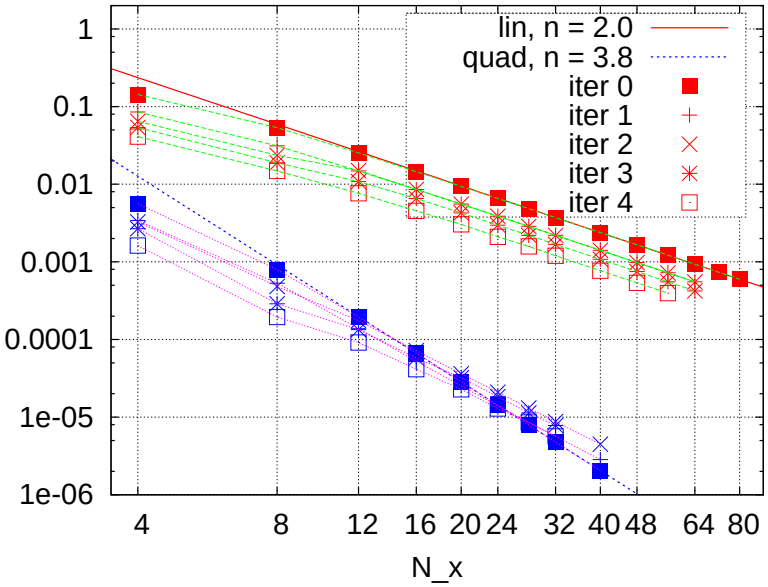

Figure 10.4: Error in the l_2-norm for the solutions obtained with linear and and quadratic finite elements with adaptive mesh refinement. The test problem used is that one of Section 10.3 with potential V_C. The straight lines represent the fitted convergence exponents. For linear elements, at each resolution we started with a semi-structured multi-block triangulation and did four AMR iterations. The l_2 norms of errors for these iterations are plotted with the same abscissa, corresponding to the initial resolution. For each resolution, the set of iterations done with quadratic finite elements is the result of p-refinement on the linear element meshes.

First of all, no matter how much the mesh is refined, in the end the finite element solution has to be restricted to the same FD grid. What matters for our purposes is the ability of the FD code to properly approximate the solution on this grid, and not at the refined FE mesh. The original FD multi-block grid is already adapted to be sufficiently fine to resolve all important features of the solution.

Second, in the cases here treated both the final solution is a rather regular smooth function, and the domain has regular boundaries. For such cases, standard uniform refinement gives just as good error reduction as AMR. AMR should be advantageous, though, in cases where, for example, the solution has non-smooth features or the domain has non-smooth boundaries.

Finally, the set of grid points where we sample the solution (that is, the multi-block ones) is very special. As already explained, the convergence order at these points is generally higher than one might expect. The special status of these grid points implies local symmetry of the finite element function spaces with respect to these points, which in turn implies superconvergence. AMR can easily break this symmetry and degrade both the error and the convergence order to the level of "ordinary" points. If we wanted to keep this symmetry and have superconvergence, we would have to refine at least within the entire block, but this would be almost as expensive as refining the entire domain uniformly.

Our experiments do not show particular advantage of using AMR compared to the uniform refinement of semi-structured multi-block triangulations. In our experiments we found that, in general, after a few refinement steps the AMR error saturates, while uniform refinement error continues to decrease. We have found that often, while decreasing the global l_2 norm, AMR leads to an increase in the l_∞ norm of the solution, because the local symmetry is broken at several grid points in the refined mesh.

We have also tried a simple form of p-refinement. Namely, using the same set of refined meshes for linear and quadratic elements (see Fig. 10.4). We chose several initial multi-block triangulation meshes with different resolutions and did four AMR iterations with linear elements. Then we used the same meshes to increase the order of finite elements to quadratics (p-refinement). It turns out that at high resolutions the meshes which give the best error reduction when going from linear to quadratic elements are initial triangulation meshes with no AMR. It happens so because the refined mesh loses the property of local symmetry at some of the grid points, the pointwise superconvergence for quadratic elements is lost and the global L_2-norm error is observed instead.

Chapter 11. Brill Wave Initial Data

In General Relativity, initial data on a spatial 3D-slice has to satisfy the Hamiltonian and momentum constraint equations [150, 208],

$$ {}^3R - K^{ij}K_{ij} + K^2 = 0 \tag{11.1} $$

$$ \nabla_i (K^{ij} - g^{ij}K) = 0 \tag{11.2} $$

where K_{ij} and K are the *extrinsic curvature* of the 3D-slice and its trace, respectively, and ${}^3R$ the Ricci scalar associated with the spatial metric g_{ij}.

Brill waves [209] constitute a simple yet rich example of initial data in numerical relativity. In such a case the extrinsic curvature of the slice is zero, and the above equations reduce to a single one, stating that the Ricci scalar has to vanish:

$$ {}^3R = 0\,. \tag{11.3} $$

If the spatial metric is given up to one unknown function, Eq. (11.3) in principle allows us to solve for such function and thus complete the construction of the initial data. The Brill equation is a special case of (11.3), where the 3-metric is expressed through the conformal transformation $g_{ij} = \psi^4 \tilde{g}_{ij}$ of an unphysical metric $\tilde{g}_{ij}$, with an unknown conformal factor ψ. Equation (11.3) then becomes [210]:

$$ (-\nabla^2_{\tilde{g}} + \frac{1}{8}\tilde{R})\psi = 0 \tag{11.4} $$

where $\tilde{R}$ and $\nabla^2_{\tilde{g}}$ are the Ricci scalar curvature and Laplacian of the unphysical metric $\tilde{g}_{ij}$, respectively.

Here we will focus on the axisymmetric case with the unphysical metric given in cylindrical coordinates by

$$\tilde{g}_{ij} = e^{2q(\rho,z)}(d\rho^2 + dz^2) + \rho^2 d\varphi^2\,, \tag{11.5}$$

where $q(\rho, z)$ is a function satisfying the following conditions:

1. regularity at the axis: $q(\rho = 0, z) = 0$, $\frac{\partial q}{\partial \rho}|_{\rho=0} = 0$,
2. asymptotic flatness: $q(\rho, z)|_{r\to\infty} < O(1/r^2)$, where r is the spherical radius $r = \sqrt{\rho^2 + z^2}$.

The Hamiltonian constraint equation (11.3) becomes a second order elliptic PDE, which with asymptotically flat boundary conditions at $r \to \infty$ takes the form

$$-\nabla^2\psi(\rho, z) + V(\rho, z)\psi(\rho, z) = 0, \tag{11.6}$$

$$\psi|_{r\to\infty} = 1 + \frac{M}{2r} + O(1/r^2), \tag{11.7}$$

with the potential $V(\rho, z)$ given by

$$V = -\frac{1}{4}(q''_{\rho\rho} + q''_{zz}).$$

We numerically solve this equation using FETK on the 13-block multi-block spherical domain described in Section 10.1 (see Fig. 10.1). We use domain parameters $R_{out} = 30$, $R_{med} = 7$, $a_c = 1.5$, and grid dimension ratios $N : N_{r,inner} : N_{r,outer} = 2 : 3 : 12$. Our low-medium-high resolution triple is $N = 32$, $N = 36$ and $N = 40$, except for pointwise convergence tests on the x-axis (see Fig. 11.3), where we use $N = 16$, $N = 24$ and $N = 36$ (since they all differ by powers of 1.5).

We impose Robin boundary conditions, as in equation (10.5). The weak form (10.6) and bilinear linearization form (10.7) for this problem are given in Section 10.2. Since first order elements lead to unacceptably low convergence orders for most general relativistic applications, from

here on we restrict ourselves to quadratic ones (which should give fourth order convergence if superconvergence is exploited).

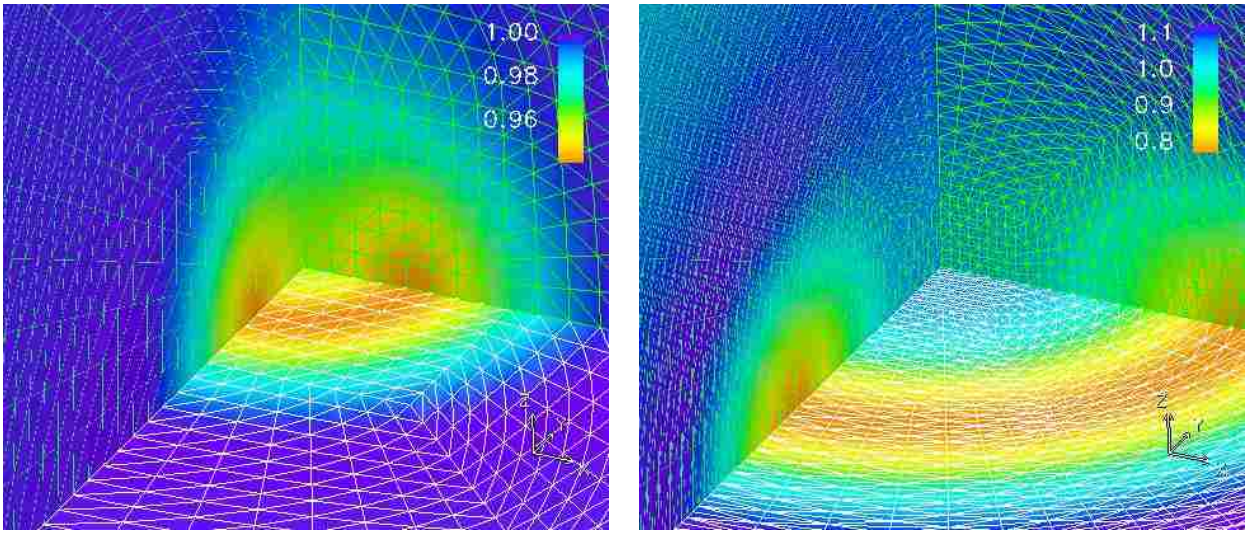

(a) (b)

Figure 11.1: Potentials for the two types of Brill waves considered: Holz' (a) and toroidal (b) forms.

We work with two specific choices for $q(\rho, z)$:

(a) Holz' form [211]: $q_H(\rho, z) = a_H \rho^2 e^{-r^2}$, with amplitude $a_H = 0.5$;

(b) toroidal form: $q_t(\rho, z) = a_t \rho^2 \exp\left(-\frac{(\rho-\rho_0)^2}{\sigma_\rho^2} - \frac{z^2}{\sigma_z^2}\right)$, with amplitude $a_t = 0.05$, radius $\rho_0 = 5$, width in ρ-direction $\sigma_\rho = 3.0$ and width in z-direction $\sigma_z = 2.5$.

Holz potential is chosen for historical reasons. It is suitable for evolutions using the cubed sphere system, because initially the wave is concentrated near the origin (at the central block), and later decays into a sequence of spherical waves. The cubed sphere grid resolves the wave well both at the initial moment, and during the subsequent evolution. For the toroidal potential, the cubed sphere system is adapted even better, since it efficiently removes the dependence on one of the angular coordinates, φ.

11.1 Importing the Initial Data into QUILT

Once we have constructed the initial data sets, we analyze and evolve them by importing them into QUILT. For evolutions we use the Generalized Harmonic (GH) first order symmetric hy-

perbolic formulation of the Einstein equations introduced in [51], which features exponential suppression of short-wavelength constraint violations; our multi-block implementation is described in [50].

The set of evolved variables in this system includes the 4-metric g_{ab}, its spatial derivatives $\Phi_{iab} = \partial_i g_{ab}$ and quantities $\Pi_{ab} = -t^c \partial_c g_{ab}$, where t^c is the unit normal vector to the spatial slice.

To set up the initial data, we first compute the $3+1$ quantities and then convert them to GH variables. The 3-metric $g_{ij}(x, y, z)$ is computed from the conformal factor $\psi(x, y, z)$, in Cartesian coordinates, using the expressions (which follow from 11.5):

$$
\begin{aligned}
g_{xx} &= \psi^4 (e^{2q} x^2 + y^2)/\rho^2, & g_{xy} &= \psi^4 (e^{2q} - 1) xy/\rho^2, \\
g_{yy} &= \psi^4 (x^2 + e^{2q} y^2)/\rho^2, & g_{zz} &= \psi^4 e^{2q}, \\
g_{xz} &= g_{yz} = 0
\end{aligned}
$$

where $\rho = \sqrt{x^2 + y^2}$. Then we construct the rest of the evolved variables, including the gauge source functions $H_a = -g^{bc} \Gamma_{a,bc}$ (here $\Gamma_{a,bc} = \frac{1}{2}(\partial_b g_{ac} + \partial_c g_{ab} - \partial_a g_{bc})$ are the Christoffel symbols). The extrinsic curvature is assumed to be zero, $K_{ij} = 0$, we also use unit lapse $\alpha = 1$, zero shift $\beta_i = 0$, and zero time derivative of lapse and shift: $\partial_t \alpha = \partial_t \beta_i = 0$.

11.2 Convergence of Initial Data and Hamiltonian Constraint

To estimate the quality of our initial data, we evaluate the Hamiltonian constraint violation using the SBP operators, which is in fact equivalent to an independent residual evaluation for the Brill equation (11.6). As is the case with just numerical derivatives, we find that the magnitude and convergence order of the Hamiltonian constraint violation depends on both the order of the SBP operator, and the order of finite elements. In total, computing the Hamiltonian constraint involves two numerical differentiations, therefore it has to converge with the same order as second numerical derivatives. We can see this convergence rate for different SBP operators in Fig. 11.2. Table 11.1 summarizes those results, along with the expected convergence orders for second numerical derivatives.

Consistent with what one expects, for finite difference operators of sufficiently high order

Table 11.1: Convergence orders of the Hamiltonian constraint for the two initial data sets in the l_2-norm.

q	D_{2-1}	D_{4-2}	D_{4-3}	D_{6-3}	D_{6-5}	D_{8-4}
Holz	0.59	1.42	2.03	2.01	1.86	2.58
Toroidal	0.58	1.75	2.55	3.08	2.55	3.96

the constraints converge with the same order as the finite element solution itself, which should be $3 + \sigma$ for some $0 < \sigma \leq 1$ (depending on the level of superconvergence obtained). Similarly, below in Chapter 12 we will show that the extracted gravitational waves have a similar convergence order.

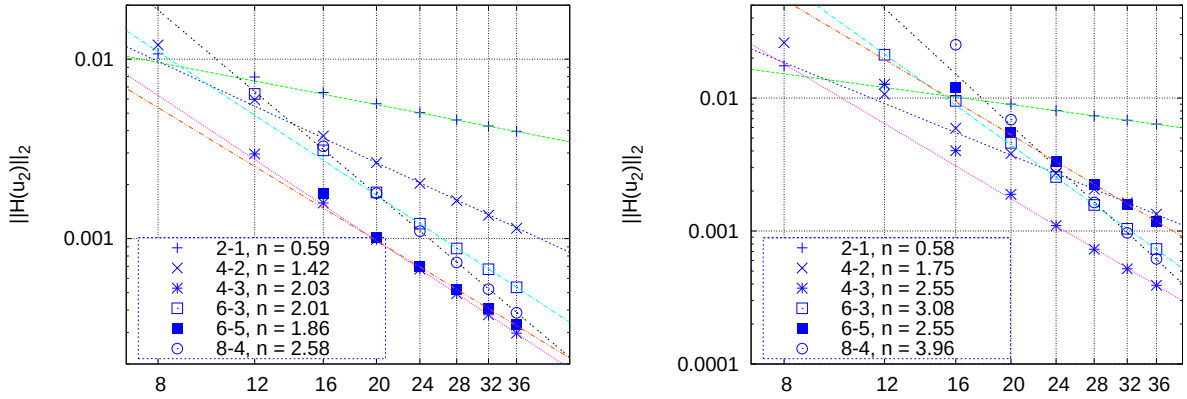

Figure 11.2: Convergence of the Hamiltonian constraint in the l_2-norm for Brill waves of Holz (left) and toroidal (right) type, computed using quadratic finite elements and different numerical SBP operators.

It is not difficult to see why the convergence order is lower for problem (a). This is the order we might expect for quadratic elements on completely unstructured meshes, without superconvergence. The reason that no superconvergence is observed in this case is the following. We have chosen the domain and the width of the Brill wave in such a way that around the boundary of the inner cubical block the solution varies significantly (see Fig. 11.3). Recall that the size of that block is $a_c = 1.5$ and the width of the gaussian in the function q is 1. But this is exactly the place where the local symmetry property is violated most (especially at the corners of the cube), and conditions for superconvergence are the least favorable. Everywhere else the solution varies very slowly and the error is small compared to the error at the boundary of the central cubical

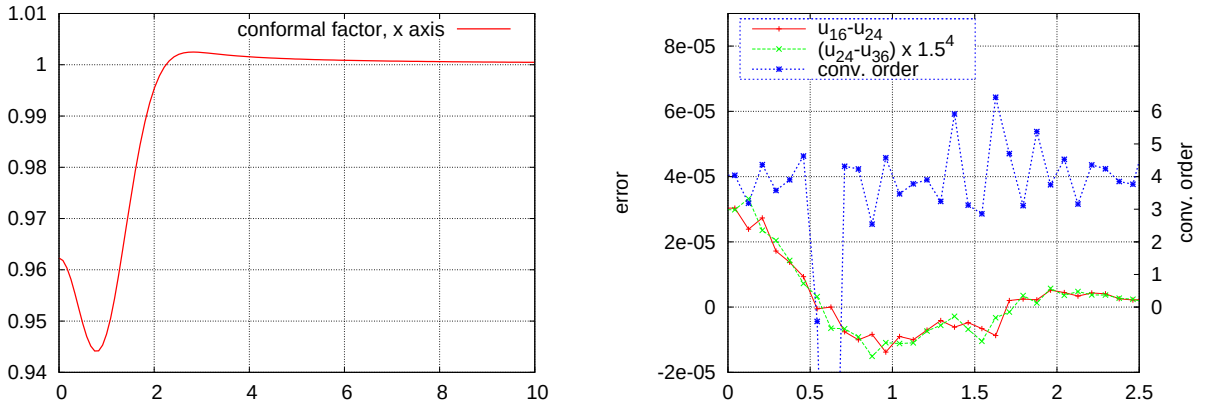

Figure 11.3: (a) 1-d cut through the Brill wave conformal factor ψ_{fine} for problem (a) along the x-axis. (b) Errors $\psi_{coarse} - \psi_{medium}$, $\psi_{medium} - \psi_{fine}$, and pointwise convergence order on the 1-d cut along the x-axis.

block. With increasing resolution this error dominates in both l_2 and l_∞ norms. The situation is better for the problem with toroidal potential, because most of the variation of the solution is located outside the central cube (recall that the radius of the toroidal wave we use is $r_0 = 5$); though this is still in the inner-blocks region (the radius of the spherical boundary between inner and outer blocks is $r_{med} = 7$).

Chapter 12. Evolutions of Brill Wave Spacetimes

We now demonstrate that our approach for generating initial data on multi-block grids using finite element methods can be successfully used in practice in fully nonlinear relativistic simulations. We do so by presenting results of multi-block evolutions of the Holz set of Brill initial waves constructed above.

In the notation of [51], we fix the damping parameters of the GH formulation to $\gamma_0 = \gamma_2 = 1$. We used the SBP operator D_{6-3} for spatial differentiations, a 4-th order Runge-Kutta time integrator with adaptive time stepping, and maximally dissipative outer boundary conditions.

The Brill wave amplitude $a_H = 0.5$ is in the subcritical regime (the critical value is around $a_{cr} \approx 4.85$ [211]). As a result the wave, initially concentrated near the center, dissipates and leaves the domain after a while. Fig. 12.1 shows a convergence plot in time for the Hamiltonian constraint during such evolution. We see that the Hamiltonian constraint converges with a factor of $2-3$ in the l_2 norm. This has to be one order less convergent than the solution itself, therefore we anticipate the solution to converge with a factor of $3-4$, which is in agreement with the pointwise convergence order of the conformal factor at the initial time (see Fig. 11.3).

We compute gravitational waveforms using a generalized Regge-Wheeler-Zerilli formalism, along the lines of [50, 212]. The four-dimensional spacetime metric is decomposed into a spherically symmetric "background" plus a small perturbation [213, 214]. The background part of the metric is identified with the Schwarzschild solution and the radiation content with the difference between the numerically computed solution and the background.

The background metric is written as

$$ds^2 = \tilde{g}_{\rho\tau}(t,r)dx^\rho dx^\tau + f^2(t,r)\hat{g}_{AB}dx^A dx^B. \tag{12.1}$$

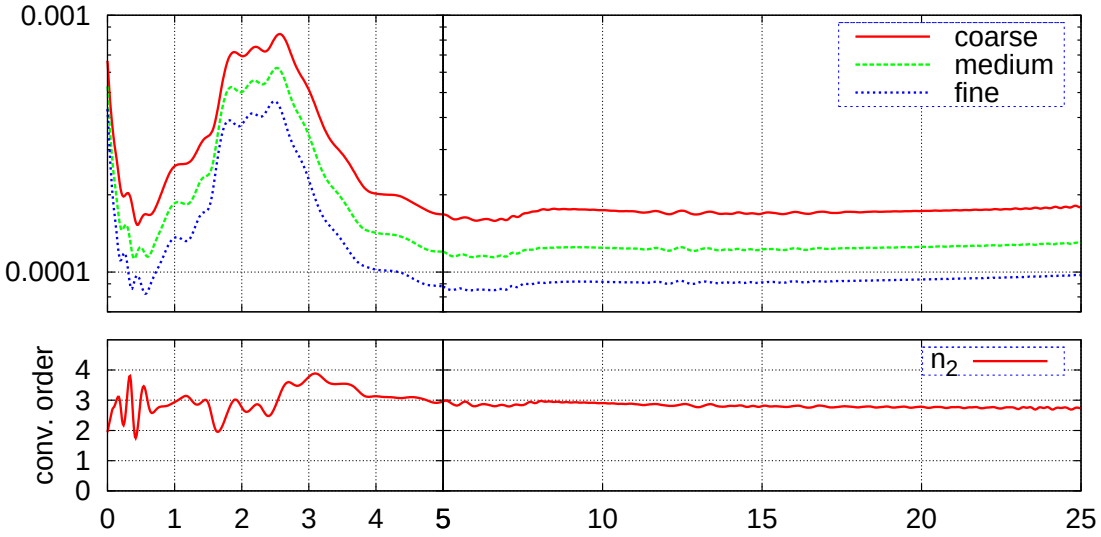

Figure 12.1: Convergence of the Hamiltonian constraint as a function of time during a multi-block evolution of the Brill wave initial data generated with finite element methods.

with the four-dimensional background manifold split as the product space of a two-dimensional one $\mathcal{M}$ endowed with coordinates x^ρ (with $\rho, \tau = 0, 1$ usually denoting the time and radial coordinate) and a unit 2-sphere S^2 with coordinates x^A (with $A = 2, 3$ commonly taken as the θ and ϕ polar spherical coordinates). Here $\tilde{g}_{\rho\tau}$ is the metric of the manifold $\mathcal{M}$ and f^2 is a positive function of x^ρ. If using the areal radius as a coordinate we have $f = r$. The metric of the 2-sphere is taken to be $\hat{g}_{AB} = \mathrm{diag}(1, \sin^2\theta)$ in polar spherical coordinates.

The metric perturbation is decomposed in terms of scalar, vector and tensor spherical harmonics [50, 215, 216]. The decomposition naturally splits the different (ℓ, m) modes into even $(-1)^\ell$ and odd $(-1)^{\ell+1}$ parity under reflections about the origin. The two different parities are handled separately. Odd and even-parity perturbations are described by the Regge-Wheeler [213] and Zerilli [214] functions, respectively.

The dominant modes in the evolutions of the Brill data constructed above are the $\ell = 2, 4$ even parity, axisymmetric ones (see Fig. 12.2). Figs. 12.3 and 12.4 display the corresponding Zerilli functions and their convergence behavior, extracted at a radius $r_e = 12.75$. The observed

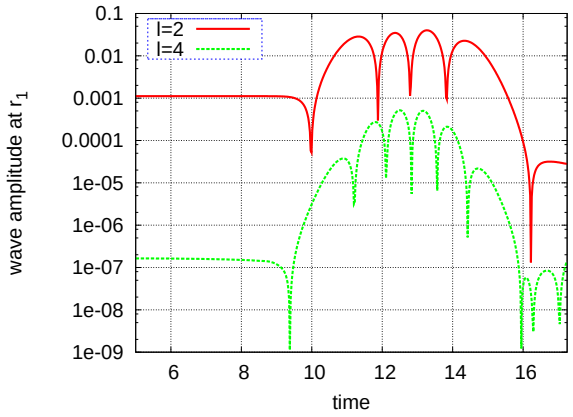

Figure 12.2: Nonzero components of gravitational radiation $\ell = 2$ and $\ell = 4$, $m = 0$, extracted at radius $r_e = 12.75$.

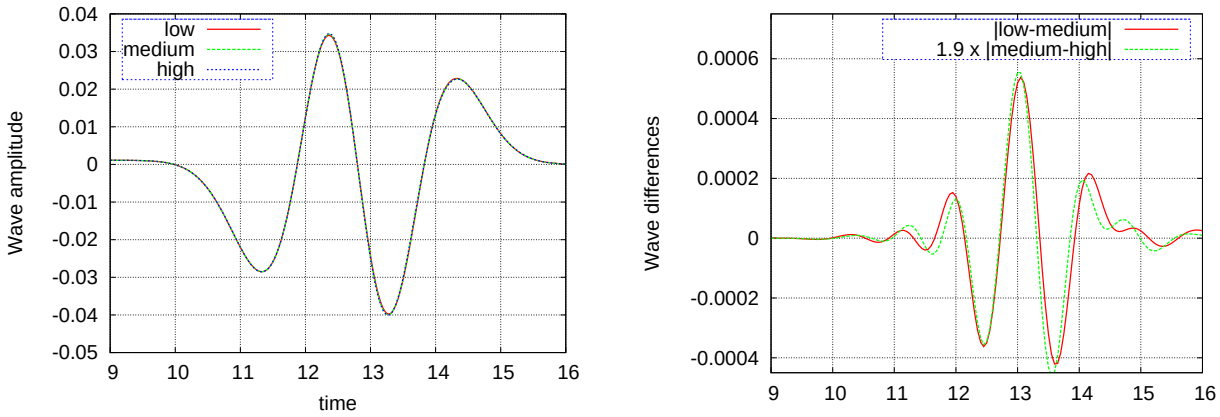

(a) (b)

Figure 12.3: Zerilli function (left) and self-differences (right) for the $(\ell = 2, m = 0)$ mode, scaled according to fourth order convergence.

convergence factors for the $\ell = 2$ and $\ell = 4$ modes are around four and three, respectively, which are consistent with the convergence factors from quadratic elements with superconvergence for the initial data and the D_{6-3} SBP operator and fourth-order Runge-Kutta for the evolution.

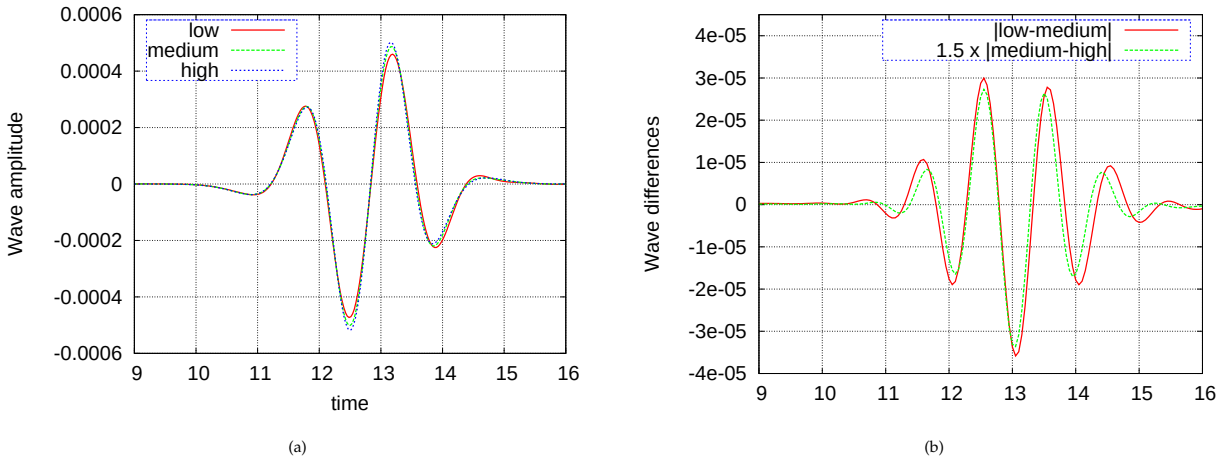

(a) (b)

Figure 12.4: Zerilli function (left) and self-differences (right) for the $(\ell = 4, m = 0)$ mode, scaled according to third order convergence.

Conclusion

- **Self-gravitating Disks**

In the work reported in this thesis we have explored the problem of non-axisymmetric instabilities in self-gravitating disks around black holes (BHs). To address this problem, we used 3D general relativistic hydrodynamical simulations including a full treatment of the Einstein equations. We studied several moderately slender and slender models with disk-to-BH mass ratio ranging from 0.11 to 0.24. The parameters of these models are listed in Table 4.1.

To obtain a self-consistent equilibrium disk model outside BH, we solve the coupled system of Einstein constraints and Euler equations using iterative Green functions approach, implemented in the RNSID code [97]. To avoid coordinate singularities, we transform the stationary initial data outside the BH horizon from quasi-isotropic to non-singular horizon-penetrating coordinates. We set the missing data inside the BH horizon to analytic Kerr-Schild solution and smoothly blend it with the computed data outside the horizon.

We evolve the metric using first-order form of the Generalized Harmonic formulation of the Einstein equations with adaptive constraint damping. The metric evolution equations are discretized on multiblock grid and solved using 8th order finite difference operators. We evolve the matter with relativistic Euler equations in flux-conservative form, using a finite volume cell-centered discretization scheme. We also use a Γ-law as the matter equation of state. Our numerical approach makes extensive use of the curvilinear mesh adaptation in order to achieve desired resolutions in different parts of the domain.

We have not observed the runaway instability in our models, which could have developed due to the disk overfilling its toroidal Roche lobe in the process of radial oscillations. Such radial axisymmetric oscillations of the disk around its equilibrium state are triggered in all of

our simulations by an axisymmetric perturbation in the metric. The latter is introduced into the initial data by the blending of two metrics inside and outside the BH horizon. Although our initial disk models are close to overfilling the toroidal Roche lobe, the radial oscillations do not lead to the development of the runaway instability within several initial orbital periods that we have simulated. However, this result may be specific to the particular model that we focused on; we can not exclude the possibility of the quick runaway instability development in models with different initial parameters.

In all models that were explored we observed unstable non-axisymmetric modes. We have performed detailed analysis of these modes to determine their types, growth rates, radial profiles and pattern speeds (see Table 6.3). For all simulations in Cowling approximation we observe the development of Papaloizou-Pringle (PP) instability with $m = 1 - 4$. For the simulations in full GR we observe two distinct types of instabilities. The unstable mode with $m = 1$ has PP type, similar to the one observed in Cowling case. Unstable modes with $m > 1$ become the intermediate modes (I-modes), representing elliptical, triangular or square deformations of the disk.

In full GR case, the development of the $m = 1$ PP mode is accompanied by outspiraling motion of the BH, which is correlated in time with the growth of the mode. Due to this motion, the $m = 1$ mode growth rate is higher by approximately ≈ 1.5 compared to the Cowling case. The overall picture of the unstable modes is qualitatively similar to the Newtonian case and consistent with previous works [28, 31, 82]

- **Superconvergent Finite Elements**

In this work we followed a finite element approach for generating initial data satisfying the Einstein constraint equations on semi-structured, multi-block three-dimensional domains.

In Section 10 we used semi-structured multi-block triangulations to solve for some test problems with known closed-form solutions. The obtained linear and quadratic finite element solutions were then restricted to the multi-block grid, and their convergence, as well as the convergence of their first and second derivatives, was evaluated numerically using independent high-order finite difference operators satisfying summation by parts (SBP). While the linear elements

solution showed usual 2-nd order convergence (unacceptably low for many relativistic applications), for quadratic elements we obtained superconvergence with order $3 + \sigma$ (with $0 < \sigma \leq 1$) on the grid, due to the approximate local symmetry at the mesh vertices with respect to the local inversion of the multi-block triangulations.

Initial data for a first-order formulation of the Einstein equations involves first derivatives of the solution of the constraints equation. Computing the constraints or right-hand sides of the evolution equations requires taking derivatives twice. In Section 10.4 we analyzed convergence of the first and second numerical derivatives, taken with different high-order SBP operators. For quadratic elements, the first numerical derivative was observed to converge with either the superconvergence order $3 + \sigma$, or the order of SBP operator. The latter is a transient error behavior and happens when the FE error is still smaller than the error of numerical differentiation.

In Section 10.5 we discussed three factors which make adaptive mesh refinement (AMR) unnecessary and/or less efficient for the problems here considered when compared to global refinement: the fact that the multi-block grid is already tailored to resolve fine features of the solution, the need to restrict the finite element solution to the same grid, and the superconvergence properties of the quadratic elements solution. Because we lose superconvergence when using completely unstructured meshes, adaptively refining the solution sometimes makes the errors *larger* (see Fig. 10.4 for an example). However, we also noted that AMR would likely become advantageous for other problems with more singular solution features.

Finally, in Chapter 11 we presented numerical experiments with Brill waves. The constraint equations in this case reduce to a single elliptic one (11.6) on the conformal factor ψ, which has to be differentiated once to obtain the full set of initial data variables in the generalized harmonic formulation (Section 11.1). Section 11.2 presented a convergence analysis of the initial data and Hamiltonian constraint, and confirmed that the initial data computed with quadratic finite elements shows the desired order of convergence > 3 (see table 11.1). Finally, in Chapter 12 we demonstrated stable, > 3-rd order convergent multi-block evolutions of subcritical Brill waves with finite differences, summation by parts operators, and extracted the first two dominant radiation modes from the numerical solution.

Our experiment with semistructured triangulations of multiblock grids have demonstrated

that the second-order FE initial data on such triangulations generates superconvergent evolution when evolved using high-order FD solver. Therefore, this approach is feasible for producing accurate and convergent initial data on multiblock grids. Future work in this direction will include testing this approach on full set of the Einstein constraints equations and producing more physically motivated 3D initial data.

References

[1] A. Einstein, Die Feldgleichungen der Gravitation, Sitzungsberichte der Königlich Preußischen Akademie der Wissenschaften (Berlin), Seite 844-847. (1915) 844–847.

[2] A. Einstein, Zur allgemeinen Relativitätstheorie, Sitzungsberichte der Königlich Preußischen Akademie der Wissenschaften (Berlin), Seite 778-786. (1915) 778–786.

[3] R. A. Hulse, J. H. Taylor, Discovery of a pulsar in a binary system, ApJ195 (1975) L51–L53.

[4] LIGO: Laser Interferometer Gravitational Wave Observatory.
URL http://www.ligo.caltech.edu/

[5] VIRGO.
URL http://www.virgo.infn.it/

[6] GEO 600.
URL http://www.geo600.uni-hannover.de/

[7] TAMA.
URL http://tamago.mtk.nao.ac.jp/

[8] B. F. S. B.S. Sathyaprakash, Physics, astrophysics and cosmology with gravitational waves, Living Reviews in Relativity 12 (2).
URL http://www.livingreviews.org/lrr-2009-2

[9] Advanced LIGO.
URL http://www.ligo.caltech.edu/advLIGO/

[10] F. Acernese, et al., The Virgo status, Class. Quant. Grav. 23 (2006) S635–S642.

[11] K. Danzmann, A. Rüdiger, LISA technology – Concept, status, prospects, Class. Quantum Grav. 20 (2003) S1–S9.
URL stacks.iop.org/CQG/20/S2

[12] ET: Einstein Telescope.
URL http://www.et-gw.eu/

[13] M. Hannam, I. Hawke, Numerical relativity simulations in the era of the Einstein Telescope.

[14] K. Menou, E. Quataert, R. Narayan, Astrophysical Evidence for Black Hole Event Horizons, ArXiv Astrophysics e-prints.

[15] J. Magorrian, S. Tremaine, D. Richstone, R. Bender, G. Bower, A. Dressler, S. M. Faber, K. Gebhardt, R. Green, C. Grillmair, J. Kormendy, T. Lauer, The Demography of Massive Dark Objects in Galaxy Centers, AJ115 (1998) 2285–2305.

[16] M. R. Garcia, J. E. McClintock, R. Narayan, P. Callanan, D. Barret, S. S. Murray, New Evidence for Black Hole Event Horizons from Chandra, ApJ553 (2001) L47–L50.

[17] S. Komossa, Observational evidence for supermassive black hole binaries, in: J. M. Centrella (Ed.), The Astrophysics of Gravitational Wave Sources, Vol. 686 of American Institute of Physics Conference Series, 2003, pp. 161–174.

[18] P. Mészáros, Gamma-ray bursts, Rep. Prog. Phys. 69 (2006) 2259–2321.

[19] T. Piran, Y. Fan, Gamma-ray burst theory after Swift, Royal Society of London Philosophical Transactions Series A 365 (2007) 1151–1162.

[20] N. Gehrels, E. Ramirez-Ruiz, D. B. Fox, Gamma-Ray Bursts in the Swift Era, ARA&A47 (2009) 567–617.

[21] M. Ruffert, H.-T. Janka, Gamma-ray bursts from accreting black holes in neutron star mergers, Astron. Astrophys. 344 (1999) 537.

[22] S. E. Woosley, J. S. Bloom, The supernova gamma-ray burst connection, Annual Rev. Astron. Astrophys. 44 (2006) 507–556.

[23] V. V. Usov, Millisecond pulsars with extremely strong magnetic fields as a cosmological source of gamma-ray bursts, Nature357 (1992) 472–474.

[24] J. C. B. Papaloizou, J. E. Pringle, The dynamical stability of differentially rotating discs with constant specific angular momentum, MNRAS208 (1984) 721–750.

[25] J. C. B. Papaloizou, J. E. Pringle, The dynamical stability of differentially rotating discs. II, MNRAS213 (1985) 799–820.

[26] P. Goldreich, J. Goodman, R. Narayan, The stability of accretion tori. I - Long-wavelength modes of slender tori, MNRAS221 (1986) 339–364.

[27] Y. Kojima, The Dynamical Stability of a Fat Disk with Constant Specific Angular Momentum, Progress of Theoretical Physics 75 (1986) 251–261.

[28] Y. Kojima, The Dynamical Stability of Tori around a Schwarzschild Black Hole, Progress of Theoretical Physics 75 (1986) 1464–1467.

[29] R. Narayan, P. Goldreich, J. Goodman, Physics of modes in a differentially rotating system - Analysis of the shearing sheet, MNRAS228 (1987) 1–41.

[30] J. Goodman, R. Narayan, The stability of accretion tori. III - The effect of self-gravity, MNRAS231 (1988) 97–114.

[31] D. M. Christodoulou, R. Narayan, The stability of accretion tori. IV - Fission and fragmentation of slender, self-gravitating annuli, ApJ388 (1992) 451–466.

[32] D. M. Christodoulou, The stability of accretion tori. V - Unstable modes and avoided crossings in extended, self-gravitating annuli, ApJ412 (1993) 696–719.

[33] M. A. Abramowicz, M. Calvani, L. Nobili, Runaway instability in accretion disks orbiting black holes, in: B. Bertotti, F. de Felice, A. Pascolini (Eds.), General Relativity and Gravitation, Volume 1, 1983, pp. 677–+.

[34] S. Nishida, Y. Eriguchi, Runaway Instability of Black Hole–Neutron Torus Systems, ApJ461 (1996) 320–+.

[35] F. Daigne, R. Mochkovitch, Gamma-ray bursts and the runaway instability of thick discs around black holes, MNRAS285 (1997) L15–L19.

[36] N. Masuda, Y. Eriguchi, Three-dimensional Simulations of Runaway Instability of Self-gravitating Accretion Disks, ApJ489 (1997) 804–+.

[37] M. A. Abramowicz, V. Karas, A. Lanza, On the runaway instability of relativistic tori, A&A331 (1998) 1143–1146.

[38] N. Masuda, S. Nishida, Y. Eriguchi, The runaway instability of self-gravitating tori with non-constant specific angular momentum around black holes, MNRAS297 (1998) 1139–1144.

[39] J. A. Font, F. Daigne, The runaway instability of thick discs around black holes - I. The constant angular momentum case, MNRAS334 (2002) 383–400.

[40] O. Zanotti, L. Rezzolla, Dynamics of Oscillating Relativistic Tori, Memorie della Societa Astronomica Italiana Supplement 1 (2003) 192–+.

[41] O. Zanotti, L. Rezzolla, J. A. Font, Quasi-periodic accretion and gravitational waves from oscillating 'toroidal neutron stars' around a Schwarzschild black hole, MNRAS341 (2003) 832–848.

[42] F. Daigne, J. A. Font, The runaway instability of thick discs around black holes - II. Non-constant angular momentum discs, MNRAS349 (2004) 841–868.

[43] P. J. Montero, J. A. Font, M. Shibata, Influence of Self-Gravity on the Runaway Instability of Black-Hole-Torus Systems, Physical Review Letters 104 (19) (2010) 191101–+.

[44] M. Holst, Adaptive numerical treatment of elliptic systems on manifolds, Advances in Computational Mathematics 15 (2001) 139–191.
URL `citeseer.ist.psu.edu/holst01adaptive.html`

[45] Cactus Computational Toolkit, `http://www.cactuscode.org`.

[46] E. Schnetter, S. H. Hawley, I. Hawke, Evolutions in 3D numerical relativity using fixed mesh refinement, Classical and Quantum Gravity 21 (2004) 1465–1488.

[47] Adaptive mesh refinement with Carpet, `http://www.carpetcode.org/`.

[48] E. Schnetter, P. Diener, E. N. Dorband, M. Tiglio, A multi-block infrastructure for three-dimensional time- dependent numerical relativity, Class. Quant. Grav. 23 (2006) S553–S578.

[49] B. Zink, E. Schnetter, M. Tiglio, Multipatch methods in general relativistic astrophysics: Hydrodynamical flows on fixed backgrounds, Phys. Rev. D77 (10) (2008) 103015–+.

[50] E. Pazos, E. N. Dorband, A. Nagar, C. Palenzuela, E. Schnetter, M. Tiglio, How far away is far enough for extracting numerical waveforms, and how much do they depend on the extraction method?, Classical and Quantum Gravity 24 (2007) 341–+.

[51] L. Lindblom, M. A. Scheel, L. E. Kidder, R. Owen, O. Rinne, A new generalized harmonic evolution system, Classical and Quantum Gravity 23 (2006) 447–+.

[52] R. M. Wald, General relativity, The University of Chicago Press, Chicago, 1984.

[53] J. Thornburg, Coordinates and boundary conditions for the general relativistic initial data problem, Class. Quantum Grav. 4 (5) (1987) 1119–1131.
URL `http://stacks.iop.org/0264-9381/4/1119`

[54] J. Thornburg, Numerical relativity in black hole spacetimes, Ph.D. thesis, University of British Columbia, Vancouver, British Columbia (1993).

[55] R. Gómez, L. Lehner, R. Marsa, J. Winicour, Moving black holes in 3D, Phys. Rev. D 57 (8) (1998) 4778–4788.

[56] R. Gómez, R. L. Marsa, J. Winicour, Black hole excision with matching, Phys. Rev. D 56 (1997) 6310–6319, gr-qc/9708002.

[57] R. Gómez, L. Lehner, R. Marsa, J. Winicour, A. M. Abrahams, A. Anderson, P. Anninos, T. W. Baumgarte, N. T. Bishop, S. R. Brandt, J. C. Browne, K. Camarda, M. W. Choptuik, G. B. Cook, R. Correll, C. R. Evans, L. S. Finn, G. C. Fox, T. Haupt, M. F. Huq, L. E. Kidder, S. A. Klasky, P. Laguna, W. Landry, J. Lenaghan, J. Masso, R. A. Matzner, S. Mitra, P. Papadopoulos, M. Parashar, L. Rezzolla, M. E. Rupright, F. Saied, P. E. Saylor, M. A. Scheel, E. Seidel, S. L. Shapiro, D. Shoemaker, L. Smarr, B. Szilágyi, S. A. Teukolsky, M. H. P. M. van Putten, P. Walker, J. W. York Jr, Stable characteristic evolution of generic three-dimensional single-black-hole spacetimes, Phys. Rev. Lett. 80 (1998) 3915–3918.

[58] S. Bonazzola, E. Gourgoulhon, J.-A. Marck, Evolutionary sequences of irrotational binary neutron stars, Proceedings of the 19th Texas SymposiumGr-qc/9904040.

[59] L. E. Kidder, M. A. Scheel, S. A. Teukolsky, Extending the lifetime of 3D black hole computations with a new hyperbolic system of evolution equations, Phys. Rev. D 64 (2001) 064017.

[60] E. Gourgoulhon, P. Grandclément, K. Taniguchi, J. Marck, S. Bonazzola, Quasiequilibrium sequences of synchronized and irrotational binary neutron stars in general relativity: Method and tests, Phys. Rev. D 63 (2001) 064029.

[61] P. Grandclément, S. Bonazzola, E. Gourgoulhon, J.-A. Marck, A multi-domain spectral method for scalar and vectorial Poisson equations with non-compact sources, J. Comput. Phys. 170 (2001) 231–260.

[62] H. P. Pfeiffer, L. E. Kidder, M. A. Scheel, S. A. Teukolsky, A multidomain spectral method for solving elliptic equations, Computer Physics Communications 152 (2003) 253–273.

[63] J. Thornburg, Black hole excision with multiple grid patches, Class. Quantum Grav. 21 (15) (2004) 3665–3691.

[64] G. Calabrese, D. Neilsen, Excising a boosted rotating black hole with overlapping grids, Phys. Rev. D 71 (2005) 124027.

[65] M. A. Scheel, H. P. Pfeiffer, L. Lindblom, L. E. Kidder, O. Rinne, S. A. Teukolsky, Solving Einstein's equations with dual coordinate frames, Phys. Rev. D 74 (2006) 104006.

[66] H. P. Pfeiffer, D. Brown, L. E. Kidder, L. Lindblom, G. Lovelance, M. A. Scheel, Reducing orbital eccentricity in binary black hole simulations, Class. Quantum Grav. 24 (2007) S59–S81.

[67] F. Foucart, L. E. Kidder, H. P. Pfeiffer, S. A. Teukolsky, Initial data for black hole neutron star binaries: A flexible, high-accuracy spectral method, Phys. Rev. D77 (12) (2008) 124051–+.

[68] M. D. Duez, F. Foucart, L. E. Kidder, H. P. Pfeiffer, M. A. Scheel, S. A. Teukolsky, Evolving black hole-neutron star binaries in general relativity using pseudospectral and finite difference methods, Phys. Rev. D78 (10) (2008) 104015–+.

[69] E. Pazos, M. Tiglio, M. D. Duez, L. E. Kidder, S. A. Teukolsky, Orbiting binary black hole evolutions with a multipatch high order finite-difference approach, Phys. Rev. D80 (2) (2009) 024027–+.

[70] P. C. Fragile, C. C. Lindner, P. Anninos, J. D. Salmonson, Application of the Cubed-Sphere Grid to Tilted Black Hole Accretion Disks, ApJ691 (2009) 482–494.

[71] M. A. Scheel, M. Boyle, T. Chu, L. E. Kidder, K. D. Matthews, H. P. Pfeiffer, High-accuracy waveforms for binary black hole inspiral, merger, and ringdown, Phys. Rev. D79 (2) (2009) 024003–+.

[72] M. D. Duez, F. Foucart, L. E. Kidder, C. D. Ott, S. A. Teukolsky, Equation of state effects in black hole-neutron star mergers, Classical and Quantum Gravity 27 (11) (2010) 114106–+.

[73] G. Calabrese, D. Neilsen, Spherical excision for moving black holes and summation by parts for axisymmetric systems, Phys. Rev. D 69 (2004) 044020.

[74] B. Szilágyi, D. Pollney, L. Rezzolla, J. Thornburg, J. Winicour, An explicit harmonic code for black-hole evolution using excision, Class. Quantum Grav. 24 (2007) S275–S293.

[75] C. Ronchi, The "Cubed Sphere": A New Method for the Solution of Partial Differential Equations in Spherical Geometry, Journal of Computational Physics 124 (1996) 93–114.

[76] P. Diener, E. N. Dorband, E. Schnetter, M. Tiglio, New, efficient, and accurate high order derivative and dissipation operators satisfying summation by parts, and applications in three-dimensional multi-block evolutions, Journal of Scientific Computing 32 (2007) 109. URL doi:10.1007/s10915-006-9123-7

[77] B. Gustafsson, On the implementation of boundary conditions for the method of lines, BIT Numerical Mathematics 38 (2) (1998) 293–314.

[78] L. D. Landau, E. M. Lifshitz, The Classical Theory of Fields, Course of Theoretical Physics, Volume 2, Elsevier Butterworth-Heinemann, Oxford, 2004.

[79] J. R. Wilson, Numerical study of fluid flow in a kerr space, Astrophys. J. 173 (1972) 431.

[80] J. A. Font, Numerical hydrodynamics in general relativity, Living Reviews in Relativity 6 (4).
URL http://www.livingreviews.org/lrr-2003-4

[81] C. F. Gammie, J. C. McKinney, G. Tóth, Harm: A numerical scheme for general relativistic magnetohydrodynamics, Astrophys. J. 589 (2003) 458.

[82] J. W. Woodward, J. E. Tohline, I. Hachisu, The stability of thick, self-gravitating disks in protostellar systems, ApJ420 (1994) 247–267.

[83] A. Harten, P. Lax, B. van Leer, On upstream differencing and godunov-type schemes for hyperbolic conservation laws, SIAM Rev. 25 (1983) 35–61.

[84] S. C. Noble, C. F. Gammie, J. C. McKinney, L. Del Zanna, Primitive Variable Solvers for Conservative General Relativistic Magnetohydrodynamics, ApJ641 (2006) 626–637.

[85] L. Lindblom, B. Szilágyi, Improved gauge driver for the generalized harmonic Einstein system, Phys. Rev. D80 (8) (2009) 084019–+.

[86] P. Secchi, The initial-boundary value problem for linear symmetric hyperbolic systems with characteristic boundary of constant multiplicity, Differential Integral Equations 9 (4) (1996) 671–700.

[87] P. Secchi, Well-posedness of characteristic symmetric hyperbolic systems, Arch. Rational Mech. Anal. 134 (2) (1996) 155–197.
URL http://dx.doi.org/10.1007/BF00379552

[88] J. Rauch, Symmetric positive systems with boundary characteristic of constant multiplicity, Trans. Amer. Math. Soc. 291 (1) (1985) 167–187.
URL http://dx.doi.org/10.2307/1999902

[89] T. P. Liu, Development of singularities in the nonlinear waves for quasilinear hyperbolic partial differential equations, "J. Differential Equations" 33 (1) (1979) 92–111.

[90] B. Gustafsson, H.-O. Kreiss, J. Oliger, Time dependent problems and difference methods, Wiley, New York, 1995.

[91] L. Lehner, O. Reula, M. Tiglio, Multi-block simulations in general relativity: high order discretizations, numerical stability, and applications, Classical and Quantum Gravity 22 (2005) 5283.
URL http://www.citebase.org/abstract?id=oai:arXiv.org:gr-qc/0507004

[92] D. W. Neilsen, M. W. Choptuik, Ultrarelativistic fluid dynamics, Classical and Quantum Gravity 17 (2000) 733–759.

[93] J. A. Font, H. Dimmelmeier, A. Gupta, N. Stergioulas, Axisymmetric modes of rotating relativistic stars in the Cowling approximation, Mon. Not. R. Astron. Soc.In press, astro-ph/0012477.

[94] P. J. Montero, J. A. Font, M. Shibata, Nada: A new code for studying self-gravitating tori around black holes, ArXiv e-prints 805.

[95] M. Abramowicz, M. Jaroszynski, M. Sikora, Relativistic, accreting disks, A&A63 (1978) 221–224.

[96] G. Calabrese, L. Lehner, O. Reula, O. Sarbach, M. Tiglio, Summation by parts and dissipation for domains with excised regions, Class. Quantum Grav. 21 (2004) 5735–5758.

[97] N. Stergioulas, J. L. Friedman, Comparing models of rapidly rotating relativistic stars constructed by two numerical methods, ApJ444 (1995) 306–311.

[98] H. Komatsu, Y. Eriguchi, I. Hachisu, Rapidly rotating general relativistic stars. I - Numerical method and its application to uniformly rotating polytropes, MNRAS237 (1989) 355–379.

[99] J. A. Font, N. Stergioulas, K. D. Kokkotas, Nonlinear hydrodynamical evolution of rotating relativistic stars: Numerical methods and code tests, Mon. Not. R. Astron. Soc. 313 (2000) 678.

[100] J. A. Font, T. Goodale, S. Iyer, M. Miller, L. Rezzolla, E. Seidel, N. Stergioulas, W. M. Suen, M. Tobias, Three-dimensional general relativistic hydrodynamics. II. Long-term dynamics of single relativistic stars, Phys. Rev. D 65 (2002) 084024.

[101] H. Dimmelmeier, N. Stergioulas, J. A. Font, Non-linear axisymmetric pulsations of rotating relativistic stars in the conformal flatness approximation, MNRAS368 (2006) 1609–1630.

[102] S. E. Woosley, Gamma-ray bursts from stellar mass accretion disks around black holes, ApJ405 (1993) 273–277.

[103] M. Ruffert, H.-T. Janka, G. Schäfer, Coalescing neutron stars – a step towards physical models. i. hydrodynamic evolution and gravitational-wave emission, Astron. Astrophys. 311 (1996) 532.

[104] M. D. Duez, Numerical relativity confronts compact neutron star binaries: a review and status report, ArXiv e-prints.

[105] R. Meinel, M. Ansorg, A. Kleinwächter, G. Neugebauer, D. Petroff, Relativistic Figures of Equilibrium, 2008.

[106] M. Ansorg, T. Fischer, A. Kleinwächter, R. Meinel, D. Petroff, K. Schöbel, Equilibrium configurations of homogeneous fluids in general relativity, MNRAS355 (2004) 682–688.

[107] Y. Eriguchi, D. Sugimoto, Another Equilibrium Sequence of Self-Gravitating and Rotating Incompressible Fluid, Progress of Theoretical Physics 65 (1981) 1870–1875.

[108] Y. Eriguchi, I. Hachisu, Bifurcation points on the one-ring sequence of uniformly rotating and self-gravitating fluid, PASJ36 (1984) 491–496.

[109] T. Piran, The physics of gamma-ray bursts, Reviews of Modern Physics 76 (2004) 1143–1210.

[110] W. H. Lee, E. Ramirez-Ruiz, The progenitors of short gamma-ray bursts, New Journal of Physics 9 (2007) 17–+.

[111] P. Meszaros, M. J. Rees, High-entropy fireballs and jets in gamma-ray burst sources, MNRAS257 (1992) 29P–31P.

[112] R. D. Blandford, R. L. Znajek, Electromagnetic extraction of energy from Kerr black holes, MNRAS179 (1977) 433–456.

[113] B. D. Metzger, Gamma-Ray Burst Central Engines: Black Hole Vs. Magnetar, ArXiv e-prints.

[114] J. Frank, A. King, D. J. Raine, Accretion Power in Astrophysics: Third Edition, 2002.

[115] L. Rezzolla, L. Baiotti, B. Giacomazzo, D. Link, J. A. Font, Accurate evolutions of unequal-mass neutron-star binaries: properties of the torus and short GRB engines, ArXiv e-prints.

[116] M. Shibata, K. Kyutoku, T. Yamamoto, K. Taniguchi, Gravitational waves from black hole-neutron star binaries: Classification of waveforms, Phys. Rev. D79 (4) (2009) 044030–+.

[117] A. I. MacFadyen, S. E. Woosley, A. Heger, Supernovae, Jets, and Collapsars, Astrophys. J. 550 (2001) 410–425.

[118] S. E. Woosley, A. Heger, T. A. Weaver, The evolution and explosion of massive stars, Rev. Mod. Phys. 74 (2002) 1015.

[119] M. J. Rees, P. Meszaros, Relativistic fireballs - Energy conversion and time-scales, MNRAS258 (1992) 41P–43P.

[120] J. Goodman, A. Dar, S. Nussinov, Neutrino annihilation in Type II supernovae, ApJ314 (1987) L7–L10.

[121] M. Jaroszynski, Neutrino emission and annihilation near tori around black holes, Acta Astronomica 43 (1993) 183–191.

[122] S. Kobayashi, B. Zhang, P. Mészáros, D. Burrows, Inverse Compton X-Ray Flare from Gamma-Ray Burst Reverse Shock, ApJ655 (2007) 391–395.

[123] E. Nakar, T. Piran, Modeling Fluctuations in Gamma-Ray Burst Afterglow Light Curves, ApJ598 (2003) 400–410.

[124] B. Zhang, Y. Z. Fan, J. Dyks, S. Kobayashi, P. Mészáros, D. N. Burrows, J. A. Nousek, N. Gehrels, Physical Processes Shaping Gamma-Ray Burst X-Ray Afterglow Light Curves: Theoretical Implications from the Swift X-Ray Telescope Observations, ApJ642 (2006) 354–370.

[125] M. A. Abramowicz, M. Calvani, L. Nobili, Runaway instability in accretion disks orbiting black holes, Nature302 (1983) 597–599.

[126] J. A. Font, F. Daigne, The runaway instability of thick discs around black holes – I. the constant angular momentum case, Mon. Not. R. Astron. Soc. 334 (2002) 383–400.

[127] B. Paczynsky, P. J. Wiita, Thick accretion disks and supercritical luminosities, Astron. Astrophys. 88 (1980) 23–31.

[128] D. B. Wilson, A runaway instability in thick accretion disks?, Nature312 (1984) 620–+.

[129] J. A. Font, F. Daigne, On the stability of thick accretion disks around black holes, Astrophys.J 581 (2002) L23–L26.

[130] R. Khanna, S. K. Chakrabarti, Effects of a self-gravitating disc on test particle motion around a Kerr black hole, MNRAS259 (1992) 1–5.

[131] S. Nishida, A. Lanza, Y. Eriguchi, M. A. Abramowicz, Runaway instability and gamma-ray bursts, MNRAS278 (1996) L41–L45.

[132] V. S. Safronov, On the gravitational instability in flattened systems with axial symmetry and non-uniform rotation, Annales d'Astrophysique 23 (1960) 979–+.

[133] A. Toomre, On the gravitational stability of a disk of stars, ApJ139 (1964) 1217–1238.

[134] C. F. Gammie, Nonlinear Outcome of Gravitational Instability in Cooling, Gaseous Disks, ApJ553 (2001) 174–183.

[135] O. M. Blaes, W. Glatzel, On the stability of incompressible constant angular momentum cylinders, MNRAS220 (1986) 253–258.

[136] J. Frank, J. A. Robertson, Numerical studies of the dynamical stability of differentially rotating tori, MNRAS232 (1988) 1–33.

[137] W. H. Zurek, W. Benz, Redistribution of angular momentum by nonaxisymmetric instabilities in a thick accretion disk, ApJ308 (1986) 123–133.

[138] O. M. Blaes, Stabilization of non-axisymmetric instabilities in a rotating flow by accretion on to a central black hole, MNRAS227 (1987) 975–992.

[139] O. M. Blaes, J. F. Hawley, Nonaxisymmetric disk instabilities - A linear and nonlinear synthesis, ApJ326 (1988) 277–291.

[140] F. C. Adams, S. P. Ruden, F. H. Shu, Eccentric gravitational instabilities in nearly Keplerian disks, ApJ347 (1989) 959–976.

[141] F. H. Shu, S. Tremaine, F. C. Adams, S. P. Ruden, Sling amplification and eccentric gravitational instabilities in gaseous disks, ApJ358 (1990) 495–514.

[142] M. H. M. Heemskerk, J. C. Papaloizou, G. J. Savonije, Non-linear development of M = 1 instabilities in a self-gravitating gaseous disc, A&A260 (1992) 161–174.

[143] S. W. Andalib, J. E. Tohline, D. M. Christodoulou, A Survey of the Principal Modes of Nonaxisymmetric Instability in Self-gravitating Accretion Disk Models, ApJS108 (1997) 471–+.

[144] P. A. Taylor, J. C. Miller, P. Podsiadlowski, Long duration gamma-ray bursts: hydrodynamic instabilities in collapsar disks, ArXiv e-prints.

[145] S. Nishida, Y. Eriguchi, A general relativistic toroid around a black hole, ApJ427 (1994) 429–437.

[146] M. Shibata, Rotating black hole surrounded by self-gravitating torus in the puncture framework, Phys. Rev. D76 (6) (2007) 064035–+.

[147] J. D. Brown, Puncture evolution of schwarzschild black holes (2007).
URL http://www.citebase.org/abstract?id=oai:arXiv.org:0705.1359

[148] D. Brown, P. Diener, O. Sarbach, E. Schnetter, M. Tiglio, Turduckening black holes: an analytical and computational study, Phys. Rev. D79 (2009) 044023.

[149] H. A. Williams, J. E. Tohline, Linear and nonlinear dynamic instability of rotating polytropes, ApJ315 (1987) 594–601.

[150] C. W. Misner, K. S. Thorne, J. A. Wheeler, Gravitation, W. H. Freeman, San Francisco, 1973.

[151] E. Schnetter, Finding apparent horizons and other two-surfaces of constant expansion, Class. Quantum Grav. 20 (22) (2003) 4719–4737.
URL http://stacks.iop.org/0264-9381/20/4719

[152] A. T. Okazaki, S. Kato, J. Fukue, Global trapped oscillations of relativistic accretion disks, PASJ39 (1987) 457–473.

[153] L. Rezzolla, S. Yoshida, O. Zanotti, Oscillations of vertically integrated relativistic tori - I. Axisymmetric modes in a Schwarzschild space-time, MNRAS344 (2003) 978–992.

[154] T. Zwerger, E. Müller, Dynamics and gravitational wave signature of axisymmetric rotational core collapse., Astron. Astrophys. 320 (1997) 209.

[155] J. A. Font, T. Goodale, S. Iyer, M. Miller, L. Rezzolla, E. Seidel, N. Stergioulas, W.-M. Suen, M. Tobias, Three-dimensional general relativistic hydrodynamics. II. Long-term dynamics of single relativistic stars, Phys. Rev. D 65 (2002) 084024.

[156] L. Baiotti, I. Hawke, P. J. Montero, F. Löffler, L. Rezzolla, N. Stergioulas, J. A. Font, E. Seidel, Three-dimensional relativistic simulations of rotating neutron star collapse to a Kerr black hole, Phys. Rev. D 71 (2005) 024035.

[157] E. B. Abdikamalov, H. Dimmelmeier, L. Rezzolla, J. C. Miller, Relativistic simulations of the phase-transition-induced collapse of neutron stars, MNRAS392 (2009) 52–76.

[158] E. B. Abdikamalov, C. D. Ott, L. Rezzolla, L. Dessart, H. Dimmelmeier, A. Marek, H. Janka, Axisymmetric general relativistic simulations of the accretion-induced collapse of white dwarfs, Phys. Rev. D81 (4) (2010) 044012–+.

[159] L. Lehner, Numerical relativity: A review, Class. Quantum Grav. 18 (2001) R25–R86.

[160] F. Pretorius, Evolution of binary black hole spacetimes, Phys. Rev. Lett. 95 (2005) 121101.

[161] S. Bonazzola, J. Frieben, E. Gourgoulhon, J.-A. Marck, Spectral methods in general relativity – v toward the simulation of 3D-gravitational collapse of neutron stars, in: Proceedings of the Third International Conference on Spectral and High Order Methods, Houston Journal of Mathematics (1996), University of Houston, 1996.

[162] J. N. Philippe Grandclément, Spectral methods for numerical relativity, Living Reviews in Relativity 12 (1) (2009) 1–+.
URL http://www.livingreviews.org/lrr-2009-1

[163] G. B. Cook, Initial data for numerical relativity, Living Rev. Relativity 3 (2000) 5.
URL http://www.livingreviews.org/lrr-2000-5

[164] H. P. Pfeiffer, S. A. Teukolsky, G. B. Cook, Quasi-circular orbits for spinning binary black holes, Phys. Rev. D 62 (2000) 104018.

[165] L. E. Kidder, L. S. Finn, Spectral methods for numerical relativity. the initial data problem, Phys. Rev. D 62 (2000) 084026.

[166] H. Pfeiffer, Initial data for black hole evolutions, Ph.D. thesis, Cornell University, Ithaca, New York State (2003).

[167] S. Bonazzola, E. Gourgoulhon, J.-A. Marck, Numerical approach for high precision 3-D relativistic star models, Phys. Rev. D. 58 (1998) 104020.

[168] L.-M. Lin, J. Novak, A new spectral apparent horizon finder for 3D numerical relativity, Class. Quant. Grav. 24 (2007) 2665–2676.

[169] T. Nakamura, Y. Kojima, K. Oohara, A method of determining apparent horizons in three-dimensional numerical relativity, Phys. Lett. A 106 (5-6) (1984) 235–238.

[170] E. Tadmor, Spectral methods for hyperbolic problems, in: Lecture notes delivered at Ecole des Ondes, "Méthodes numériques d'ordre élevé pour les ondes en régime transitoire", INRIA–Rocquencourt January 24-28., 1994.
URL http://www.cscamm.umd.edu/people/faculty/tadmor/pub/spectral-approximations/Tadmor.INRIA-94.pdf

[171] L. E. Kidder, M. A. Scheel, S. A. Teukolsky, E. D. Carlson, G. B. Cook, Black hole evolution by spectral methods, Phys. Rev. D 62 (2000) 084032.

[172] L. Kidder, M. Scheel, S. Teukolsky, G. Cook, Spectral evolution of Einstein's equations, in: Miniprogram on Colliding Black Holes: Mathematical Issues in Numerical Relativity, Institute for Theoretical Physics, UCSB, Santa Barbara, CA, 2000.

[173] M. A. Scheel, L. E. Kidder, L. Lindblom, H. P. Pfeiffer, S. A. Teukolsky, Toward stable 3d numerical evolutions of black-hole spacetimes, Phys. Rev. D 66 (2002) 124005.

[174] J. M. Martí, E. Müller, Numerical hydrodynamics in special relativity, Living Rev. Relativity 2 (1999) 3.
URL http://www.livingreviews.org/lrr-1999-3

[175] M. D. Duez, L. E. Kidder, S. A. Teukolsky, Evolving relativistic fluid spacetimes using pseudospectral methods and finite differencing (2007).
URL http://www.citebase.org/abstract?id=oai:arXiv.org:gr-qc/0702126

[176] J. Isenberg, Constant mean curvature solution of the Einstein constraint equations on closed manifold, Class. Quantum Grav. 12 (1995) 2249–2274.

[177] J. Isenberg, V. Moncrief, A set of nonconstant mean curvature solution of the Einstein constraint equations on closed manifolds, Class. Quantum Grav. 13 (1996) 1819–1847.

[178] M. Holst, J. Kommemi, G. Nagy, Rough solutions of the Einstein constraint equations with nonconstant mean curvature, submitted to Comm. Math. Phys. Available as arXiv:0708.3410v2 [gr-qc].

[179] M. Holst, G. Nagy, G. Tsogtgerel, Rough solutions of the Einstein constraints on closed manifolds without near-CMC conditions, submitted for publication. Available as arXiv:0712.0798v1 [gr-qc].

[180] M. Holst, G. Nagy, G. Tsogtgerel, Far-from-constant mean curvature solutions of Einstein's constraint equations with positive Yamabe metrics, submitted to Phys. Rev. Lett.

[181] M. Holst, G. Tsogtgerel, Adaptive finite element approximation of nonlinear geometric PDE, preprint.

[182] M. Holst, G. Tsogtgerel, Convergent adaptive finite element approximation of the Einstein constraints, preprint.

[183] L. Wahlbin, Superconvergence in Galerkin Finite Element Methods, Springer-Verlag New York, 1995.

[184] R. Bank, M. Holst, A new paradigm for parallel adaptive mesh refinement, SIAM Rev. 45 (2) (2003) 291–323.

[185] M. Holst, The finite element toolkit (FeTK), Website, `http://www.fetk.org`.

[186] B. Aksoylu, D. Bernstein, S. Bond, M. Holst, Generating initial data in general relativity using adaptive finite element methods, in preparation.

[187] B. Aksoylu, M. Holst, Optimality of multilevel preconditioners for local mesh refinement in three dimensions, SIAM J. Numer. Anal. 44 (3) (2006) 1005–1025.

[188] B. Aksoylu, S. Bond, M. Holst, An odyssey into local refinement and multilevel preconditioning III: Implementation and numerical experiments, SIAM J. Sci. Comput. 25 (2) (2003) 478–498.

[189] L. Chen, M. Holst, J. Xu, Convergence and optimality of adaptive mixed finite element methods, submitted to Math. Comp.

[190] L. Chen, M. Holst, J. Xu, The finite element approximation of the nonlinear Poisson-Boltzmann Equation, SIAM J. Numer. Anal. 45 (6) (2007) 2298–2320.

[191] R. A. Adams, Sobolev Spaces, Academic Press, Inc., 1987.

[192] M. S. Gockenbach, Understanding and Implementing the Finite Element Method, SIAM, 2006.

[193] P.-L. George, H. Borouchaki, Delauney Triangulation and Meshing: Application to Finite Elements, Kogan Page, 1998.

[194] C.-M. Chen, Superconvergence of Finite Element Solutions and Their Derivatives, Hunan Science Press, 1982, (in Chinese).

[195] Q.-D. Zhu, Q. Lin, Hyperconvergence Theory of Finite Elements, Hunan Science and Technology Publishing House, Changsha, P.R. China, 1989, (in Chinese).

[196] M. Křížek, P. Neittaanmäki, On a global superconvergence of the gradient of linear triangular elements, J. Comput. Appl. Math. 18 (2) (1987) 221–233.

[197] A. H. Schatz, I. H. Sloan, L. B. Wahlbin, Superconvergence in finite element methods and meshes that are locally symmetric with respect to a point, SIAM Journal on Numerical Analysis 33 (2) (1996) 505–521.
URL http://link.aip.org/link/?SNA/33/505/1

[198] A. H. Schatz, Pointwise error estimates, superconvergence and extrapolation (1998) 237–247.

[199] J. F. Sallee, The middle-cut triangulations of the n-cube 5 (3) (1984) 407–419.

[200] H. W. Kuhn, Some combinatorial lemmas in topology, IBM Journal of Research and Development 4 (1960) 508–524.

[201] C. Min, Simplicial isosurfacing in arbitrary dimension and codimension, Journal of Computational Physics 190 (1) (2003) 295–310.

[202] D. Braess, Finite Elements: Theory, Fast Solvers, and Applications in Solid Mechanics, Cambridge University Press, 2007.

[203] S. Brenner, L. Scott, The Mathematical Theory of Finite Element Methods, Springer – Verlag, 2003.

[204] A. Ern, J. Guermond, Theory and practice of finite elements, Springer, 2004.

[205] N. D. Levine, Superconvergent recovery of the gradient from piecewise linear finite element approximations, IMA Journal of Numerical Analysis 5 (1985) 407–427.

[206] G. Goodsell, J. Whiteman, A unified treatment of superconvergent recovered gradient functions for piecewise linear finite element approximations, International Journal of Numerical Methods in Engineering 27 (1989) 469–481.

[207] Q. L. H. Blum, R. Rannacher, Asymptotic error expansion and richardson extrapolation for linear finite elements, Numer. Math. 49 (1986) 11–37.

[208] R. Arnowitt, S. Deser, C. W. Misner, The dynamics of general relativity, in: L. Witten (Ed.), Gravitation: An introduction to current research, John Wiley, New York, 1962, pp. 227–265.

[209] D. R. Brill, On the positive definite mass of the bondi-weber-wheeler time-symmetric gravitational waves, Ann. Phys. 7 (1959) 466–483.

[210] N. Ó Murchadha, Brill Waves, in: B. L. Hu, T. A. Jacobson (Eds.), Directions in General Relativity: Papers in Honor of Dieter Brill, Volume 2, 1993, pp. 210–+.

[211] M. Alcubierre, G. Allen, B. Bruegmann, G. Lanfermann, E. Seidel, W.-M. Suen, M. Tobias, Gravitational collapse of gravitational waves in 3d numerical relativity, Physical Review D 61 (2000) 041501.
URL http://www.citebase.org/abstract?id=oai:arXiv.org:gr-qc/9904013

[212] E. Pazos, Numerical studies on new techniques for gravitational wave extraction and binary black hole simulations, Ph.D. thesis, University of Maryland, College Park (2009).

[213] T. Regge, J. Wheeler, Stability of a Schwarzschild singularity, Phys. Rev. 108 (4) (1957) 1063–1069.

[214] F. J. Zerilli, Effective potential for even-parity Regge-Wheeler gravitational perturbation equations, Phys. Rev. Lett. 24 (13) (1970) 737–738.

[215] F. J. Zerilli, Tensor harmonics in canonical form for gravitational radiation and other applications, J. Math. Phys. 11 (1970) 2203–2208.

[216] K. Thorne, Multipole expansions of gravitational radiation, Rev. Mod. Phys. 52 (2) (1980) 299.

[217] S. Brandt, E. Seidel, The evolution of distorted rotating black holes III: Initial data, Phys. Rev. D 54 (2) (1996) 1403–1416.

[218] R. P. Kerr, A. Schild, Republication of: A new class of vacuum solutions of the Einstein field equations, General Relativity and Gravitation 41 (2009) 2485–2499.

[219] R. Takahashi, Horizon-penetrating transonic accretion discs around rotating black holes, MNRAS382 (2007) 567–593.

[220] O. Korobkin, B. Aksoylu, M. Holst, E. Pazos, M. Tiglio, Solving the Einstein constraint equations on multi-block triangulations using finite element methods, Class. Quant. Grav. 26 (2009) 145007.

Appendix A. Transforming Initial Data to Horizon-penetrating Coordinates

Here we present the transformation of the stationary axisymmetric initial data in quasi-isotropic coordinates to time-independent horizon-penetrating coordinates which is used in Chapter 4 in order to remove metric degeneracy at the BH horizon. In our initial data, the metric is given in general form (4.1) and represents an axisymmetric deformation of Schwarzschild BH by a massive equilibrium torus. The sought transformation has to satisfy the following requirements:

- metric in the new coordinates is time-independent;
- metric does not have pathologies (degeneracy or divergence) at the event horizon;
- 3-metric on $t = \text{const.}$ foliation is positive definite (i.e. the $t = \text{const.}$ foliation is spacelike).

We build our transformation by analogy with the transformation from isotropic Boyer-Lindquist coordinates [217] to horizon-penetrating Kerr-Schild coordinates [218] of Schwarzschild spacetime (see also [219] for a general case of rotating BH). In this case, the line element has the following form:

$$ds^2_{is} = -\left(\frac{1 - m/2r_*}{1 + m/2r_*}\right)^2 dt^2 + \psi^4 (dr^2_* + r^2_* d\Omega^2),$$

where m is the BH mass, r_* is the isotropic radius, $d\Omega^2 \equiv d\theta^2 + \sin\theta^2 d\varphi^2$ is the solid angle element, and $\psi \equiv 1 + \frac{m}{2r_*}$ is the conformal factor. At the event horizon $r_{*,h} = m/2$ the determinant of the isotropic metric is zero.

In the horizon-penetrating Kerr-Schild coordinates, the line element will be:

$$ds^2_{ks} = -(1 - H)d\bar{t}^2 + 2Hd\bar{t}dr + (1 + H)dr^2 + r^2 d\Omega^2$$

where $H \equiv 2m/r$ and $r \equiv r_* \left(1 + m/2r_*\right)^2$ is the Schwarzschild radial coordinate.

The Jacobian of transformation from the isotropic $(t, r_*, \theta, \varphi)$ to the horizon-penetrating coordinates $(\bar{t}, r, \theta, \varphi)$ has the following form:

$$\frac{D(t, r_*, \theta, \varphi)}{D(\bar{t}, r, \theta, \varphi)} = \begin{bmatrix} 1 & -\frac{H}{1-H} & 0 & 0 \\ 0 & \frac{r_*}{r\sqrt{1-H}} & 0 & 0 \\ 0 & 0 & 1 & 0 \\ 0 & 0 & 0 & 1 \end{bmatrix}.$$

Notice that at the event horizon the components of the transformation have to become infinite in order to compensate for the degeneracies in the isotropic metric.

The metric in the new coordinates remains independent of time, which is also true for an arbitrary transformation with the following Jacobian:

$$\frac{D(t, r_*, \theta, \varphi)}{D(\bar{t}, r, \theta, \varphi)} = \begin{bmatrix} 1 & f(r,\theta) & h(r,\theta) & 0 \\ 0 & g(r,\theta) & p(r,\theta) & 0 \\ 0 & 0 & 1 & 0 \\ 0 & 0 & 0 & 1 \end{bmatrix}, \qquad \text{(A1)}$$

where the functions $\{f, g, h, p\}$ do not explicitly depend on time and are only constrained by the regular Jacobian integrability conditions:

$$\frac{\partial f(r,\theta)}{\partial \theta} = \frac{\partial h(r,\theta)}{\partial r}, \qquad \frac{\partial g(r,\theta)}{\partial \theta} = \frac{\partial p(r,\theta)}{\partial r}.$$

For the case of a general axisymmetric spacetime, the metric in quasi-isotropic coordinates is given by:

$$\mathbf{g_{is}} \equiv \begin{bmatrix} g_{tt} & 0 & 0 & -\omega g_{\varphi\varphi} \\ 0 & e^{2\alpha} & 0 & 0 \\ 0 & 0 & r^2 e^{2\alpha} & 0 \\ -\omega g_{\varphi\varphi} & 0 & & g_{\varphi\varphi} \end{bmatrix}$$

where $g_{tt} \equiv -\lambda^2 + \omega^2 g_{\varphi\varphi}$ and $g_{\varphi\varphi} \equiv B^2\lambda^{-2} r_*^2 \sin\theta^2$. We can select the set of functions $\{f, g, h, p\}$ in the Jacobian (A1) above to construct a transformation from the quasi-isotropic to horizon-penetrating coordinates, which satisfies the above requirements for an arbitrary stationary axi-symmetric deformation of Schwarzschild if we choose:

$$f(r,\theta) = 1 - 1/\lambda^2(r,\theta), \quad g(r,\theta) = e^{-\alpha(r,\theta)}/\lambda(r,\theta).$$

Since the metric potentials $\lambda(r_*,\theta)$ and $\alpha(r_*,\theta)$ are known as functions of r_* and not r, we need to express the new radial coordinate r in terms of r_*. The required relations in the following differential form are obtained by inverting the Jacobian (A1):

$$\left(\frac{\partial r_*}{\partial r}\right)_{\theta=\text{const.}} = \frac{1}{g(r_*,\theta)}, \quad \left(\frac{\partial r_*}{\partial \theta}\right)_{r_*=\text{const.}} = 0.$$

These need to be integrated along the radial coordinate from $r_{*,h}$ to r_* for each θ:

$$r(r_*,\theta) - r_h = \int_{r_{*,h}}^{r_*} \frac{d\zeta}{g(\zeta,\theta)} = \int_{r_{*,h}}^{r_*} \lambda(\zeta,\theta) e^{\alpha(\zeta,\theta)} d\zeta.$$

where r_h is the radius of the event horizon in new coordinates. The remaining two unknown functions h and p can be calculated by 1D integration of the Jacobian integrability conditions:

$$\begin{aligned} h(r,\theta) &= \int_{r_h}^{r} dr' \frac{\partial f(r',\theta)}{\partial\theta} = 2\int_{r_{*,h}}^{r_*} \frac{\lambda'_\theta(\zeta,\theta) e^{\alpha(\zeta,\theta)}}{\lambda^2(\zeta,\theta)} d\zeta, \\ p(r,\theta) &= \int_{r_h}^{r} dr' \frac{\partial g(r',\theta)}{\partial\theta} \\ &= -\int_{r_{*,h}}^{r_*} \left(\alpha'_\theta(\zeta,\theta) + \frac{\lambda'_\theta(\zeta,\theta)}{\lambda(\zeta,\theta)}\right) d\zeta. \end{aligned}$$

After the transformation, the metric in the new horizon-penetrating coordinates has the following form:

$$\mathbf{g_{ks}} = \begin{bmatrix} g_{tt} & fg_{tt} & hg_{tt} & -\omega g_{\varphi\varphi} \\ \dots & e^{2\alpha}g^2 + g_{tt}f^2 & fhg_{tt} + e^{2\alpha}gp & -\omega f g_{\varphi\varphi} \\ \dots & \dots & h^2 g_{tt} + e^{2\alpha}(p^2 + r_*^2) & -\omega h g_{\varphi\varphi} \\ \dots & \dots & \dots & g_{\varphi\varphi} \end{bmatrix}$$

where ellipsis indicate matrix elements which can be filled in by symmetry. In the limit of $r \to r_h$, the functions f and g tend to infinity, while h and p vanish. The resulting metric at the horizon remains finite and non-degenerate:

$$\lim_{r\to r_h} \mathbf{g_{ks}} = \begin{bmatrix} 0 & 1 & 0 & 0 \\ 1 & 2 & C & 0 \\ 0 & C & e^{2\alpha}r_*^2 & 0 \\ 0 & 0 & 0 & g_{\varphi\varphi} \end{bmatrix}$$

where $C \equiv \lim_{r\to r_h} [fhg_{tt} + e^{2\alpha}gp]$ is a finite constant.

Appendix B. Permission to Include Authored Article in a Thesis

The second part of this thesis reproduces our article [220] in the *Classical and Quantum Gravity* journal, which is publishing in the IOP PUBLISHING, the publishing arm of the Institute of Physics (`http://iopscience.iop.org/`). Below we reproduce Clause 3 from the "Assignment of Copyright", with which authors become familiar when submitting their articles to any of the IOP journals. This document sets out the rights that IOP authors retain. Clause 3.2.2 explicitly states that the Named Authors retain the rights to include the Article in a research thesis.

3. Author Rights

   3.1. IOP grants the Named Authors the rights specified in 3.2 and 3.3. All such rights must be exercised for non-commercial purposes, if possible should display citation information and IOP's copyright notice, and for electronic use best efforts must be made to include a link to the on-line abstract in the Journal. Exercise of the rights in 3.3 additionally must not use the final published IOP format but the Named Author's own format (which may include amendments made following peer review).

   3.2. The rights are:

      3.2.1. To make copies of the Article (all or part) for teaching purposes;

      3.2.2. To include the Article (all or part) in a research thesis or dissertation;

      3.2.3. To make oral presentation of the Article (all or part) and to include a summary and/or highlights of it in papers distributed at such presentations or in conference proceedings; and

      3.2.4. All proprietary rights other than copyright.

   3.3. The additional rights are to:

      3.3.1. Use the Article (all or part) without modification in personal compilations or publications of a Named Author's own works (provided not created by third party publisher);

      3.3.2. Include the Article (all or part) on a Named Author's own personal web site;

      3.3.3. Include the Article (all or part) on web sites of the Institution (including its repository) where a Named Author worked when research for the Article was carried out; and

      3.3.4. Include the Article (all or part) on third party web sites including e-print servers, but not on other publisher's web sites.

Vita

Oleg Korobkin was born in Dnepropetrovsk, Ukraine (former socialist republic of the USSR), in December 1977, as the son of Gennady Korobkin and Taisa Korobkina. He has completed his undergraduate program in Moscow Institute of Physics and Technology at 1998 and graduated with Master of Sciences degree in applied physics and maths in 2003. When working on his master's thesis, Oleg Korobkin was associated with Ginzburg theoretical physics group at Lebedev Physical Institute, Moscow. He was supervised by Dr. Andrei Silin and the subject of his research was spectra of semiconducting quantum wires. In January 2005, Oleg Korobkin started his graduate studies towards a doctoral degree at the Department of Physics and Astronomy in Louisiana State University. First three years he worked with Dr. Manuel Tiglio. Starting from 2008 Oleg Korobkin was doing his doctoral research under the supervision of Dr. Erik Schnetter. His publications include:

- Oleg Korobkin, Ernazar Abdikamalov, Erik Schnetter, Nikolaos Stergioulas, Bukhard Zink, *"Stability of General Relativistic Accretion Disks"*, in preparation for submission.

- Eloisa Bentivegna, Gabrielle Allen, Oleg Korobkin, Erik Schnetter, *"Ensuring correctness at the application level: a software framework approach"*, Proceedings of the Workshop on Component-Based High Performance Computing, in Portland, Oregon, 2009.

- Bukhard Zink, Oleg Korobkin, Erik Schnetter, Nikolaos Stergioulas, *"On the frequency band of the f-mode CFS instability"*, Phys.Rev.D, **81**(8), pp.84-55, 2010.

- Andrei Hutanu, Erik Schnetter, Werner Benger, Eloisa Bentivegna, Alex Clary, Peter Diener, Jinghua Ge, Robert Kooima, Oleg Korobkin, Kexi Liu, Frank Löffler, Ravi Paruchuri, Jian Tao, Cornelius Toole, Adam Yates, and Gabrielle Allen, *"Large-scale problem solving using*

automatic code generation and distributed visualization", in "Scalable Computing: Practice and Experience", Vol.**11**, no. 2, June 2010.

- Oleg Korobkin, Burak Aksoylu, Michael Holst, Enrique Pazos, Manuel Tiglio, *"Solving the Einstein constraint equations on multi-block triangulations using finite element methods"*, Class.Quant.Gravity, 26, pp.145-152, 2009

- Oleg Korobkin, *"Energy Spectrum of semiconductor quantum wires"*, Master's thesis, Moscow Institute of Physics and Technology, 2003

- Oleg Korobkin, Andrei P. Silin, *"Influence of the geometric shape of the quantum wires and quantum dots on their energy spectrum"*, Bulletin of the Lebedev Physics Institute, 07, 2003

- Oleg Korobkin, Andrei P. Silin, *"Energy spectrum of narrow-gap semiconducting quantum wires"*, Bulletin of the Lebedev Physics Institute, 10, 2002